28 Apr 2006

AFCI Quarterly Report

Transmutation Engineering

Jan – Mar 2006

LA-UR-06-3096

The inaugural meeting of the Gen IV Materials Handbook Committee was held in Santa Fe, New Mexico at the Bishop's Lodge (February 28-March 1, 2006) including representatives from the Gen IV and AFCI programs.

Blank Page

AFCI Technical Quarterly Report
Transmutation Engineering
Jan – Mar 2006
LA-UR-06-3096

Approvals

Date 4/27/06

Michael Cappiello, AFCI National Technical Director
for Transmutation Engineering

Blank Page

Table of Contents

Major Contributors ..... **vii**

Acronyms and Symbols ..... **ix**

TRANSMUTATION ENGINEERING **1**

Introduction 1

Physics **2**

Scope 2

Highlights 2

Nuclear Data Evaluations 3

Scope 3

Analysis of Experimental Data 4

Nuclear Reaction Calculations 6

Code Development 9

Detailed Assessment of Experimental Uncertainties 9

Nuclear Data Sensitivity Analysis 10

Scope 10

Technical Summary 10

Cross Section Measurements 15

Fission Cross-Section Measurement 15

Capture Cross-Section Measurement 16

Gas Production Cross-Section Measurements 18

Target Preparation 21

Code Development 23

MCNPX 23

Structural Materials **28**

Scope 28

Highlights 29

Materials Testing 30

LANL Hot-Cell Work 30

PNNL Activities 33

Radiation Damage Modeling of Structural Materials 36

Simulation of Radiation Cascades in Fe-Cr System 36

KMC Simulations of Helium in Iron and Ferritic Steels 39

Coolant Technology **45**

Scope 45

Highlights 45

Integration 45

DELTA Loop Operations 46

Oxide Layer Analysis 46

Lead Correlation Stand (LCS) 49

Corrosion Control 49

Irradiation Effects on Corrosion 51

Corrosion Resistant Alloys 52

Transmuter Design Activities 52
Transmuter Design 52
Scope 52
Highlights 52
Technical Summary 52
Experimental Physics [ANL] 54
Scope 54
Highlights 54
Technical Summary 55

Materials Test Station (MTS) 61
Integration 62
External Review Committee Report 62
Neutronics Design 63
Target Calculations 64
Shielding and Activation 65
Target Assembly 66
Overview 66
Design Trade Studies 67
Decay Heat Removal 69
Prototype Target Plate Cladding 70
Target Plate Cooling Experiments 71
Auxiliary Systems 72
Target Resource Auxiliary Module (TRAM) 72
Helium Chamber and Internals 79
Inner Shielding and Helium Tank 79
Accelerator Systems 81
Safety and Permitting 81

LANL-Sponsored University Programs 82
University of Illinois 82
Scope 82
Impedance Spectroscopy for Monitoring Corrosion in LBE Systems 82
Effects of Helium on Irradiation Damage in BCC Iron 87

References 90

Major Contributors

C. Ammerman (LANL)
J. Baker (LANL)
B. Blind (LANL)
M. Cappiello (LANL)
P. Demkowicz (INL)
J. Eddleman (LANL)
F. Garner (PNL)
B. Haight (LANL)
J. Hendricks (LANL)
T. Hill (LANL)
G. Imel (ANL)
M. James (LANL)
K. Johnson (LANL)
T. Kawano (LANL)
R. Kellogg (ANL)
N. Li (LANL)
S. Lillard (LANL)
C. McGrath (INL)
S. Maloy (LANL)
A. Marchese (LANL)
G. Palmiotti (ANL)
E. Pitcher (LANL)
R. Reifarth (LANL)
D. Rusthoi (LANL)
R. Sheffield (LANL)
S. Srivilliputher (LANL)
P. Talou (LANL)
M. Toloczko (PNNL)
F. Tovesson (LANL)
J. Ullmann LANL)
S. Wender (LANL)
K. Woloshun (LANL)

Blank Page

Acronyms and Symbols

ADS	Accelerator-Driven System
ADMAB	Accelerator-Driven Minor Actinide Burner
AFCI	Advanced (Nuclear) Fuel Cycle Initiative
AFM	Atomic Force Microscopy
A•h	Ampere-Hour
AHA	Acetohydroxamic acid
Am	Americium
AMUSE	Argonne Model for Universal Solvent Extraction, the generic TRUEX model expanded to include UREX and PUREX processing
ANL	Argonne National Laboratory (Chicago)
ANS	American Nuclear Society
ANSYS	structural analysis modeling code
appm	atomic parts per million
ASME	American Society of Mechanical Engineers
ATR	Advanced Test Reactor (INEEL)
ATW	Accelerator Transmutation of Waste
Ba	Barium
BCM	Beam-Current Monitor
BCP	Baseline Change Proposal
BCP	Buffered Chemical Polishing
Be	Beryllium
Beta (β)	Ratio to the speed of light
Bi	Bismuth
BISTRO	Two-Dimensional Discrete Ordinates Code
BNFL	British Nuclear Fuels, Ltd
BNL	Brookhaven National Laboratory
BOR-60	Sodium-Cooled Fast Reactor (Dmitrovgrad, Russia)
BSE	backscattered electron (images)
Ce	Cerium
C/E	calculated/experimental values
CEA	Commissariat à l'Energie Atomique (France)
CEM	Cascade Exciton Model code (Model-based Monte-Carlo particle transport code)
CERCA	Compagnie Pour L'Etude Et La Realisation De Combustibles Atomiques
cercer	Ceramic-Ceramic
cermet	Ceramic-Metal
CFD	Computational Fluid Dynamics
CINDER90	Computer Code
CLWR	Commercial Light-Water Reactor
Cm	Curium
CMR	Chemistry and Metallurgy Research (facility at LANL)
CONCERT	COmbined Neutron Center for European Research and Technology
CS	cross section
Cs	Cesium
Cu	Copper
CVD	Chemical Vapor Deposition
DACS	Data Acquisition and Control System
DANCE	Detector for Advanced Neutron Capture Experiment
DAS	Data Acquisition System
DBTT	Ductile-To-Brittle Transition Temperature
DELTA	DEvelopment of Lead-alloy Technology Applications
DFT	Density Functional Theory
DIAMEX	Aqueous Solvent Extraction Process for TRU Recovery

DOE	Department of Energy
dpa	Displacements per Atom
EBR	Experimental Breeder Reactor
EDS	Energy Dispersive Spectrometry
EFPD	Effective Full-Power Day
EFTTRA-T4	Radiation Test Sponsored by the European Union
EIS	Electrochemical Impedance Spectroscopy
EIS	Environmental Impact Statement
ENDF	Evaluated Nuclear Data File - Evaluations that can be used in MCNPX for more accurate predictions of fission, criticality, transport, and radiation damage
EOI	End of Irradiation
EOL	End of Life
ECAP	Equal Channel Angular Process
ERANOS	Computer modeling code
ES&H	Environmental, Safety, and Health
ESS	European Spallation Source
ESSAB	Energy System Acquisition Advisory Board (DOE)
Eu	Europium
Fe	Iron
FFTF	Fast Flux Test Facility (Richland, WA)
FPY	Full-Power Year
FWHM	Full Width Half Maximum
FZJ	Forschungs Zentrum Jülich (German Laboratory)
FZK	Forschungs Zentrum Karlsruhe (German Laboratory)
g/L	Grams per Liter
GNASH	Nuclear Reaction Code
GSI	Gesellschaft für Schwerionenforschung (Darmstadt, Germany)
GT-MHR	Gas Turbine Modular Helium Reactor
H	Hydrogen
HAN	Hydroxylamine
HCP	Hazard Control Plan
He	Helium
HEBT	High-Energy Beam Transport
HEU	Highly enriched uranium
Hf	Hafnium
HFIR	High Flux Isotope Reactor (ORNL)
HFR	High Flux Reactor (Petten, Netherlands)
Hg	Mercury
HIP	Hot Isostatic Process (for bonding materials)
HM	Heavy metal
HPRF	High-Power Radio Frequency
HX	Heat exchanger
I&C	Instrumentation and Control
IAC	Idaho Accelerator Center
IAEA	International Atomic Energy Agency (Vienna, Austria)
IBML	Ion Beam Material Lab (in Los Alamos)
ICP-MS	Inductively Coupled Plasma-Mass Spectrometry
ICS	Integrated Control System
IFMIF	International Fusion Materials Irradiation Facility
IFR	Integral Fast Reactor
IHX	Intermediate Heat Exchanger
IMS	Information Management System
INEEL	Idaho National Engineering and Environmental Laboratory
INL	Idaho National Laboratory
IPBT	In-Pile Beam Tube

IPPE	Institute of Physics and Power Engineering (Obninsk, Russia)
ISABEL	Physics Modeling Code
ISTC	International Science and Technology Centre (Moscow)
ITER	International Thermonuclear Experimental Reactor
ITU	Institute for Transuranium Elements (Karlsruhe, Germany)
JAERI	Japan Atomic Energy Research Institute
JFMS	Japanese Ferritic/Martensitic Steel
JLAB	Jefferson Laboratory (VA)
K	Potassium
KAERI	Korean Atomic Energy Research Institute
KEK	National Laboratory for High-Energy Physics (Tsukuba, Japan)
keV	Kiloelectron Volt
KMC	Kinetic Monte Carlo
KRI	Khlopin Radium Institute (Russia)
LA150n	Los Alamos generated nuclear data library, extending up to 150 MeV
LAHET	Los Alamos High-Energy Transport
LANL	Los Alamos National Laboratory
LANSCE	Los Alamos Neutron Science Center
LBE	Lead-bismuth eutectic
L/d	Length-to-diameter ratio
L/hr	Liter per hour
LCFR	low-conversion-ratio fast reactor
LEBT	Low-Energy Beam Transport
LEDA	Low-Energy Demonstration Accelerator
LHGR	linear heat generation rate
LLFP	Long-lived fission product
LLNL	Lawrence Livermore National Laboratory
LLRF	Low-level radio frequency
LME	Liquid-metal embrittlement
LMFBR	Liquid-Metal Fast Breeder Reactor
LMR	Liquid Metal Reactor
LWR	Light Water Reactor
M	Molar
MA	Minor actinide
mb	Millibarn
mCi	Millicurie
MCNP	Monte Carlo N-Particle Transport Code
MCNPX	Merged code—Los Alamos High-Energy Transport (LAHET) and Monte Carlo N-Particle Codes (MCNP)
MCWO	MCNP Coupling With ORIGEN2 (burnup calculation code)
MD	Molecular dynamics
MDD	Modified Direct Denitration
MEAM	Molecular Embedded Atom Method
MEGAPIE	Megawatt Pilot Experiment
MFM	Magnetic Flow Meter
MIT	Massachusetts Institute of Technology
mL	Milliliter
Mo	Molybdenum
MOTA	Materials Open Testing Assembly
MOX	Mixed-oxide fuel
MPM	multistage pre-equilibrium model
mR	Millirad (a measure of radiation)
MSM	Modified Source Multiplication (MSM) method
MSA	Multiplication Approximated Source or Multiplication Source Approach
MTS	Materials Test Station

MUSE	CEA-Cadarache Zero-Power Subcritical Experiments
MW	Megawatt
MWD/T	Megawatt Days per Ton (standard unit for burnup)
MWth	Megawatt thermal
N	Nickel or nitride
Np	Neptunium
n/p	Neutrons per proton
NDA	Nondestructive analyses
NEA	Nuclear Energy Agency (Paris)
NEPA	National Environmental Protection Agency
NERAC	Nuclear Energy Research Advisory Committee
NERI	Nuclear Energy Research Initiative
NFC	Nuclear Fuel Cycle
NFF	Nonfertile Fuel
NUTS	NUclide Time-dependent Sensitivity
O	Oxygen or Oxide
O&M	Operations and Maintenance
OECD	Organization for Economic Cooperation and Development (Paris)
ORIGEN	A computer code system for calculating the buildup, decay, and processing of radioactive materials
ORNL	Oak Ridge National Laboratory
P&ID	Piping and Instrumentation Diagram
P&T	Partitioning and Transmutation
PACS	Personnel Access Control System
Pb	Lead
PCM	Pulse Control Modulation
Pd	Paladium
PD	prompt decay
PFD	Process Flow Diagram
PHA	Preliminary Hazards Assessment
PHENIX	Fast Reactor in France
PIE	Post-Irradiation Examination
PKA	Primary Knock-on Atom
PNNL	Pacific Northwest National Laboratory
PNS	Pulsed Neutron Sources
POP	Proof of Performance, Proof of Principle
PRAD	Proton Radiography
PRISM	Power Reactor Innovative Small Module
PSAR	Preliminary Safety Analysis Report
PSS	Personnel Safety System
PSI	Paul Scherrer Institute (Switzerland)
Pu	Plutonium
PUREX	Plutonium-Uranium Extraction
PWR	Pressurized Water Reactor
PYRO	Pyrochemical process
Q	Quality factor
QA	Quality Assurance
R	Rad (a unit of radiation)
RACE	Reactor-Accelerator Coupling Experiments
RAMI	Reliability, Availability, Maintainability, and Inspectability
RBS	Rutherford Backscattering Spectrometry
RERTR	Reduced Enrichment for Research and Test Reactors program
RF	Radio Frequency
RFQ	Radio-Frequency Quadrupole
RIA	Rare Isotope Accelerator

RIAR	Russian Institute of Atomic Reactors
rms	root mean square
RRR	Residual Resistance Ratio
RSICC	Radiation Safety Information Computational Center
RTD	Surface Temperature Detector
RTH	Royal Institute of Technology (Stockholm, Sweden)
SANEX	Aqueous Solvent Extraction Process for Am and Cm Recovery
SAR	Safety Analysis Report
SC	Superconducting
SCM	Subcritical Multiplier
SCRF	Superconducting RF
SDD	System Design Description
SEM	Scanning Electron Microscopy
SFT	Stacking-Fault Tetrahedral
SHR	shutdown heat-removal
SINQ	Spallation Neutron Source at Paul Scherrer Institute (Switzerland)
SM	source multiplication
SNF	Spent Nuclear Fuel
SNL	Sandia National Laboratory
SRS	Savannah River Site
SRTC	Savannah River Technology Center
Star-CD	Computational fluid dynamics code
STAYSL	A computer code to analyze results of activation foil measurements
STAYSL2	A computer code to analyze results of activation foil measurements in both a proton and neutron flux
STP	Standard Temperature and Pressure
STIP	Spallation Target Irradiation Program (at PSI)
T/p	Tritons (nucleii of tritium atoms) per Proton
Ta	Tantalum
TAD	Temperature Accelerated Dynamics
TBP	Tri-*n*-butyl Phosphate or Tributylphosphate
Tc	Technitium
TEM	Transmission Electron Microscopy
TESLA	International Collaboration on a TeV Superconducting Linear Accelerator
TGA	Thermal Gravimetric Analysis
TJNAF	Thomas Jefferson National Accelerator Facility
TMT	Target and Materials Test Station
TRAC	Transient Reactor Analysis Code
TRACE 3-D	Interactive computer code that calculates the envelopes of a bunched beam through a user-defined transport system
TREACS	TReat Experiment for ACcelerator-driven Systems
TREAT	Transient Reactor Test Facility
TRISO	Tri-isotropic, referring to a multi-layered fuel-particle coating consisting of pyrolytic carbon and silicon carbide
TRADE	TRIGA Accelerator Driven Experiment
TRAM	Target Resource Auxiliary Module
TRIGA	Small Reactor Type
TRL	Technical Readiness Level
TRU	Transuranics (americium, curium, neptunium, and plutonium)
TRUEX	Aqueous solvent extraction process for TRU recovery
U	Uranium
UNLV	University of Nevada Las Vegas
UREX	Uranium Extraction (an aqueous partitioning process)
URA	University Research Alliance
URP	University Research Program

USQD	Unreviewed Safety Question Determination
V	Vanadium
VPS	Vapor Plasma Spray
VARIANT	Three-Dimensional Nodal Transport Code
W	Tungsten
WBS	Work Breakdown Structure
WNR	Weapons Neutron Research (facility at LANL)
WPPT	Working Party on Partitioning and Transmutation
WSRC	Westinghouse Savannah River Company
Xe	Xenon
XPS	X-ray Photo Spectroscopy
XRD	X-ray Diffraction
Y	Yttrium
ZPPR	Zero Power Physics Reactor
Zr	Zirconium

Advanced Fuel Cycle Initiative
Transmutation Engineering
Quarterly Report
January - March 2006

TRANSMUTATION ENGINEERING

Introduction

The top-level objective for Transmutation Engineering is to develop the engineering basis for the transmutation of minor actinides (MA) and long-lived fission products (LLFP) so informed decisions can be made in the next few years concerning transmutation technologies, and a path forward can be developed for implementation. In support of that objective, proof-of-principle information is being developed in areas not supported in the fuels, separations, Gen IV research or other DOE-NE research programs. In the near-term, transmutation engineering activities are focused in the areas of physics, nuclear data and codes, coolants and corrosion, structural materials, and accelerator-based transmutation.

Subsequent to a decision on transmutation technology and a successful proof-of-principle phase, engineering development and demonstration will be performed to provide proof-of-performance to prepare for deployment of a transmuter technology.

In the next five years, information provided by transmutation engineering and other advanced fuel-cycle activities will provide support for key decisions. This support can be summarized as follows:

- Transmutation Engineering Physics will provide nuclear cross-section data in the thermal, epithermal, and fast-neutron spectra. These data will allow the accurate prediction of transmutation rates and reduce calculation uncertainties. Coefficients of reactivity will be obtained in all three spectra to support licensing and safety analyses. Analysis codes will be developed, validated, and benchmarked so design calculations can be made with confidence. The Performance Measure for this activity is to "Reduce and Quantify Uncertainty of ^{237}Np Nuclear Data."
- Transmutation Engineering Materials activities will provide detailed information on the degradation of structural materials in a fast-neutron spectrum and mixed-particle environment (neutrons and protons). Material limits will be established that help determine the level of burnup that can be obtained, and therefore, the effectiveness of the various options. Heavy-metal coolant technology for critical reactor and accelerator-driven systems will be developed that supports the selection of technology options. The FY06 Performance Measure for this activity is

to “Select Alloys for Transmuter Technology”. As part of this effort, a major new capability for irradiations of materials and fuels for the AFCI and Gen IV programs will be implemented. The Materials Test Station at LANSCE will provide fast neutrons for experimenters to develop the necessary transmutation materials, and complement the irradiations being performed in the ATR, France and Japan.

- Transmutation Engineering Activities in Accelerator-Driven Systems will provide necessary information on the physics of coupling an accelerator to a subcritical system and the operation and start-up of such systems. In addition, the target technology necessary to drive these systems will be developed to support the technology decisions. This activity area will rely heavily on the ADS activities being performed at UNLV, ISU, and within the EUROTRANS Program.

Physics

Scope

Transmutation engineering physics will provide nuclear cross-section data in the thermal, epithermal, and fast-neutron spectra. These data will allow the accurate prediction of transmutation rates and reduce calculation uncertainties. Coefficients of reactivity will be obtained in all three spectra to support licensing and safety analyses. Analysis codes will be developed, validated, and benchmarked to enable design calculations to be made with confidence. The major objective of high-energy physics activities is to improve and maintain the computer codes used in the analyses of transmutation systems. As part of the improvement, the nuclear data accuracy is reevaluated to match desired objectives.

Implementation of the Physics Scope of Work includes analyzing the results of irradiations performed in the French fast reactor (PHENIX) of PROFIL-2 (irradiation of actinides) and TRAPU (irradiation of mixed oxides) to gather information on the transmutation rates and associated cross sections of such isotopes. Time-dependant calculations are carried out to perform the analyses and to evaluate the discrepancy between experimental and computational results.

Codes and associated libraries for thermal and fast reactor, as well as whole-core codes, need to be upgraded for new types of fuels and reflectors for different types of advanced fuel-cycle strategies involving mixed-oxide fuels (MOX), gas-cooled reactors, and liquid-metal-cooled systems, with presence of minor actinides or fertile-free compositions. Our scope includes the following tasks: maintain, update, and improve fuel-cycle codes, support users, and perform limited code development.

Highlights

Nuclear Data Evaluations

- Additional experimental data sets for neutron-induced reactions on ^{235}U have been included in the analysis of uncertainties, specifically, capture-to-fission ratio data and prompt number of neutrons per fission.

- New nuclear-reaction model calculations have been carried out, with more input parameters included in the sensitivity matrix prediction.

Nuclear Data Sensitivity Analysis

- In the frame of representativity analysis, a study was performed to compare the integral experiment ZPPR-2 and the large (European) sodium-cooled fast reactor (EFR). Good representativity factors were observed for the integral parameters K_{eff}, β_{eff} and η, as well as for the spectral indices at the interface blanket/reflector. However, a low value of representativity was found for the spectral index at the core center.
- A representativity study was completed of Assembly 53 of Integral Experiment ZPR-3 with respect to all fast systems investigated during the extensive sensitivity analysis performed the last fiscal year (GFR, EFR, SFR and LFR). Beside the EFR, a fairly good representativity was observed between Assembly 53 and the GFR reactor. As expected, a poor similarity was found for the LFR reactor.

Cross Section Measurements

- The LANSCE accelerator is still in its maintenance period. Beam is expected to resume on or about May 1, 2006. Proposed measurements are a completion of the gas production experiments on zirconium and a new gas production measurement on molybdenum, high energy fission measurements for ^{242}Pu and ^{240}Pu, and supplementary capture data for ^{239}Pu, ^{240}Pu and ^{242}Pu.
- The ^{237}Np fission data was used in a new evaluation that has been submitted to ENDF/B-VII.
- A new cooperative effort is underway between LANL evaluators and LANL experimentalists to improve the reporting of uncertainties and their covariance in fission cross-section data.
- Energy calibration for the available ^{242}Pu data is complete and the analysis continues on schedule.

MCNPX

- Two methods for burnup-depletion predictor-correction acceleration were completed and reviewed. The MONTEBURNS method was chosen for integration into MCNPX 26B. This new method speeds up calculations of a pin-cell problem by a factor of three with no loss in accuracy.

Nuclear Data Evaluations

Scope

In FY06, we are focused on providing an uncertainty quantification of reactions of interest for the AFCI program. The need for reliable uncertainties has been stressed by the work of Palmiotti, *et al.,* on sensitivity studies which can help better focus the experimental and evaluation efforts in the coming years for some key ADS and Gen-

IV reactors. The overall goal of our present work is to evaluate covariance matrices of reactions of interest to AFCI/Gen-IV in a form suitable for use in sensitivity calculations. The neutron-induced reactions to be studied this year concern three major isotopes: ^{235}U, ^{238}U and ^{239}Pu; the first one being studied is ^{235}U.

Analysis of Experimental Data

In the last Quarterly report, we briefly presented the motivations and the procedure for estimating the global covariance matrix that quantifies the quality of the evaluations for neutron-induced reactions on ^{235}U, ^{238}U, and ^{239}Pu. In the present report, we focus on results obtained for ^{235}U.

The most difficult and time-consuming part of the covariance evaluation effort lies in the correct estimation of uncertainties in experimental data sets. Here, we review some of the steps followed in the analysis of different reaction channels. Some reaction cross sections were already described in the previous report. Therefore, we focus here only on experimental data for the quantities α and $<\nu>$.

Data on α = σ(Capture) / σ(Fission)

Direct measurements of the capture cross sections of fissile nuclei are difficult and subject to large errors. This is in large part due to the difficult experimental separation of capture from fission events. Some other corrections (neutron flux, overall normalization, etc.) make it very cumbersome to measure the capture cross section itself. Instead, most often this quantity is obtained through the measurement of the ratio $\alpha=\sigma(capture)/\sigma(fission)$. Obviously, this is also a fundamental quantity in reactor physics.

Known measurements of α for ^{235}U started in the fifties. Measurements continued through the seventies by various experimental groups using different techniques. Because the sources of errors in the different experiments are for the most part uncorrelated, the combination of experimental data will lead to a significant decrease in the evaluated uncertainties using the principle of Bayesian inference. Of course, this is an ideal theoretical view, because most of the techniques used to estimate α are not totally independent. Nevertheless, it is true that the techniques to determine α are quite different from one experiment to another.

As mentioned, the main experimental problem lies in the differentiation between capture and fission events. Some groups have used the detection of fission fragments in coincidence with the observed pulse, the detection of the prompt neutrons (assuming a particular form for the P(ν) distribution and width), or the renormalization to the high-energy part of the observed γ-ray spectrum. These various techniques, although different from each other, have rather large uncertainties due to the complicated corrections to be made to the raw data. On average, systematic uncertainties are of the order of 7-10%.

Figure 1 shows a selected subset of experimental data and the result of a generalized-least-squares (GLS) treatment. The evaluated covariance matrix is shown in Fig. 2.

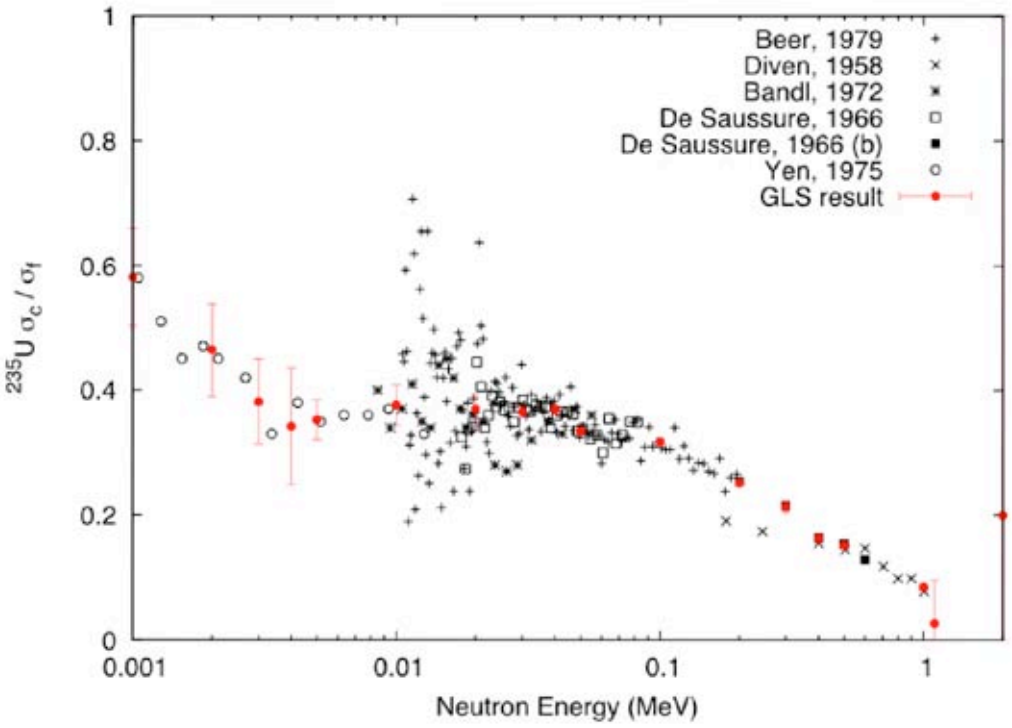

Fig. 1. Experimental data on $\alpha = \sigma_c/\sigma_f$ for ^{235}U, and the result of a Generalized-Least-Squares (GLS) evaluation (in red).

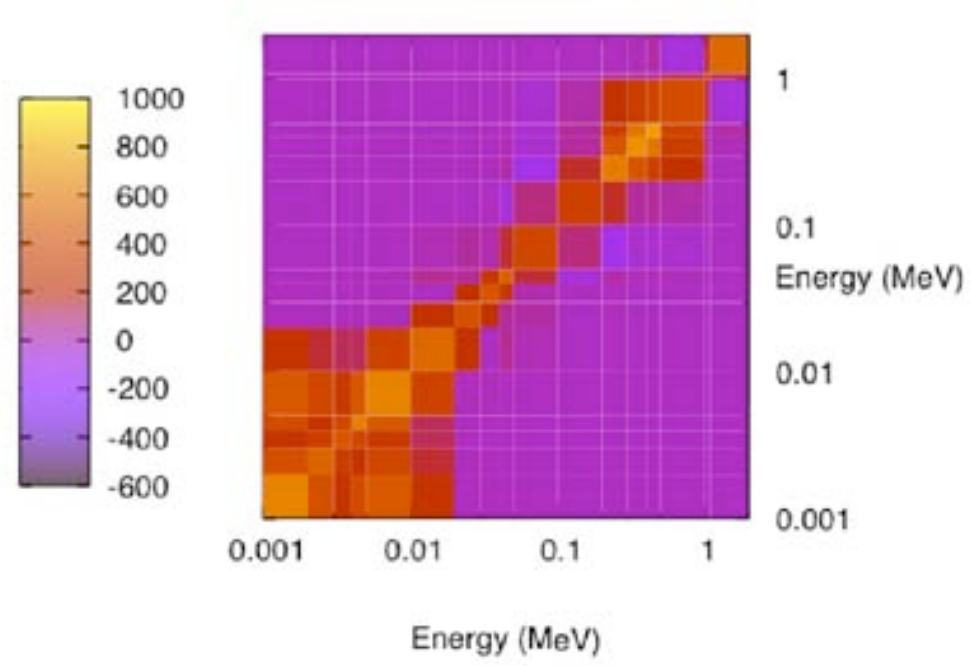

Fig. 1. Correlation matrix for $\alpha(^{235}U)$ experimental data sets.

Data on <ν>, Number of Prompt Neutrons per Fission for ^{235}U

The number of prompt neutrons per fission, <ν>, is a very important quantity since it directly impacts the neutron economy in a reactor. It also gives some important insights in the later stage of the fission process. The variation of <ν> as a function of incident neutron energy has been studied by various groups over the years, and is plotted on Fig. 3.

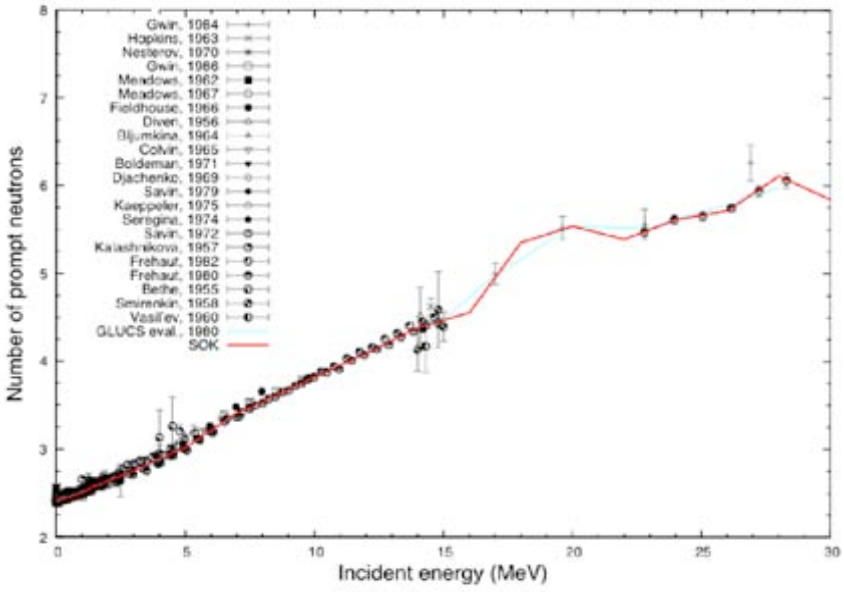

Fig. 2. Average number of prompt neutrons <ν> in the neutron-induced fission of ^{235}U, as a function of neutron incident energy.

In most experiments, the average number of prompt neutrons emitted in the spontaneous fission of ^{252}Cf is used to infer the corresponding value for ^{235}U. Therefore, almost all measurements were done in ratio to $<\nu>(^{252}Cf_{(sf)})$, and had to be re-normalized for the present GLS evaluation. This was done using the new ENDF/B-VII standard values for $<\nu>(^{252}Cf_{(sf)})$ as a function of neutron incident energy.

Because this quantity is not calculated in standard nuclear-reaction calculations but instead obtained with a separate code (which implements the fission model of Madland-Nix), we will only use the experimental covariance matrix for the final evaluated covariance matrix.

Note that the erratic behavior of the GLS (SOK) result for <ν> observed between 15-20 MeV is simply due to some limitations in the interpolation scheme in our code, and will be smoothed out in the final result.

Nuclear Reaction Calculations

A second step in the covariance evaluation procedure used in the present work requires estimated uncertainties and correlations due to model calculations.

We assume that the physical models implemented in GNASH are valid and can be applied successfully to describe the quantities of interest, provided that appropriate model input parameters are chosen.

Once the "initial" set of model input parameters is chosen and GNASH calculations ran accordingly, the input parameters are varied in order to obtain the following sensitivity coefficients:

$$S_{ij} = (\delta\sigma_i) / (\delta p_j).$$

These coefficients quantify how much a particular calculated cross section changes if the value of a single parameter is changed. A similar quantity is the relative sensitivity R_{ij}, defined as

$$R_{ij} = (\delta\sigma_i/\sigma_i) / (\delta p_j/p_j) = S_{ij} \times p_j/\sigma_i.$$

A driver script was developed to generate GNASH input files directly from a set of default parameters, except for one parameter whose value is changed to determine the impact on the computational result. The script was then adapted to launch multiple GNASH runs in parallel on the new LANL T-16 cluster machine. The new script accommodates numerous GNASH calculations at a fraction of the time required on a single-CPU machine, and for a larger number of incident neutron energies.

Some results are shown in the following figures (Figs. 4-6). A subset of model parameters was chosen, according to its *a priori* relevance to the calculation of particular channel cross sections.

Relative sensitivities of the calculated neutron-induced fission cross-section of ^{235}U to the choice of the inner and outer barrier heights in GNASH fission model are shown in Fig.4. As expected, we can distinguish three regions according to the neutron incident energy E_n. If E_n is lower than the neutron binding energy B_n, the fission channel is dominated by the first chance fission *(n,f)* and only the barrier heights for the compound nucleus ^{236}U are important. This plot also indicates that if one changes the fission barrier height (inner or outer) by about 1%, changes in the calculated fission cross section are about 4%. This is roughly true until the second chance fission *(n,n'f)* becomes dominant above about 6 MeV. Then, the fission barrier heights in ^{235}U become the most important factors.

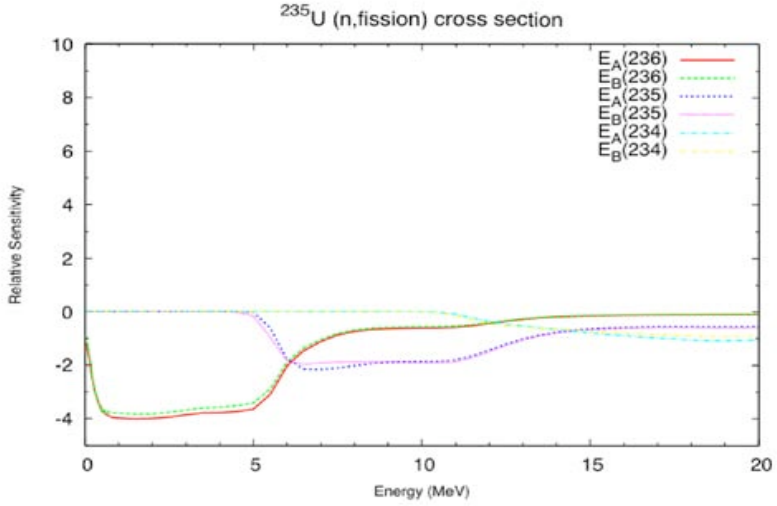

Fig. 4. Relative sensitivities of the calculated neutron-induced fission cross-section of ^{235}U to the inner and outer fission barrier heights in the $^{234-236}$U compound nuclei.

As expected, Fig. 4 also indicates that increasing the barrier heights tends to reduce the fission cross section (negative sensitivities).

Another *a priori* important parameter in fission calculations is the width $(h\omega)_{A,B}$ of the fission barriers. However, sensitivity calculations show that these values have little influence on the GNASH calculations. The same holds true for the factors that are used to describe the enhancement of collective states due to asymmetries at the saddle points. However, the range of values for those parameters can also be very large, and uncertainties may still be important.

In the present GNASH calculations, the Gilbert-Cameron-Ignatyuk formalism was used to represent level densities in the continuum. The 'a' level density parameter and the pairing energy 'Δ' are the only parameters in this model. We have also studied the impact of these parameters on GNASH results. The result is shown in Fig. 5 for the *(n,fission)* cross section.

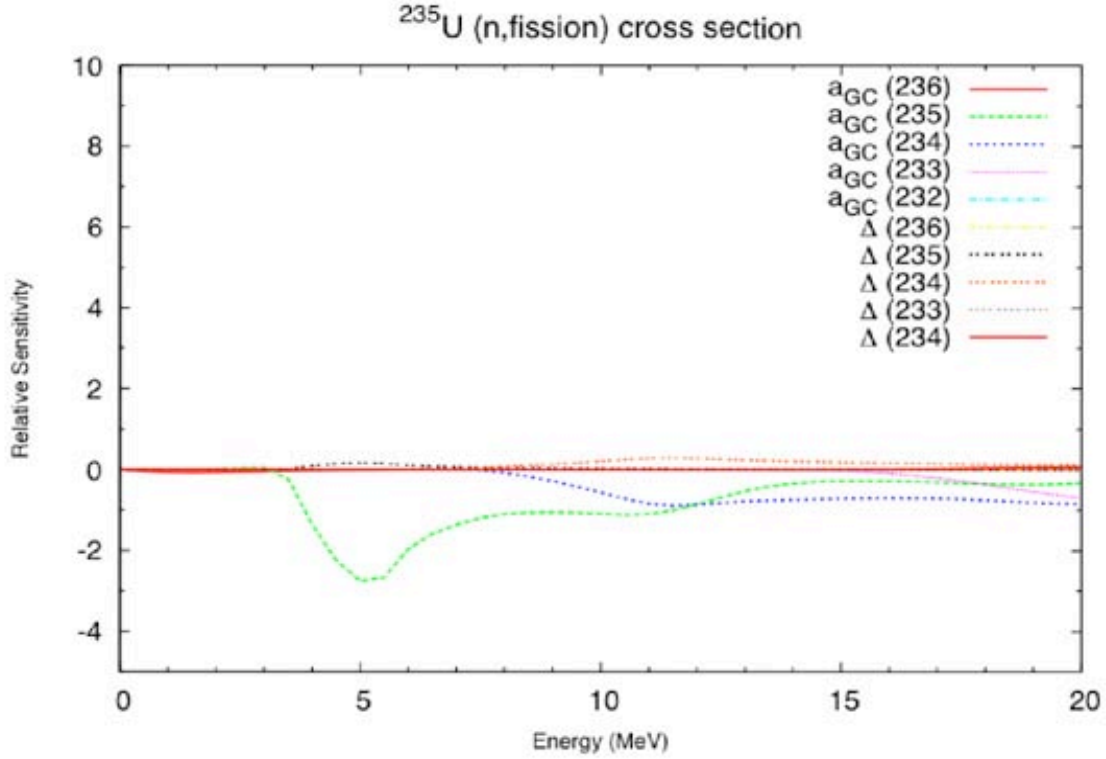

Fig. 5. Relative sensitivities for the calculated *(n,fission)* cross-section to the choice of level density parameters 'a' and 'Δ'.

Figure 5 shows that the pairing energy values have very little impact on the calculated fission cross section. However, the level density parameters 'a' in ^{235}U and to a lesser extent in ^{234}U are important. Those parameters define the number of final states available for the decay of the nucleus by *(n,n')* and *(n,2n)* reactions, which are in competition with the fission channel. Obviously, by correlation, they also influence strongly the *(n,n')* and *(n,2n)* channels as can be seen in Fig. 6.

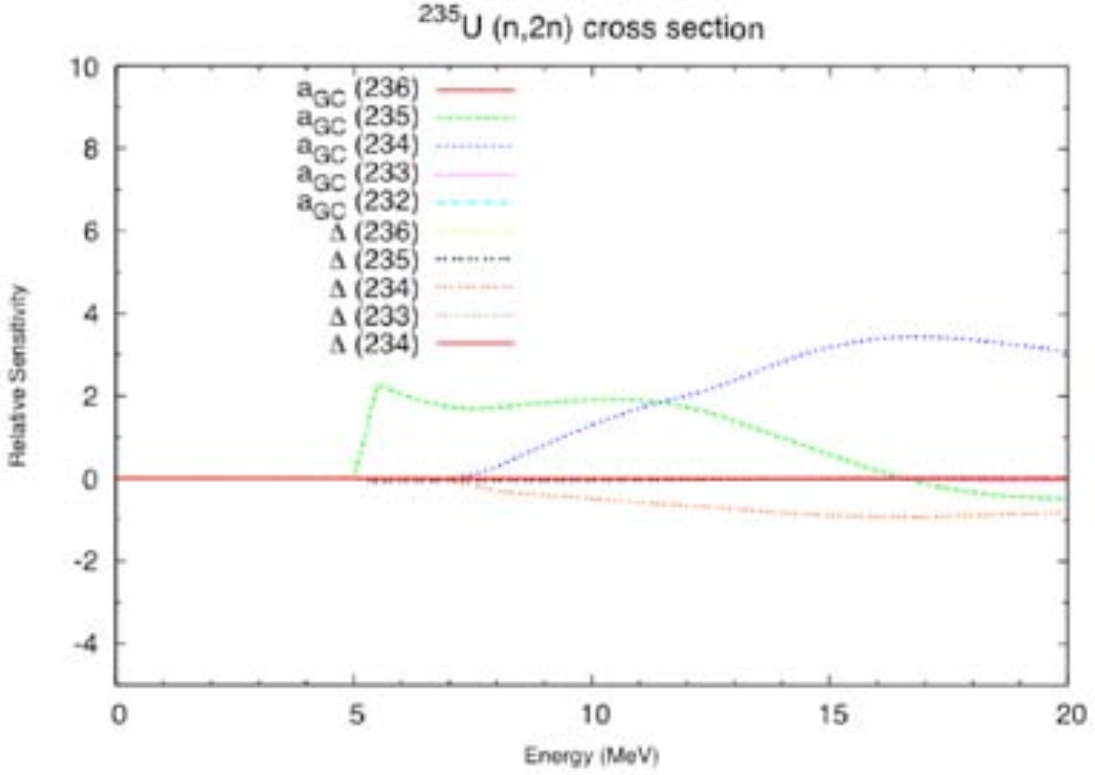

Fig. 6. Relative sensitivities for the calculated *(n,2n)* cross-section to the choice of level density parameters 'a' and 'Δ'.

Because of energy considerations, the impact on the *(n,2n)* cross section is null below the neutron binding energy. This time, the sensitivity coefficients are positive: increasing the level density in the ^{235}U "final" nucleus tends to increase the probability for the *(n,2n)* channel in competition with the *(n,n')* and *(n,fission)* channels.

The figures above are only a subset of the model sensitivities calculated with the GNASH reaction code, since all important reaction cross sections studied in this work were calculated in this manner.

Code Development

A code was written to generate an ENDF-formatted covariance matrix from the result of the KALMAN code. This is a very important step for the release of evaluated covariance matrices in an appropriate format for further processing.

Detailed Assessment of Experimental Uncertainties

In collaboration with F. Tovesson (LANSCE) and T. Hill (LANSCE), we have started an important effort to analyze the various sources of uncertainties in the measurement of the ^{237}Np *(n,fission)* cross-section recently performed at the Lujan Center and WNR facilities.

Thanks to this close collaboration between experimentalists and evaluators, important steps toward a better understanding of experimental uncertainties have been made in

this particular measurement, and therefore are in a much better position to produce realistic covariance data.

Nuclear Data Sensitivity Analysis

Scope

Past uncertainty evaluations have shown that poor quality cross section can have severe impact on margins to be taken on neutronic design parameters (e. g. critical mass, reactivity coefficients, power distribution etc,) of system of interest of the AFCI program. This is the first year of a three-year program that will assess the quality of recently available cross-section data files: ENDF/B-VII, JEF3.1 (and possibly JENDL3.3). This will be done by selecting among the several hundred integral experiments performed in the USA and abroad those that are relevant and representative of the AFCI transmuter systems using covariance data and sensitivity techniques and then analyzing the performance of the data files on the selected systems. Relevance of the experiments to the Gen-IV systems will possibly be evaluated. In the first phase, experiments carried out at the ZPR and ZPPR facilities will be considered. In the second phase, the selection will be extended to experiments that are part of the IRPHE database. After the selection is made, the chosen systems will be analyzed with the most sophisticated methodology and cross-section data in order to evaluate their performance.

Technical Summary

In the frame of the representativity analysis, a study has been carried out between the integral experiment ZPPR-2 and the large sodium-cooled fast reactor (EFR) system investigated during the extensive sensitivity analysis performed the last fiscal year.

The ZPPR Assembly 2 experimental program started in January 1971 with the purpose to meet industry's need for information applicable to the designs of 300-500 MWe liquid-metal fast-breeder reactors (LMFBRs). The reactor configuration has a two-zone core with an enrichment ratio of 1.5 (outer zone/inner zone) and equal zone volumes. The reference configuration has a radial reflector made of mild steel block inserted directly into the matrix tubes. The axial reflector in "half one" was sodium and steel, 8 inches thick, in an approximate 50%-50% combination, while the axial reflector in "half two" was solid steel, 5 inches thick. The difference was due to material inventory considerations. The radial blanket is divided into two subregions because of material considerations, which resulted in slightly different steel and sodium densities in the two portions of the blanket. Finally, a spring gap, consisting of holding springs, drawer back plates and drawer fronts, was used.

Geometry and homogenized compositions characterizing the ZPPR-2 model used in the present calculation are presented in Table 1. In the original reactor configuration, the axial reflectors "half one" and "half two" were built as half cylinders. Because of the RZ representation allowed by the BISTRO code of ERANOS, the two axial reflectors were modeled as nested rings (the original volumes were preserved). The details of the EFR system selected for the representativity analysis with the ZPPR-2 may be found in any of the publications made during the last fiscal year on the sensitivity/uncertainty analysis.

Table 1. ZPPR-2: Geometry and Compositions [10^{24} at/cm^3]

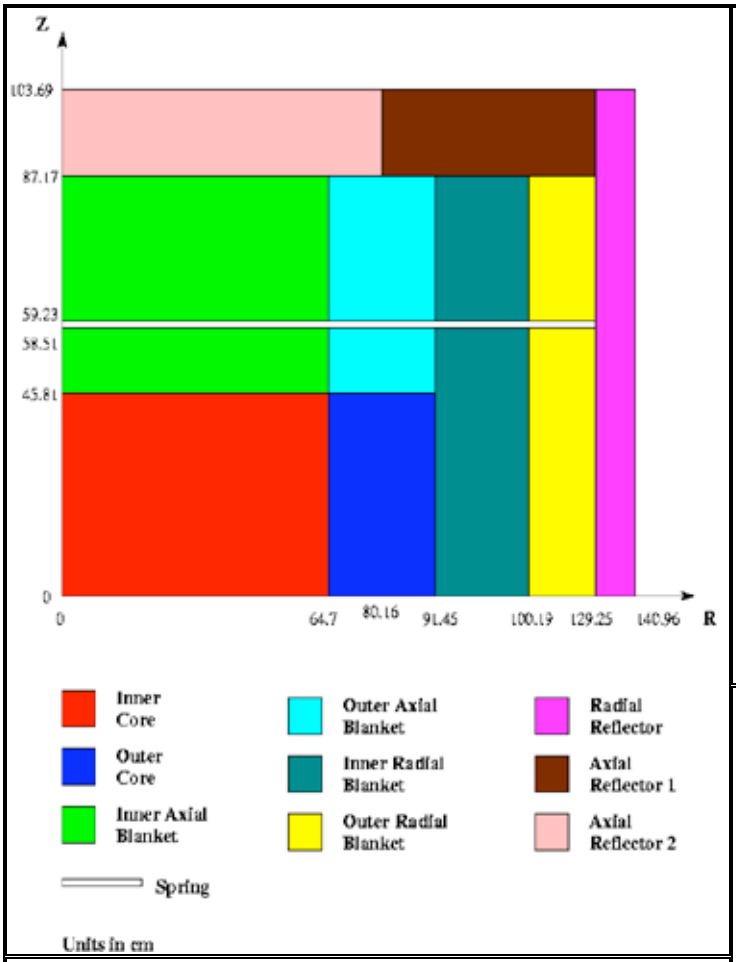

	Inner Core	Outer Core
Pu239	8.433E-4	1.274E-3
Pu240	1.117E-4	1.687E-4
Pu241	1.530E-5	2.310E-5
Pu242	1.800E-6	2.800E-6
Pu238	6.000E-7	9.000E-7
Am241	2.900E-6	4.300E-6
U235	1.230E-5	1.150E-5
U238	5.555E-3	5.198E-3
C	3.000E-5	2.300E-5
O	1.312E-2	1.176E-2
Na	8.796E-3	8.564E-3
Al	3.000E-6	4.000E-6
Fe	1.258E-2	1.385E-2
Cr	2.702E-3	2.523E-3
Ni	1.221E-3	1.160E-3
Mn	2.090E-4	2.020E-4
Cu	1.900E-5	2.000E-5
Mo	2.310E-4	3.410E-4
Si	1.370E-4	1.180E-4

	Radial Reflector	Spring
C	5.580E-4	2.840E-4
Al	-	1.000E-6
Fe	7.516E-2	2.113E-2
Cr	1.205E-3	4.393E-3
Ni	5.130E-4	1.503E-3
Mn	5.980E-4	2.790E-4
Cu	1.300E-5	3.000E-5
Mo	1.200E-5	2.300E-5
Si	9.100E-5	1.820E-4

	Inner Radial Blanket	Outer Radial Blanket	Inner Axial Blanket	Outer Axial Blanket
U235	2.400E-5	2.400E-5	1.600E-5	1.600E-5
U238	1.109E-2	1.109E-2	7.036E-3	7.057E-3
C	1.013E-3	1.013E-3	3.600E-5	3.000E-5
O	2.013E-2	2.013E-2	1.390E-2	1.401E-2
Na	6.398E-3	5.963E-3	8.739E-3	8.808E-3
Al	2.000E-6	3.000E-6	2.000E-6	2.000E-6
Fe	6.923E-3	7.541E-3	1.075E-2	9.355E-3
Cr	1.991E-3	2.172E-3	2.835E-3	2.418E-3
Ni	8.980E-4	9.870E-4	1.275E-3	1.095E-3
Mn	1.570E-4	1.740E-4	2.300E-4	2.050E-4
Cu	1.700E-5	1.800E-5	1.700E-5	1.700E-5
Mo	1.400E-5	1.500E-5	1.400E-5	1.400E-5
Si	9.400E-5	1.020E-4	1.500E-4	1.190E-4
H	8.000E-6	8.000E-6	-	-

	Axial Reflector 1	Axial Reflector 2
C	2.140E-4	5.570E-4
Na	8.966E-3	
Al	2.000E-6	
Fe	3.571E-2	7.227E-2
Cr	5.347E-3	1.639E-3
Ni	2.412E-3	7.060E-4
Mn	6.110E-4	6.230E-4
Cu	1.700E-5	1.400E-5
Mo	1.400E-5	1.300E-5
Si	3.050E-4	1.140E-4

With respect to the ZPPR-2, the EFR core has a larger size (including the blanket: 21000 liters compared to 9000 liters). We also recall that the EFR has a 1% minor-actinides loading, while the ZPPR-2 contains no minor actinides.

The obtained multiplication factor for ZPPR-2 is 0.985834. Particular care was devoted to the coolant-void reactivity coefficient, which results in opposite sign compared to the EFR case. Defining the coolant-void coefficient as the reactivity difference between the voided and the reference configuration, the value is -767.3 pcm for the ZPPR-2 and +1934.5 pcm for the EFR. A perturbation analysis was performed for the two reactors. As expected, due to the smaller size, the ZPPR-2 leakage component gives a very large negative contribution greater than the spectral component and therefore the final negative sign for the total value.

As in the previous cases, the representativity analysis was carried out with respect to the following integral parameters: K_{eff}, coolant void reactivity coefficient, β_{eff}, $\eta=<\nu\Sigma_f\Phi>/<\Sigma_a\Phi>$, and the spectral indices $<\sigma_{f,U8}\Phi>_{pos1}/<\sigma_{f,Pu9}\Phi>_{pos1}$ (with pos1 referring to the center core position), $<\sigma_{f,U8}\Phi>_{pos2}/<\sigma_{f,U8}\Phi>_{pos3}$ and $<\sigma_{f,Pu9}\Phi>_{pos2}/<\sigma_{f,Pu9}\Phi>_{pos3}$ (with pos2 referring to the radial location at 5 cm from the blanket boundary inside the reflector and pos3 referring to the radial location inside the blanket at 5 cm from the interface with the reflector).

The results of this representativity analysis are provided in Table 2, where absolute values, total and reduced uncertainties for each integral parameter are shown. It can be observed that good representativity factors are observed for the integral parameters K_{eff}, β_{eff} and η: the values are close among themselves as well as to the optimum value 1. In the case of the spectral indices at the interface blanket/reflector, the representativity also shows good results. On the contrary, a low value for the representativity factor appears for the spectral index $<\sigma_{f,U8}\Phi>_{pos1}/<\sigma_{f,Pu9}\Phi>_{pos1}$ at the core center, which is likely due to a dissimilarity of the sensitivity profiles at low energy rather than at high energy. More investigations are needed on this aspect. Finally, it is important to notice that the representativity factor in the case of the coolant-void reactivity coefficient shows a negative value. In fact, according to the formula giving the representative factor for an integral parameter R

$$r_{RE} = \frac{\left(S_R^+ D S_E\right)}{\left[\left(S_R^+ D S_R\right)\left(S_E^+ D S_E\right)\right]^{1/2}}$$

, where D is covariance matrix and S_R and S_E are the sensitivity matrix associated to R for the reactor and the experiment respectively), negative values are expected for those cases where the sensitivity profiles related to the two systems object of the representativity analysis show important components of opposite sign associated to the same isotope data. It is worth noting that negative representativity factors are as useful as positive ones if they are close to -1. In this latter case, a perfect anti-correlation between the experiment and the target reactor is established so that the total uncertainty can be correspondingly reduced.

Work continued on the representativity study of Assembly 53 of the integral experiment ZPR-3. For completeness, the representativity study was carried out with respect to all fast systems investigated during the extensive sensitivity analysis performed the last fiscal year (GFR, EFR, SFR and LFR), even though it is known that Assembly 53 would show a poor similarity with some fast reactors, like the LFR, with quite different features. In this way, not only the similarities, but also the differences among the investigated systems could be highlighted.

Table 2. ZPPR-2 Representativity and Uncertainty (%) Results

	R = EFR E = ZPPR-2	R = EFR E = ZPPR-2	R = EFR E = ZPPR-2	R = EFR E = ZPPR-2
Integral Parameter	**K_{eff}**	**Coolant Void Coefficient**	**β_{eff} (**)**	$\frac{\langle \nu\Sigma_f \Phi \rangle}{\langle \Sigma_a \Phi \rangle}$ (**)
Absolute Value in R:	1.108481	1934.5 pcm	206.2 pcm	2.94
Absolute Value in E:	.985834	-767.3 pcm	217.3 pcm	2.921
Total Uncertainty in R:	1.02	8.40	0.70	0.04
Total Uncertainty in E:	1.23	30.82	0.61	0.03
Representativity factor:	**0.954**	**-0.724**	**0.964**	**0.965**
Reduced Uncertainty in R:	0.31	5.80	0.19	0.01
Integral Parameter	$\frac{\langle \sigma_{f,U8} \Phi \rangle_{pos1}}{\langle \sigma_{f,Pu9} \Phi \rangle_{pos1}}$	$\frac{\langle \sigma_{f,U8} \Phi \rangle_{pos2}}{\langle \sigma_{f,U8} \Phi \rangle_{pos3}}$	$\frac{\langle \sigma_{f,Pu9} \Phi \rangle_{pos2}}{\langle \sigma_{f,Pu9} \Phi \rangle_{pos3}}$	
Absolute Value in R:	0.025	3.139	0.586	
Absolute Value in E:	0.024	3.939	1.679	
Total Uncertainty in R:	4.85	3.81	1.43	
Total Uncertainty in E:	7.33	7.51	1.53	
Representativity factor:	**0.24**	**0.904**	**0.806**	
Reduced Uncertainty in R:	4.71	1.62	0.85	

(**) Direct effect only

Assembly 53 was the fourth in a sequence of plutonium-fueled ZPR-3 assemblies with simple geometries and material compositions, the first three being Assemblies 48, 49 and 50. Although the critical masses of the assemblies in this sequence were small, their neutron spectra were generally similar to those expected in large fast power reactors. The objective of the assemblies in this sequence is to provide integral data for evaluation of calculational methods and nuclear-data compilations to be employed in the design of demonstration plant liquid-metal fast-breeder reactors (LMFBRs). The core constituents of the assemblies in this series have been limited to plutonium, depleted uranium, sodium, graphite, and the steel content of the ZPR matrix and drawers. Assembly 53 contains no sodium, this having been replaced by graphite in progressing from Assembly 48 (with Na), to Assembly 49 (voided) and then to Assembly 50 (graphite in place of Na-void). In the core compositions of Assembly 53, graphite was substituted by depleted uranium, thereby reducing the U/Pu ratio from 4.1 to 1.6. In all assemblies, the core compositions were based on a 2.2-inch-wide cell (a ZPR-3 matrix unit) to simplify the analysis of reactor properties. Assembly 53 was surrounded by a 12-inch-thick depleted uranium blanket.

The calculations performed in the present analysis for the ZPR-3 Assembly 53 reactor use a simplified RZ model with homogenized compositions (see Table 3). The representativity analysis was performed with respect to the following integral parameters: K_{eff}, β_{eff}, $\eta=\langle \nu\Sigma_f\Phi \rangle / \langle \Sigma_a\Phi \rangle$, and the spectral indices $\langle \sigma_{f,U8}\Phi \rangle / \langle \sigma_{f,Pu9}\Phi \rangle$ at the center core position. The results of this analysis are provided in Table 4 where representativity factors and reduced uncertainties are shown. Beside the EFR, a fairly good representativity is also observed between Assembly 53 and the GFR reactor. As expected, a poor similarity is shown with respect to the LFR reactor.

Table3. ZPR-3 Assembly 53: Geometry and Compositions [10^{24} at/cm^3].

	Core	Blanket
U235	6.1000E-06	8.3000E-05
U238	2.6100E-03	3.9770E-02
Pu239	1.6610E-03	-
Pu240	1.0700E-04	-
Pu241	1.1400E-05	-
Al27	1.1100E-04	-
Mo	2.0800E-04	-
Fe	7.4740E-04	4.8470E-03
Ni	8.1400E-04	5.2800E-04
Cr	1.8590E-04	1.2050E-03
Mn	7.7600E-05	5.0000E-05
Si	9.1000E-05	5.9000E-05
C	5.5811E-02	-

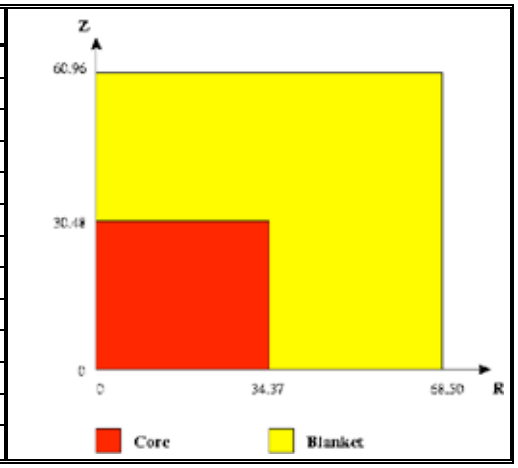

Table 4. ZPR-3 Assembly 53 Representativity and Uncertainty (%) Results.

E = ZPR-3 Assembly 53	R = GFR	R = EFR	R = SFR	R = LFR
Integral Parameter	K_{eff}	K_{eff}	K_{eff}	K_{eff}
Absolute Value in R:	1.010489	1.108482	1.052802	1.000228
Absolute Value in E:	.976549	.976549	.976549	.976549
Total Uncertainty in R:	1.13	1.02	1.10	1.51
Total Uncertainty in E:	1.04	1.04	1.04	1.04
Representativity factor:	**0.659**	**0.805**	**0.488**	**0.585**
Reduced Uncertainty in R:	0.85	0.61	0.96	1.23
Integral Parameter	β_{eff}	β_{eff}	β_{eff}	β_{eff}
Absolute Value in R:	366.1 pcm	334.3 pcm	264.6 pcm	314.8 pcm
Absolute Value in E:	328.9 pcm	328.9 pcm	328.9 pcm	328.9 pcm
Total Uncertainty in R:	0.83	0.70	0.64	0.78
Total Uncertainty in E:	0.50	0.53	0.53	0.51
Representativity factor:	**0.584**	**0.811**	**0.447**	**0.414**
Reduced Uncertainty in R:	0.68	0.41	0.57	0.71
Integral Parameter	$\frac{\langle \nu\Sigma_f\Phi\rangle}{\langle \Sigma_a\Phi\rangle}$	$\frac{\langle \nu\Sigma_f\Phi\rangle}{\langle \Sigma_a\Phi\rangle}$	$\frac{\langle \nu\Sigma_f\Phi\rangle}{\langle \Sigma_a\Phi\rangle}$	$\frac{\langle \nu\Sigma_f\Phi\rangle}{\langle \Sigma_a\Phi\rangle}$
Absolute Value in R:	2.945	2.942	3.027	2.943
Absolute Value in E:	2.938	2.938	2.938	2.938
Total Uncertainty in R:	0.04	0.04	0.05	0.05
Total Uncertainty in E:	0.02	0.02	0.02	0.02
Representativity factor:	**0.769**	**0.756**	**0.579**	**0.261**
Reduced Uncertainty in R:	0.02	0.02	0.04	0.05
Integral Parameter	$\frac{\langle \sigma_{f,U8}\Phi\rangle_{pos1}}{\langle \sigma_{f,Pu9}\Phi\rangle_{pos1}}$	$\frac{\langle \sigma_{f,U8}\Phi\rangle_{pos1}}{\langle \sigma_{f,Pu9}\Phi\rangle_{pos1}}$	$\frac{\langle \sigma_{f,U8}\Phi\rangle_{pos1}}{\langle \sigma_{f,Pu9}\Phi\rangle_{pos1}}$	$\frac{\langle \sigma_{f,U8}\Phi\rangle_{pos1}}{\langle \sigma_{f,Pu9}\Phi\rangle_{pos1}}$
Absolute Value in R:	0.028	0.025	0.025	0.015
Absolute Value in E:	0.032	0.032	0.032	0.032
Total Uncertainty in R:	4.77	4.85	4.75	8.35
Total Uncertainty in E:	3.46	3.54	3.54	3.53
Representativity factor:	**0.870**	**0.883**	**0.835**	**0.451**
Reduced Uncertainty in R:	2.36	2.28	2.61	7.45

Cross Section Measurements

Fission Cross-Section Measurement

The analysis of the ^{237}Np fission measurement was completed last quarter. The cross section data was submitted to the evaluators of the LANL Group T-16 to meet the milestone. The LANSCE data has now been included in a new evaluation of this cross section above the resolved resonance region and has been submitted to the ENDF/B-VII library. The data taken at LANSCE for ^{237}Np(n, fission) is compared to the new evaluation as shown in Fig. 7. A paper on the ^{237}Np results is in progress, and will be submitted to *Physical Review C*.

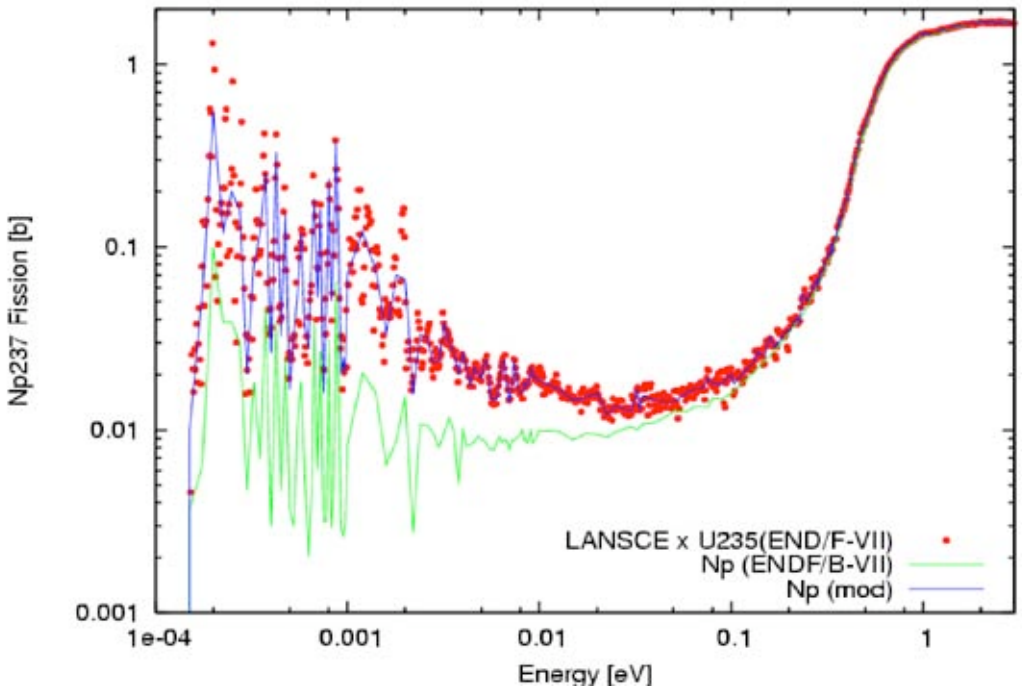

Fig. 7. Fission cross section of ^{237}Np. The red points are data measured at LANSCE in 2005. The green line shows the current ENDF/B-VII evaluation, and the blue line the new evaluation performed at LANL.

The ^{237}Np measurements at LANSCE improved the uncertainties and resolved discrepancies between the existing evaluations. It also served as a benchmarking case, since the fission cross section is better known compared to other isotopes for which data is requested by the program. In that sense, it was an appropriate first case to incorporate correlations in the reported uncertainties of the fission measurements. This issue is now being addressed in a corporate collaboration between experimentalists and evaluators at LANL. The final goal of this project is to produce the corresponding correlation matrix for each cross-section evaluation.

The analysis of the ^{242}Pu and ^{240}Pu fission cross-section data continued. One of the outcomes of the ^{242}Pu data analysis was that a resonance missing in the ENDF/B-VII evaluation was identified. The 2.5-eV resonance appears in the JENDL-3.3 evaluation, but not in the ENDF/B-VII evaluation. Although the analysis is not

complete, since the correction for ^{241}Pu contamination still needs to be performed, the data clearly identifies a resonance at 2.5 eV. The correction for the ^{241}Pu contamination will ideally be performed using data obtained using the same data acquisition system used for ^{242}Pu and ^{240}Pu. A request for a ^{241}Pu fission target was submitted to the target fabricators at Idaho National Laboratory. Very little beam time will actually be required to gain the necessary background shape.

The ^{242}Pu and ^{240}Pu measurements performed during the last beam cycle of LANSCE were carried out at the Lujan center, hence ranging in neutron energy up to 200 keV. In the upcoming beam cycle, the plan is to extend the energy range to 200 MeV by going to the WNR facility. Beam time has been requested, and the proposal was presented and the LANSCE PAC. The proposal was well received.

The tests with a Frisch-gridded ionization chamber for fission studies continued. The chamber is on loan from the Institute of Reference Material and Measurements (IRMM) in Belgium, and has been used extensively in the past for fission fragment spectroscopy. The strength of using a gridded chamber with transparent sample backing is that both fission fragments are detected in coincidence, hence allowing for a better fission / alpha separation. The chamber is planned to be used for radioactive samples that are too active to be measured with the current experimental setup.

Capture Cross-Section Measurement

The energy calibration of the DANCE detector array for the ^{242}Pu(n,γ) measurement campaign was completed. The calibration technique was designed to be sufficiently general to allow easy application to the ^{240}Pu(n, γ) measurements. Additional beam time was requested for ^{240}Pu, ^{242}Pu, and ^{239}Pu in order to improve the statistics, particularly in the 1 keV – 1 MeV region, as well as identify contaminants of ^{239}Pu in the other Pu samples. Eleven additional days of beam time have been allocated in May.

The DANCE detector array consists of 160 individual detectors requiring independent energy calibration to generate a reliable Q-value sum, one of the primary advantages of a 4-pi array. An initial energy calibration was done by performing a simultaneous fit to multiple γ-ray standards as can be seen in Fig. 8. Simulations using GEANT3 were performed to determine the detection efficiency for different energy γ-rays. Physics effects, including Compton scattering edges, were included to properly place the peak centroids—the most essential result.

A typical deficiency of BaF_2 detector material is the presence of Ra radioactive-decay products that cannot be completely removed from a large sample of Ba. When these contaminants α-decay, the α particles are detected with high efficiency in the detector. Fortunately, they can be cleanly separated from the γ-rays by comparing the fast and slow responses of the detector as shown in Fig. 9. Then a clean γ-spectrum and clean α-spectrum can be obtained.

Once a careful calibration was made of the γ-rays with sources, the equivalent α-energy was calculated on a detector-by-detector basis. These γ-equivalent alpha energies can then be used to calibrate the detectors on a run-by-run basis without stopping between each run to put in γ-calibration sources. The α background was used in this way to provide an intrinsic calibration that is available simultaneous with measurements of the Pu samples.

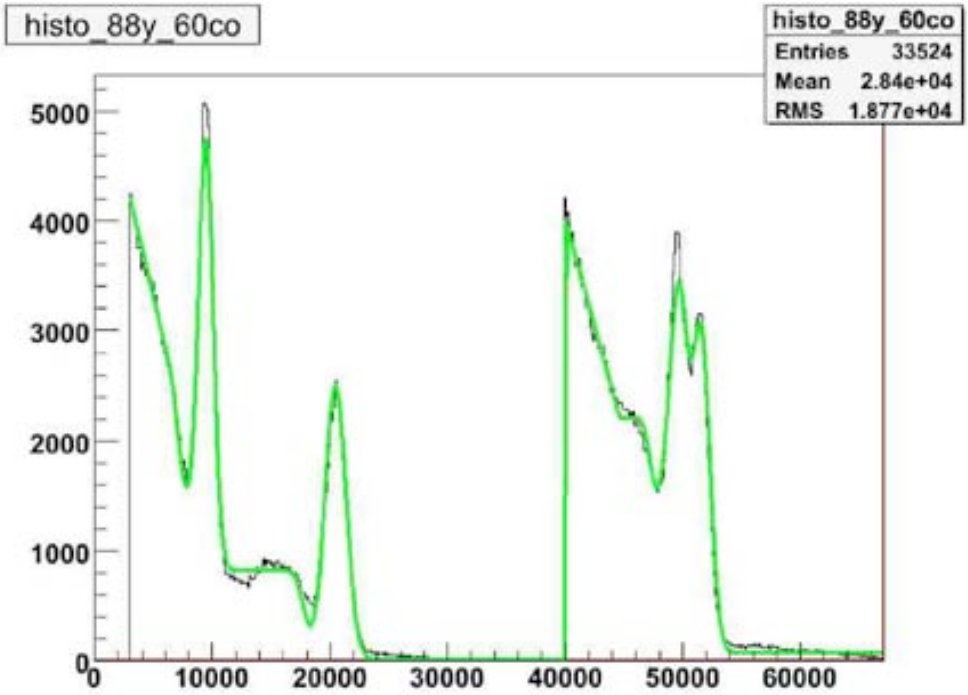

Fig. 8. Typical fit to 88-Y and 60-Co are shown. The x-axis is the integrated pulse height from the flash ADC digitizer. The fit is overlaid in green on top of the black data.

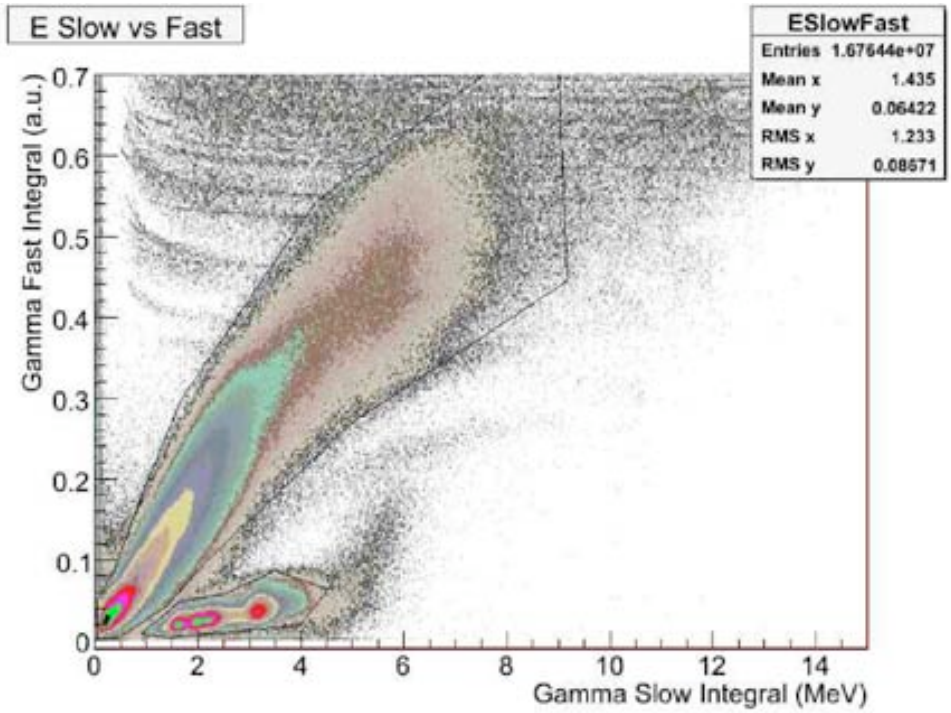

Fig. 9. 2-D histogram showing the fast vs. slow components of the BaF_2 detector signal. The γ-rays lie in the large band that runs about 60º above the horizontal. The α-band is almost horizontal, allowing an easy separation of the two different components.

The initial energy calibration of the DANCE array shows promising results for the determination of the capture cross-sections. Shown in Fig. 10 is the total gamma energy gated on a neutron energy region where ^{242}Pu capture is expected to dominate. Note how cleanly the Q-value of the reaction can be seen. By applying cuts in Q-value, neutron energy and Time-of-Flight, the situation is quite promising for the final determination of the capture cross-section.

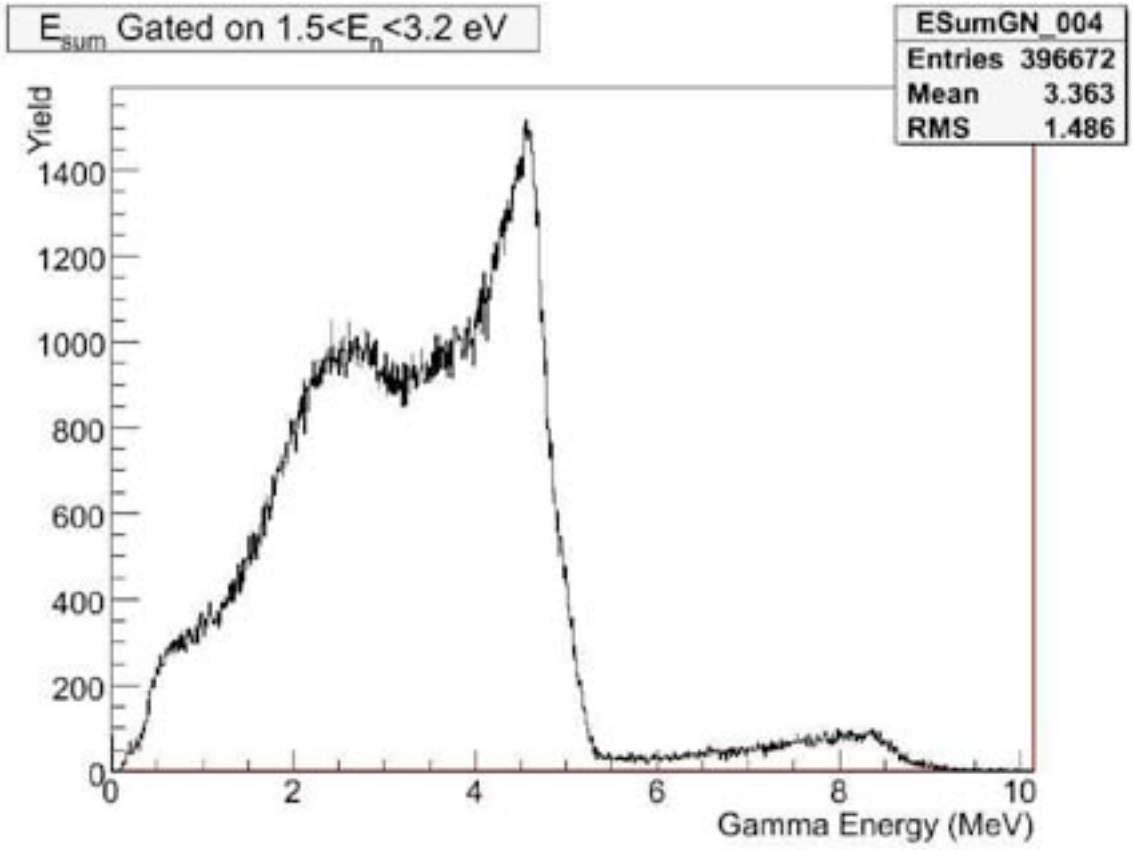

Fig. 10. Shown is the γ-energy sum near the Q-value of 5.034 MeV. The peak is shifted slightly below the Q-value due to losses in the array.

Gas Production Cross-Section Measurements

Hydrogen and helium are produced when energetic neutrons interact with materials, and these gases can lead to significant changes in materials properties such as embrittlement and swelling. Such effects have been seen in fission reactors and a significant effort has been made for the development of fusion reactors where the effects are expected to be larger because of the higher neutron energy. For AFCI, new structural materials are proposed, and the amount of gas production must be known to assess the properties of these materials under radiation damage.

Hydrogen and helium gases are produced initially as protons, deuterons and alpha particles from nuclear reactions. When these charged particles slow down and stop (with ranges of mm to cm), they acquire electrons from the material and become hydrogen (protons and deuterons) or helium (alpha particles). Our method is to

measure the protons, deuterons and alpha particles that escape from thin foils as illustrated Fig. 11.

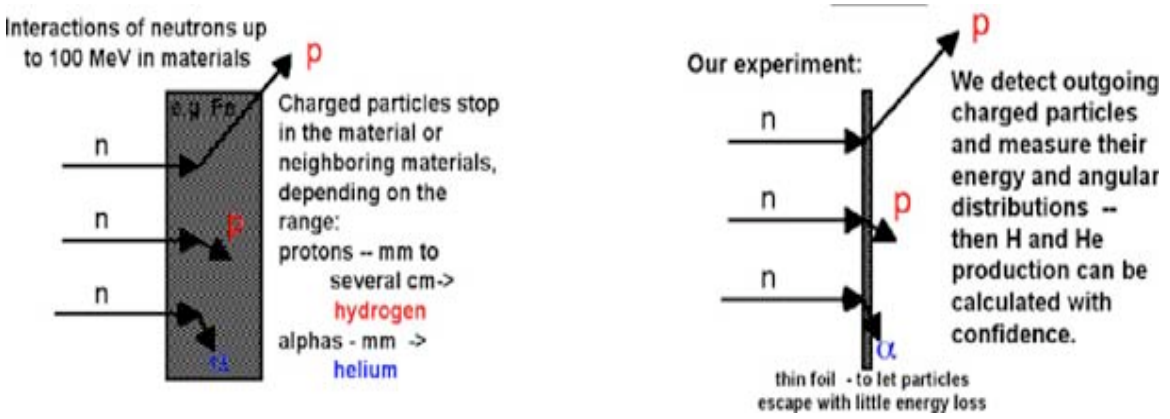

Fig. 11. Interactions of neutrons with materials produce charged particles that stop either in the material or in neighboring materials. In our experiment, we use a thin foil of the material so that the charged particles can escape and be detected.

We measure the charged particles with detector systems at four angles concurrently. Then we can move the detector systems to investigate a new set of angles. Each detector system consists of 2 or 3 detectors in coincidence and arranged so that the charged particles pass through the first detector and stop in the second or third. We do this in order to identify the protons, deuterons, and alpha particles and also the small number of tritons and ^{3}He. A photograph of the chamber is given in Fig. 12. Typical identification of helium ion products is given in Fig. 13.

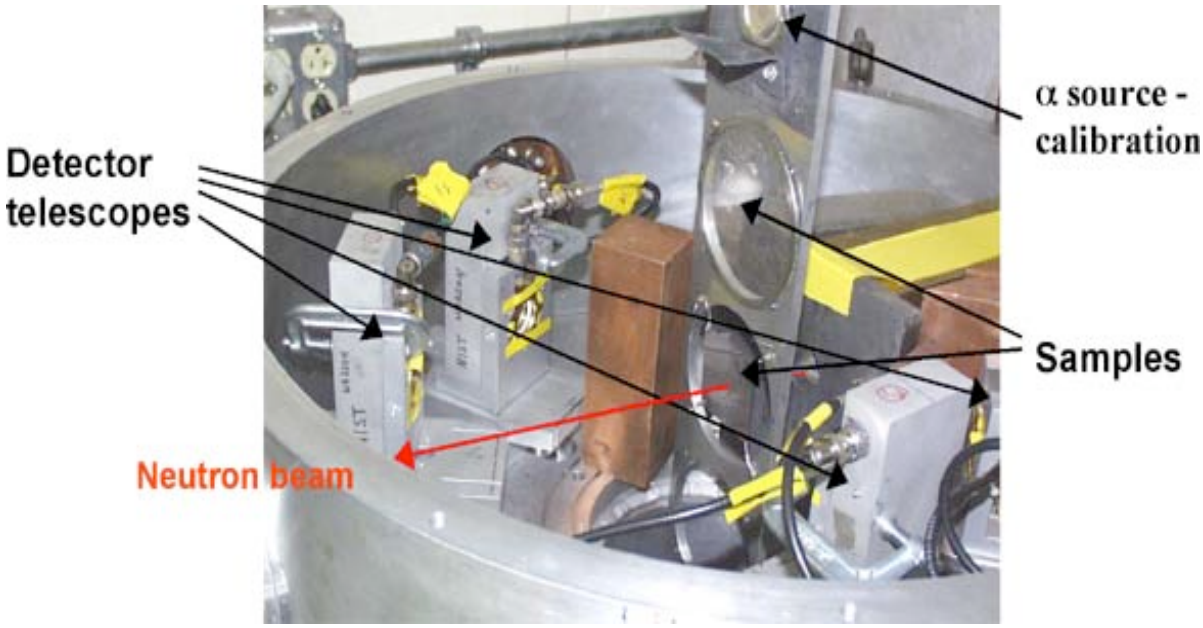

Fig. 12. Photo of the chamber, detectors and samples used in the measurement of hydrogen and helium production.

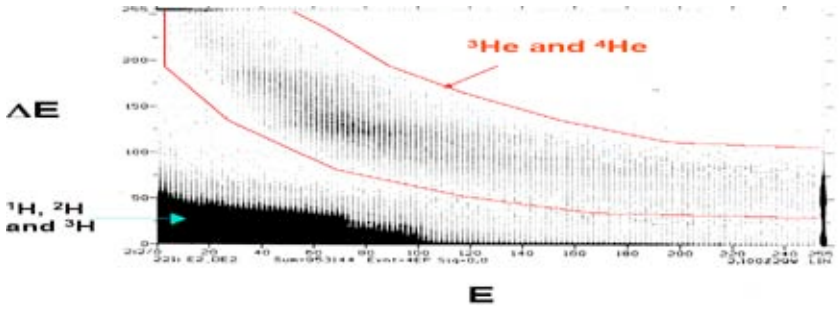

Fig. 13. Data from the detector telescopes allow us to separate reaction products: hydrogen isotopes from helium isotopes. The scales on the axes are channel numbers and are proportional to the energy deposited in the ΔE and E detectors.

The LANSCE accelerator was down for scheduled maintenance this quarter. It is scheduled to resume production operation in early May. During this downtime, we performed calibration measurements and tested some possible improvements to the detector systems. A new type of counter gas (Xe +10% CO_2 instead of pure Xe) was tested and, although it did not offer improved performance, it was no worse. Because we have a good supply of this new gas, we will be using it for the upcoming runs. We are designing a new type of gas detector, an ionization chamber rather than a proportional counter, to get better resolution and thereby separate the isotopes of helium as well as those of hydrogen. The data so obtained will provide more stringent tests of nuclear reaction models used to calculate gas-production cross sections that cannot be measured with present technologies.

We participated in the Joint AFCI/Gen-IV Physics Working Group Meeting held in Salt Lake City, Utah in January, and presented a talk entitled "AFCI Gas Production Measurements: Status through 1Q FY2006." Results for chromium were highlighted (Figs. 14 and 15).

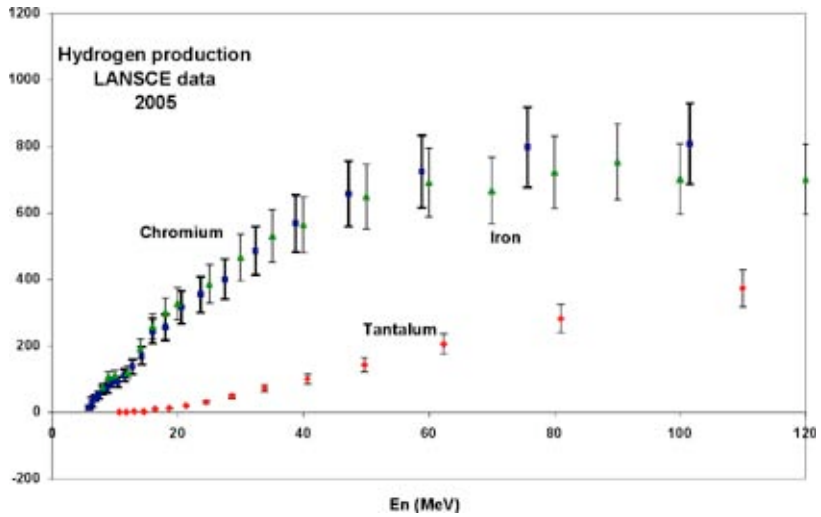

Fig. 14. H-production cross sections for neutrons on Fe, Ta and Cr. H-production is the sum of proton, deuteron and triton production. The 15% systematic uncertainty is the major uncertainty. Relative cross sections at neighboring energies have a much smaller uncertainty, estimated at 5%. The points are the central points of bins, the width of which is the spacing between neighboring points.

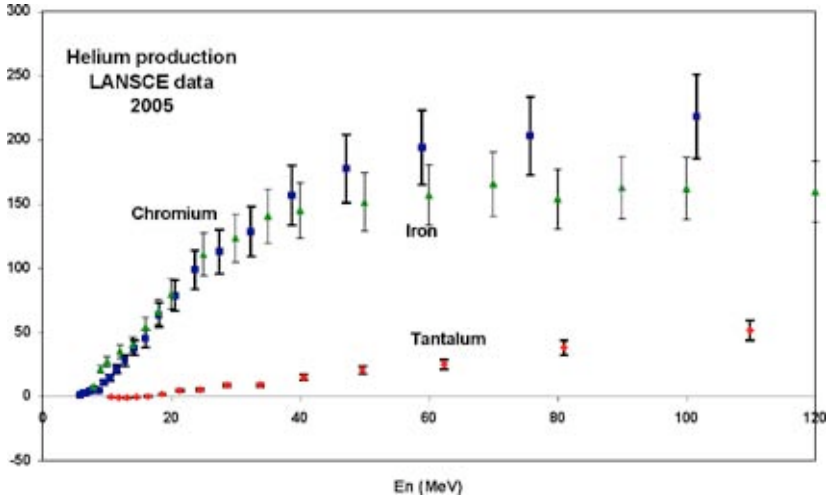

Fig. 15. He production cross sections for neutrons on Fe, Ta and Cr. He production is the sum of ^{3}He and ^{4}He production. The 15% systematic uncertainty is the major uncertainty. Relative cross sections at neighboring energies have a much smaller uncertainty, estimated at 5%. The points are the central points of bins, the width of which is the spacing between neighboring points. Previously reported cross sections for Fe (triangles) and Ta (squares) are also shown. Despite the apparent difference in the high-energy data between Cr and Fe, no such conclusion can be drawn because of the systematic uncertainties.

We completed both written (January) and oral (March) presentations of our request for beam time to the LANSCE Program Advisory Committee (PAC). The measurements proposed are a completion of the experiments on Zr and a new measurement on Mo. The recommendations of the PAC should be known in a few weeks. Their recommendations are very important because of other requests for this facility for experiments by research groups both inside LANL and from outside. The detector station for these measurements is expected to be oversubscribed, and we hope adequate beam time and intensity will be available for our gas-production measurements.

Outside of AFCI funding, we are working with Ohio University in the measurement of *(n,p)* and *(n,alpha)* cross sections on ^{13}C and ^{14}N. Reactions on nitrogen are important in the development of nitride fuels. We have completed preliminary experiments with our apparatus and identified the path forward. Complementary measurements of inverse reactions are underway at the Ohio University Accelerator Laboratory.

The next quarter will see the resumption of beam at LANSCE/WNR and the completion of measurements on Zr.

Target Preparation

Several double-sided fission foils were fabricated using 6-μm aluminized Mylar films. The films are glued to 2.3-inch-ID x 3.1-inch-OD aluminum washers. Following the fabrication, ^{252}Cf was electroplated onto one of these films. A picture of the double-sided fission foil is shown in Fig. 16. The alpha and spontaneous fission spectrum from the electroplated ^{252}Cf is shown in Fig. 17. This work completed our AFCI level-3 milestone for January.

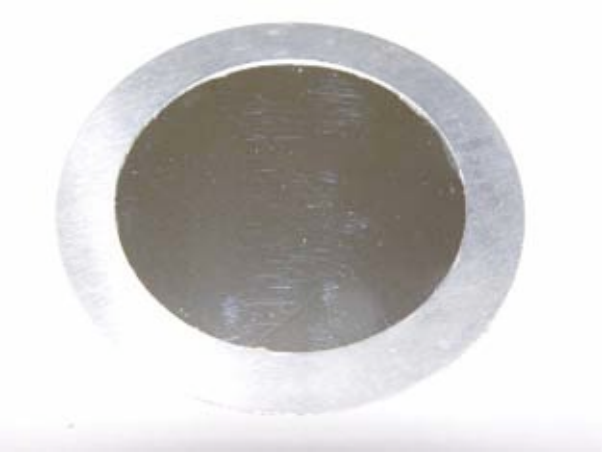

Fig. 16. Aluminized Mylar double-sided fission foil.

As can be seen from the fission spectrum in Fig. 17, the energy of the fission fragments going through the aluminized Mylar is attenuated by ~60%. To reduce the fission-fragment attenuation, we ordered and have received 0.7-μm and 0.9-μm Mylar. In a similar method to the foils above, several double-sided fission foils were fabricated using the 0.9-μm Mylar. These foils had titanium evaporated onto them at LANL, and we plan to electroplate ^{252}Cf and ^{240}Pu onto two of these foils. The ^{240}Pu will be used for a neutron-induced fission measurement at LANSCE.

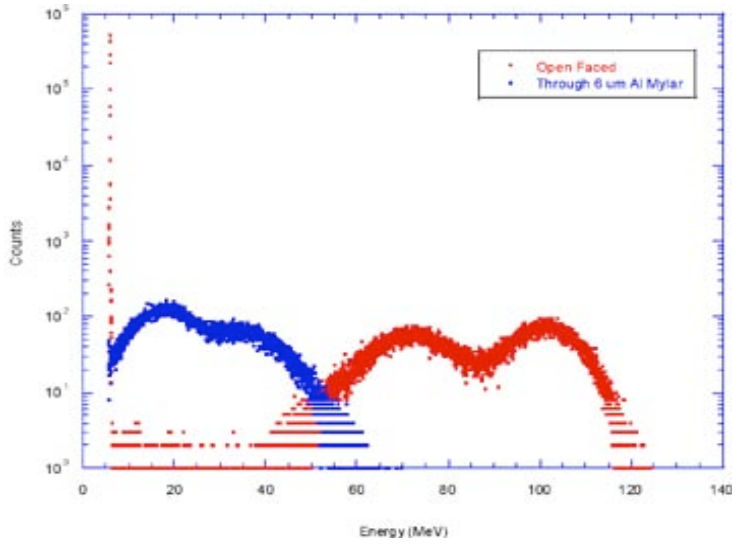

Fig. 17. Alpha and fission spectrum of electroplated ^{252}Cf from a 6-μm aluminized Mylar fission foil, both open-faced and through the Mylar.

We attended the Joint AFCI/Gen-IV Physics Working Group Meeting in Salt Lake City, UT where we presented the actinide target fabrication work.

We visited LANL and had discussions on future targets in support of AFCI/Gen-IV neutron cross-section programs. We also discussed our mass-separation capabilities and areas for potential further collaboration.

Actinide target-fabrication data was presented at the ACS meeting in Atlanta, GA in March. Many discussions were held regarding fabrication of actinide targets in potential collaboration with several universities, including UNLV and UC-Berkeley.

A journal article entitled, "Actinide Targets for Neutron Cross Section Measurements" was completed in coordination with a presentation at the MARC VII conference in Kona, HI. This article will be published in *Journal of Radioanalytical and Nuclear Chemistry*.

We purchased a rebuilt mechanical pump for our vacuum evaporator as the original pump failed. We also returned the highly calibrated HPGe detector used for target quantification to the factory for repair.

Code Development

MCNPX

The MCNPX (Monte Carlo N-Particle eXtended) radiation transport code models the interaction of radiation with matter for nearly all particle types at nearly all energies. It is extensively used by many elements of the AFCI program at Laboratories across the nation, and is probably the AFCI principal radiation analysis computational tool.

AFCI is the principal sponsor of MCNPX. Without AFCI support, it is unclear if MCNPX would survive. However, the support of AFCI and the excellence of MCNPX have enabled significant synergistic co-funding of MCNPX so that the AFCI investment is greatly leveraged.

Burnup-Depletion

The CINDER90 burnup-depletion capability in MCNPX enables a self-contained Monte Carlo transmutation capability. This is the first such capability anywhere; the alternatives are multi-step approaches linking burnup post-processors with either Monte Carlo or deterministic radiation transport codes. Having the entire code in a single package greatly simplifies the interface for users and preserves the full high fidelity of the continuous-energy Monte Carlo model.

Predictor-Corrector - In FY05, the CINDER90 burnup-depletion code was integrated into the MCNPX Monte Carlo radiation transport code along with MONTEBURNS, a code used to run these two separate codes in linked steps. That initial burnup-depletion capability has been very successfully and favorably received. However, a number of deficiencies were identified, including the need for a predictor-corrector methodology to accelerate depletion problems.

During this quarter, two methods were identified as possible predictor-corrector candidates: (1) current methodology employed in the MONTEBURNS code, and (2) methodology employed in the CELL 2 code. Both methods were coded. MOX (mixed-oxide nuclear fuel) pin cell-analysis tests comparing both linear-predictor-corrector methodologies in MCNPX to the slower, original MCNPX 2.6.A without predictor-corrector, were made to determine which method achieved acceptable results utilizing the least amount of memory and minimal computation time. Figures 18-20 display the criticality results from the completed preliminary analysis tests.

Figure 18 shows neutron multiplication results from minimizing the amount of burn steps utilizing MCNPX 2.6.A (no predictor-corrector). Figure 19 compares the 30-

step MCNPX 2.6.A. case to the different predictor-corrector methods implementing a variety of time steps (PC1 = Method 1 ; PC2 = Method 2). Figure 20 displays the EOL (end-of-life) percent difference of each case analyzed as compare with the 30-step MCNPX case. Method 1 with only 5 time steps (3X speed up = 3.46 hrs. for this case) results in only a 1.49% difference in EOL k_{eff}. Method 2 with only 5 time steps (3X speed up = 3.46 hrs. for this case) results in only a 1.55% difference in EOL k_{eff}. Both methods basically have the same percent difference within the standard deviation of the case, yet method 2 employs extra memory to be executed properly; therefore, method 1 was determined to be the best method for implementation into MCNPX 2.6.B. Implementation is now underway.

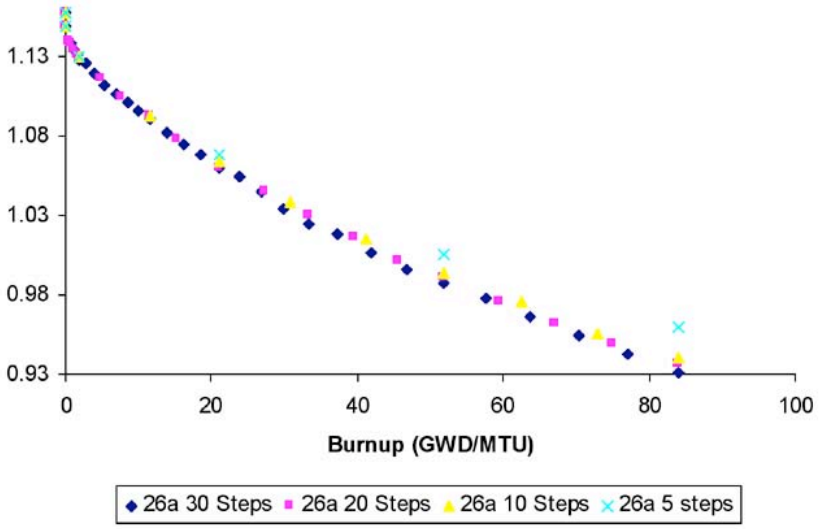

Fig. 18. MCNPX 2.6.A k_{eff} utilizing varied time steps.

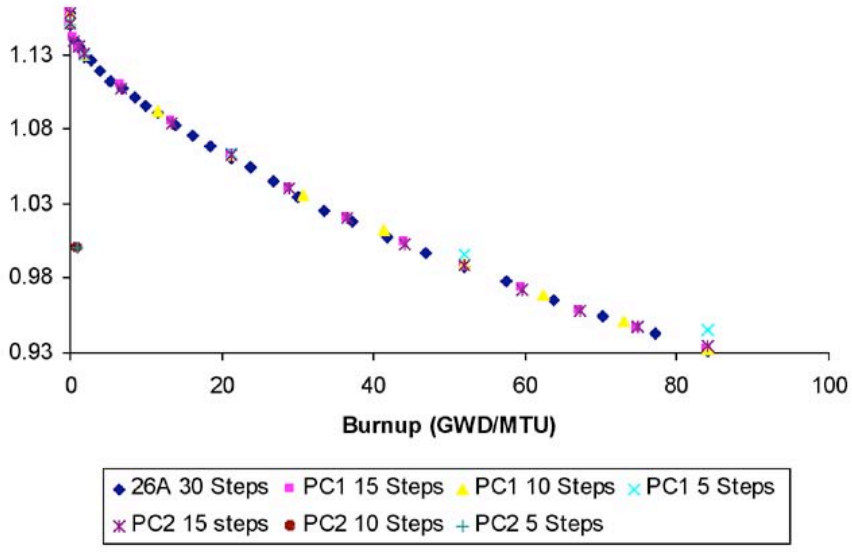

Fig. 19. MCNPX 2.6.A 30 time-step case and both predictor corrector methods' k_{eff} utilizing varied time steps.

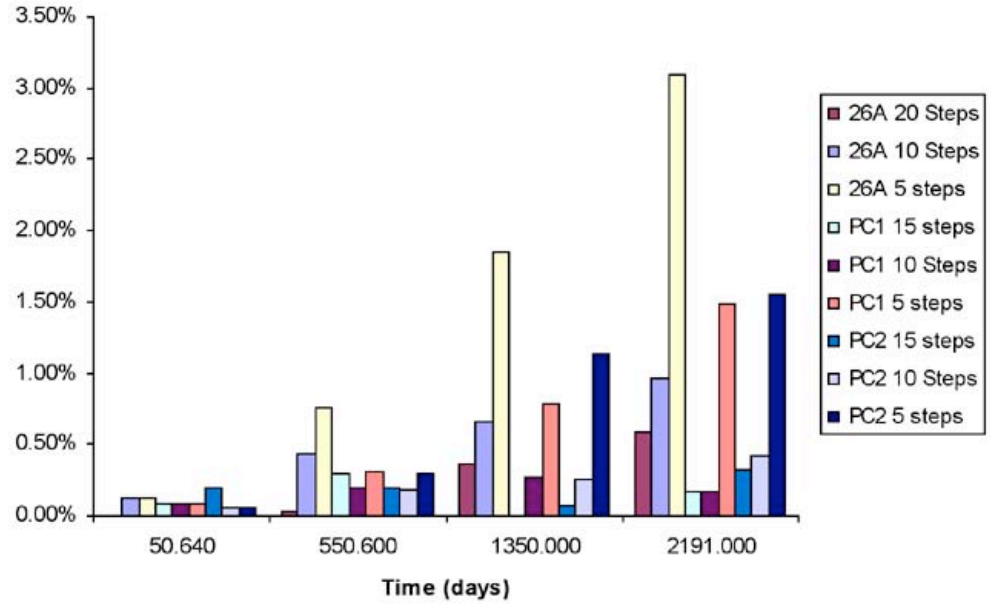

Fig. 20. Percent difference of EOL k_{eff} for each case as compared to MCNPX 2.6.A utilizing 30 time steps.

Additional Burnup-Depletion Capabilities - In addition to the predictor-corrector burnup-depletion enhancement, the following additional enhancements were made this quarter:

- Automatic selection of fission yield spectra;
- Utilizing lumped fission products to replace nuclides unavailable in the standard cross-section data libraries;
- Fixing the default settings so that the user receives a fatal error when trying to execute MCNPX without the proper Cinder library data; and
- Build-around for an Intel compiler optimization bug that created incorrect answers when running multiple materials utilizing an Intel-compiled version of MCNPX 2.6.A.

CEM03 Physics

CEM03 is the replacement physics package for CEM2K in MCNPX. This physics package makes it possible to model neutron transport for nuclides not available in the MCNPX data libraries, which is important for many applications, including depletion where many rare isotopes produced simply have no data. Further, CEM03 enables photonuclear reactions, charged-particle transport (particularly protons and light ions), and transport of neutrons above the range where ENDF data tables are unavailable.

As part of the CEM03/LAQGSM milestone for the AFCI program, CEM03 was successfully inserted into MCNPX and preliminary tests made. Further integration still remains including the LAQGSM package. Running times have been significantly improved over the initial implementation, but further improvement is being investigated. Further testing is also required. Presently the new CEM03 capability

appears to interfere with the INCL4 physics models, and this and other problems are being addressed. The first MCNPX results with CEM03 are in Figs. 21-23.

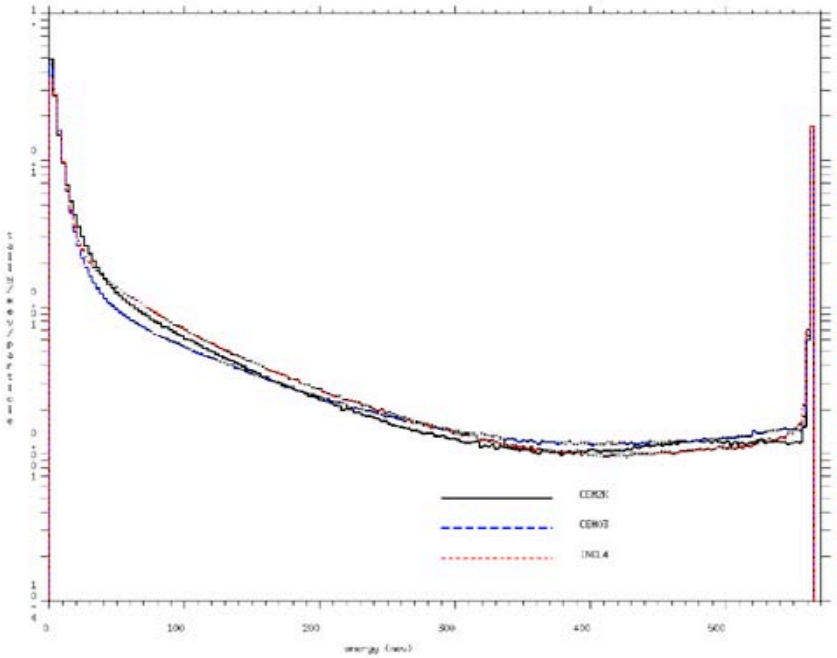

Fig. 21. Comparison of CEM03 / CEM2k, and INCL4 neutron production from 562.5-MeV neutrons bombarding Cu-64.

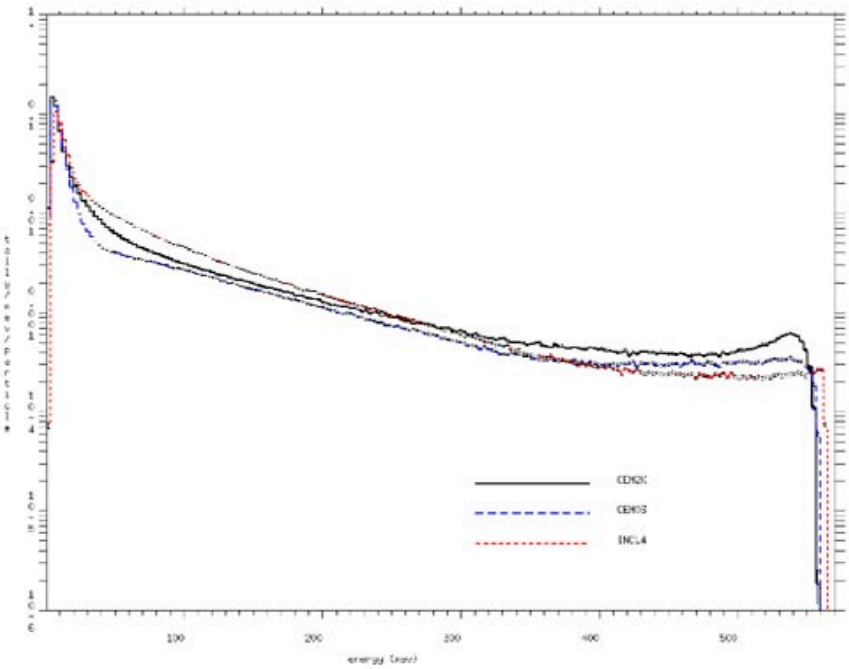

Fig. 22. Comparison of CEM03 / CEM2k, and INCL4 proton production from 562.5-MeV neutrons bombarding Cu-64.

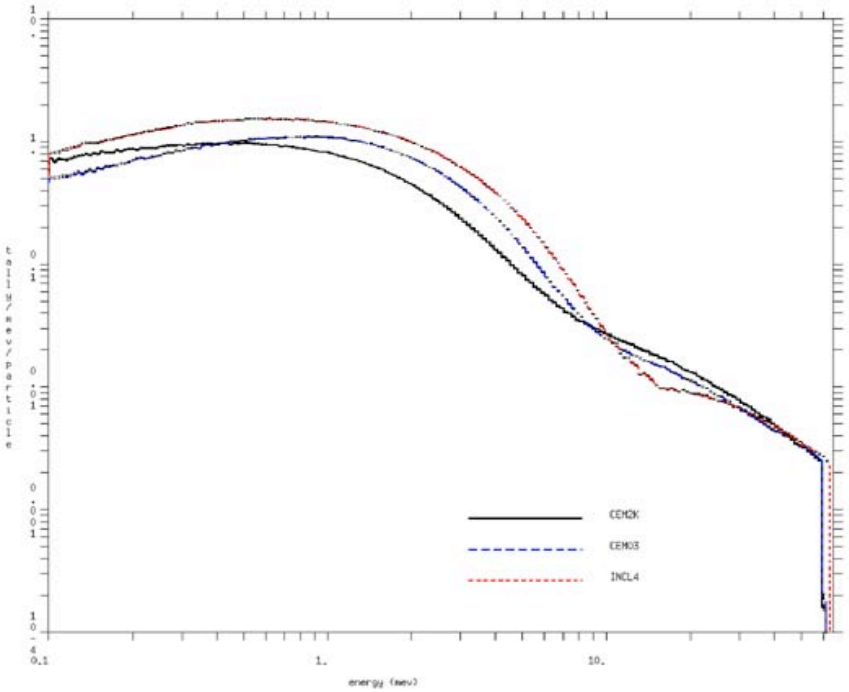

Fig. 23. Comparison of CEM03 / CEM2k, and INCL4 proton production from 62.9-MeV protons bombarding 208-Pb.

Other Activities

- A presentation was given at the AFCI/Gen IV Physics Working Group meeting held in Salt Lake City in January entitled “MCNPX: Accomplishments and Possibilities” (LA-UR-06-0765).
- The first-ever joint MCNP5/MCNPX data release from the Radiation Safety Information Computational Center, RSICC, in Oak Ridge Tennessee began in January as part of a burgeoning cooperative effort.
- The “Vacation Matrix” method for correctly estimating criticality flux distribution was, for the first time, successfully demonstrated with a large lattice of reactor fuel pins. This cooperative effort with Purdue University is essential for efficient Monte Carlo burnup calculations.
- Two MCNPX training courses were conducted, one at the University of Nevada in Las Vegas with 25 participants, and the other in Cape Town, South Africa, with 19 participants. Participant fees fund these training courses.
- There were also two half-day workshops given at the American Nuclear Society Topical Meeting on Radiation Protection and Shielding, held in Carlsbad, NM, each with over 30 participants.

Documentation

G. W. McKinney, J. S. Hendricks, J. W. Durkee, M. R. James, D. B. Pelowitz, L. S. Waters, F. Gallmeier, “Recent MCNPX Features Developed for Neutron Applications,” International Workshop on Fast Neutron Detectors and Applications, University of Cape Town, South Africa (April 3-6, 2006)

Michael L. Fensin, John S. Hendricks, Gregg W. McKinney, Holly Trellue, "Advances in Monte Carlo Depletion Capabilities for MCNPX," Los Alamos National Laboratory Report, Abstract: LA-UR-05-7895, Full paper: LA-UR-06-0629, American Nuclear Society 14th Biennial Topical Meeting of the Radiation Protection and Shielding Division, Carlsbad, New Mexico, (April 3-6, 2006)

Joshua P. Finch, John S. Hendricks, Chan K. Choi, "Fission Source Convergence in Monte Carlo Criticality Calculations," Los Alamos National Laboratory Report, LA-UR-05-7893. American

Nuclear Society 14th Biennial Topical Meeting of the Radiation Protection and Shielding Division, Carlsbad, New Mexico, (April 3-6, 2006)

M. James, G. McKinney, J. Hendricks, and M. Moyers, "Heavy-Ion Transport in MCNPX," Los Alamos National Laboratory Report, LA-UR-05-8338, American Nuclear Society 14th Biennial Topical Meeting of the Radiation Protection and Shielding Division, Carlsbad, New Mexico, (April 3-6, 2006)

Structural Materials

Scope

The objective of the materials program is to qualify the structural materials of interest to a high-flux and high-fluence irradiation environment with high-energy particles relevant to fast-spectrum transmutation. This fiscal year we will test specimens from FFTF (Fast Flux Test Facility) irradiations including the ACO3 duct and MOTA (Materials Open Testing Assembly) irradiated specimens. We will receive specimens at PNNL from FFTF irradiations. Specimens will be shipped to PSI (Paul Scherrer Institute in Switzerland) for the STIP V irradiation.[1] We will also perform tensile tests on STIP III irradiated HT-9 and EP-823 at room temperature and 400ºC. Data will be shared with EUROTRANS and CEA[2] collaborations.

To test the effects of irradiation on the mechanical properties of ferritic-martensitic (F-M) steels, irradiated EP823 and HT-9 will be tested using tensile and shear-punch tests. The tensile test has been in use for many years and provides mechanical properties directly, while the shear-punch test is not as straight forward in that it requires some level of calculation and interpretation. However, the shear-punch test is very useful when tensile specimens are not available. In an attempt to augment the data from earlier work at low temperatures (25ºC–200ºC), tests will be performed after irradiation at 250ºC–350ºC and doses of up to 25 dpa. These new tests will

[1] Spallation Target Irradiation Program (at PSI)
[2] Commissariat à l’Energie Atomique (France)

significantly extend the data available for design and maintenance consideration for new accelerators.

A large cache of high-dose irradiated ferritic-martensitic (f-m) steel mechanical test and microscopy specimens reside in storage boxes located in the Building 324 on the Hanford Site in Richland, WA. These specimens are of great value to the AFCI materials program. Building 324 is scheduled to be decommissioned and shut down. These specimens will be retrieved this year and shipped to labs for analysis. Transmission Electron Microscopy (TEM) analysis, tensile and Charpy testing will be performed on FFTF and STIP irradiated materials.

Transmutation efficiency is directly related to the material lifetime limits caused by radiation damage. This is true for both the ADS (Accelerator-Driven Systems) and fast reactor (Gen-IV) options for transmutation. It is impossible to test materials for all possible spectra. Thus, modeling is essential to fill in the details for an informed technology decision in five years. The FY06 scope centers on modeling bubble formation in Fe-Cr materials. Large-scale atomistic simulations of cascade damage in Fe-Cr systems will be performed as a function of incident ion energy (9–12 wt% Cr is the region of interest). Defect distribution from these calculations will be used as an input in KMC simulations. In parallel, Kinetic Lattice Monte Carlo (KMC) simulations will be performed to include Cr into the Fe system. We will investigate segregation and explore He bubble formation in the Fe-Cr system using atomistic simulations data wherever possible. This program will include collaborations with International partners (EUROTRANS and CEA collaboration) and collaborating with University of Illinois in the UNERI (University Nuclear Energy Research Initiative) program.

Highlights

Materials Testing

- Shear-punch testing was completed on EP-823 and HT-9 at 25ºC and 400ºC after irradiation in the STIP II irradiation. Results mirrored those measured on much larger tensile specimens.
- Shear-punch testing was completed on tantalum and Ta-1W at 25ºC after irradiation in the APT 96-97 campaign and the STIP-II irradiation. Results show good work-hardening capacity after irradiation to up to 40 dpa.
- New test data on HT-9, T-91, EP-823 and tungsten have been compiled and added to chapters in revision 5 of the AFCI Materials Handbook. Chapters are under review.
- The 5th AFCI/Gen IV Materials Working Group meeting was organized and hosted on March 1-2, 2006. Forty researchers attended, including representatives from Gen IV, AFCI and the materials university NERI projects.

PNNL Activities

- Efforts continued on the retrieval the FFTF MOTA specimens. Three plans have been formulated and are being further investigated.

- Progress has been made on retrieving the ACO3 duct. The T3 cask is being refurbished to ship the duct to LANL in mid to late June.

Radiation Damage Modeling of Structural Materials

- We have implemented and debugged a new Fe-Cr EAM model into LAMMPS, a large-scale molecular dynamics simulation code developed by the SNL. This model was tested to ensure its accuracy and some preliminary simulations of radiation cascades were carried out. We now have a powerful capability to run cascade simulations in systems with hundreds of millions of atoms.
- The Kinetic Monte Carlo (KMC) model was used to simulate the effect of damage and helium/dpa ratios in BCC iron and ferritic steels on the formation of bubbles and bubble density. Simulations were performed for values of the He concentrations varying from 1–100 He/dpa. The bubble density scales linearly with increasing damage and increases as the square root of the He/dpa ratio at higher He/dpa ratios.

Materials Testing

LANL Hot-Cell Work

To test the effects of irradiation on the mechanical properties of ferritic/martensitic (F-M) steels, irradiated EP-823 and HT-9 were tested using the shear punch technique to augment the data obtained from tensile tests and prove the validity of data obtained from a much smaller 3-mm diameter disk vs. the larger tensile specimen. Tests were performed at 25ºC and 400ºC. In addition, to investigate the mechanical properties of tantalum (a potential target material) after irradiation, shear-punch tests were performed on tantalum after irradiation in the LANSCE APT and the STIP II campaigns.

Results

Figure 24a shows shear-punch tests measured on EP-823 after the STIP II irradiation. Tensile tests measured on EP-823 under the same conditions are shown in Fig. 24b. From this data, one can see that the specimens irradiated at higher temperatures show more hardening and less ductility. Ductility is related to the difference between the shear yield and shear ultimate stresses. This difference decreases with increasing dose and increasing irradiation temperature. Similar results are observed on the tensile stress/strain curves in Fig. 24b. The reason for observing an increase in ductility when testing the specimens irradiated below 155ºC is that the test temperature (400ºC) is significantly higher than the irradiation temperature. So, during testing, some of the damage formed during irradiation is removed from the specimen. This is not observed for the specimens irradiated at higher temperature because the damage formed during irradiation is more stable at the test temperature and therefore is not annealed out during testing.

Figures 25a and 25b show stress/strain curves measured on Ta-1W after irradiation in the 800-MeV proton beam at LANSCE (APT irradiations) and pure tantalum after irradiation in the 590-MeV proton beam at PSI (STIP II irradiation). Total dose accumulated is over 20 dpa. All stress/strain curves show an increase in shear yield with irradiation while a large work-hardening capacity is retained as noted by the

difference between the shear yield and shear ultimate stresses. Retention of a work-hardening capacity is also indicative of good ductility.

Conclusion

Shear-punch testing on EP-823, HT-9 and tantalum after high energy proton irradiation shows good agreement with tensile results. Shear-punch testing on tantalum suggest a good retention of ductility up to a dose of 25 dpa. Final analysis of results is in progress.

(a)

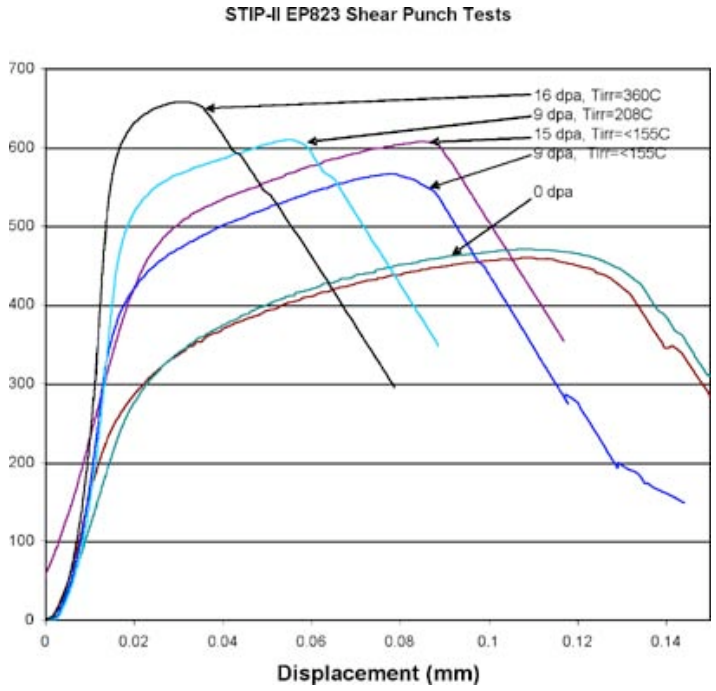

(b)

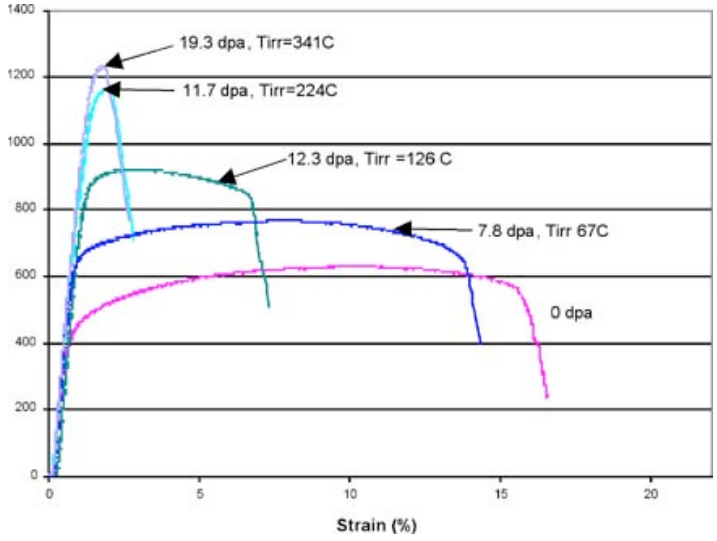

Fig. 24. Stress/strain curves measured on EP-823 at 400C using (A) shear punch testing and (B) tensile testing.

(a)

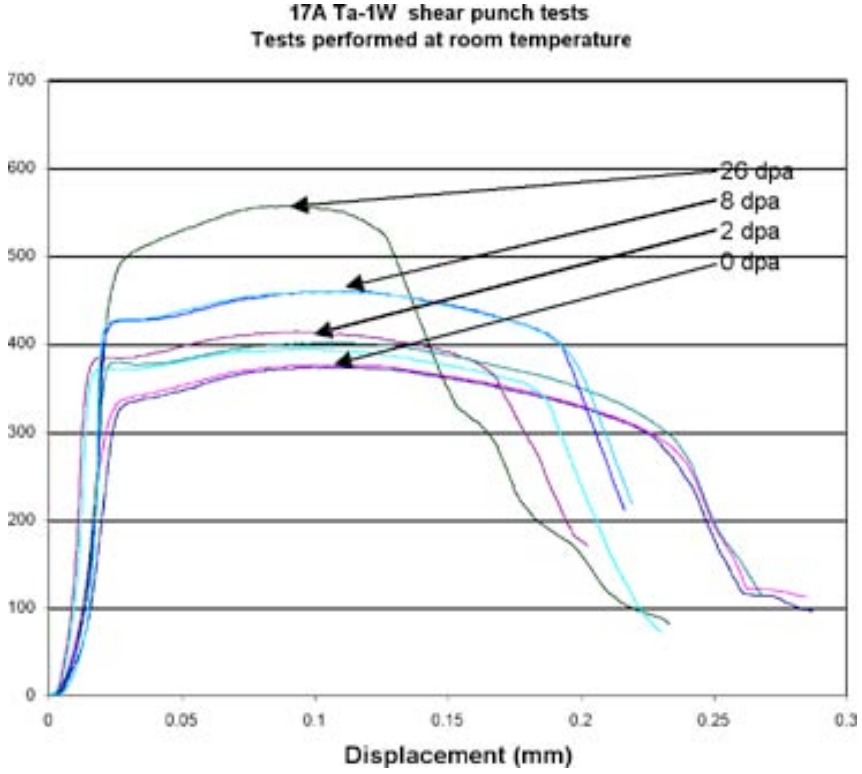

(b)

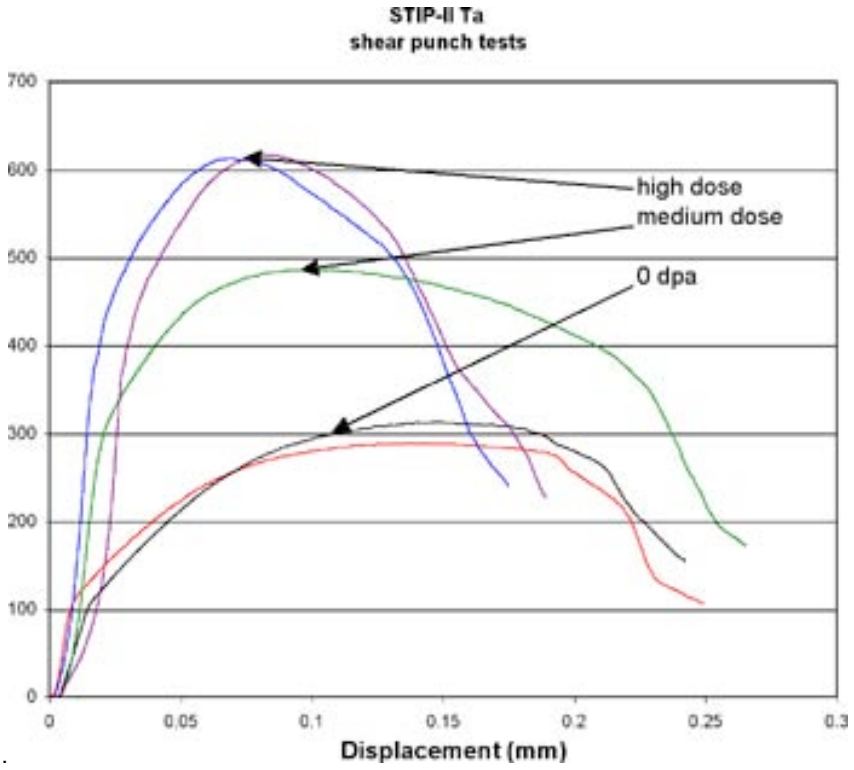

Fig. 25. Stress/strain curves measured on (A) Ta-1W after exposure to the APT irradiations and (B) Ta after exposure to the STIP II irradiations.

PNNL Activities

A large cache of high-dose irradiated ferritic-martensitic (F-M) steel mechanical properties and microscopy specimens reside in storage boxes located in Building 324 on the Hanford Site in Richland, WA. These specimens are of great value to the AFCI materials program. Building 324 is scheduled to be decommissioned and shut down. These specimens will be retrieved this year and shipped to labs for analysis. TEM analysis will be performed at PNNL on FFTF and STIP irradiated materials, tensile and Charpy testing performed on FFTF irradiated materials.

FFTF Ferritic/Martensitic Steel LMR Specimen Retrieval Activities

In the latter part of FY05, the contract for the deconstruction and demolition (D&D) of Building 324 where the FFTF F-M LMR specimens are stored was awarded to a consortium called the Washington Closure Group Hanford (WCH). A letter from DOE-NE was sent to DOE-RL mentioning DOE-NE's interest in the FFTF F-M LMR specimens and our desire to retrieve the specimens before Building 324 is demolished. Shortly after the start of FY06, WCH informed DOE-RL that their preference was not to undertake any specimen retrieval activities. After further discussions with WCH and DOE-RL, WCH has said that as long as there is no significant impact to their D&D schedule, WCH will make an attempt to retrieve the specimens. The goal is to retrieve the specimens by end of this fiscal year.

DOE-NE has requested a cost estimate from WCH for the specimen retrieval work, but WCH is presently too busy to invest significant time into creating a cost estimate. Therefore, PNNL has undertaken the majority of the work required to create a cost estimate. With guidance from WCH personnel, PNNL is formulating three different retrieval plans and cost estimates to go with each of the three plans. There is a "most desirable" retrieval plan and two alternative plans. It was hoped that these plans would be completed by the end of Q2-FY06 (March), but WCH has not had as much time to help as needed. The three retrieval plans are described in the paragraphs that follow.

(1) "Most Desirable" - Use the Existing Overhead Crane - We are still looking at the option of using the existing overhead crane. The trolley motor is broken and will not be fixed, but we are looking at whether the crane hook can be attached to the specimen storage container, and then use the force of the winch to reel the crane over the top of the specimen storage container. This concept is outlined in Fig. 26. WCH personnel have made some progress towards testing the operational capability of the crane. At present, it has been determined that at some time in the past, the crane's electrical power was cut and now needs to be re-connected. WCH personnel are working towards that goal. Once the crane power is restored, testing of the crane capabilities will begin. The main concern is whether the trolley brake can be released and whether the winch motor still functions. If the brake can be released and the winch motor functions, then there is a good chance that the overhead crane can be used. This plan is most desirable because of its simplicity and low cost. However, it is uncertain as to whether the crane will function, and in the mean time, alternate retrieval plans are being developed along side with this plan.

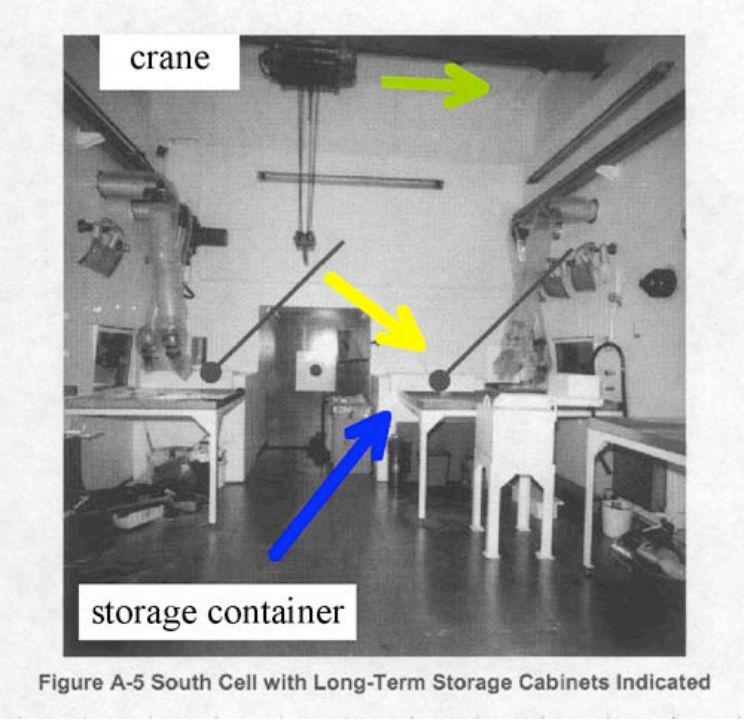

Fig. 26. Picture of SMF hotcell showing that if the crane hook can be attached to the storage container, then the crane can be reeled in over the top of the storage container using the winch motor.

(2) Alternate #1 - Insert Rigging Through the Manipulator Port - The hot cell has several ports for manipulator arms. One of the manipulator arms near the storage container would be removed as shown in Fig. 27, and rigging would be inserted through the port. It is attractive to use a manipulator port because there are already procedures in place for removing and replacing manipulator arms for servicing. This procedure, which is already approved by WCH, will be applied towards inserting the rigging into the hot cell. The rigging would consist of a load-carrying arm that would pivot and extend over the top of the specimen storage container as outlined in Fig. 28. The arm would serve as a track to run a chain fall or cable fall into the hot cell and clip onto the specimen storage container. A winch outside the hot cell would pull the cable/chain and lift the specimen storage container. This method requires procedure development for using the equipment and engineering activities to design and build the equipment. PNNL is performing all of these jobs. The rigging will be built and tested by PNNL, and PNNL will write the procedures in the format used by WCH. This plan has the highest probability for success but would be considerably more expensive.

(3) Alternate #2 - Core Drill the Hot Cell Ceiling - Provided that there is an access space above the hot cell, the concept is simply to core drill through the ceiling directly over the top of the specimen storage container and run a chain down to the specimen storage container. This alternative plan is simple in concept, but is likely to be complicated by the number of procedures and approvals that would be required to perform the core drilling operation. PNNL is working to obtain the hot cell design drawings that are needed to determine the feasibility of this alternative plan.

Fig. 27. Manipulator arm that would be removed to insert rigging into the hotcell to lift the specimen storage container.

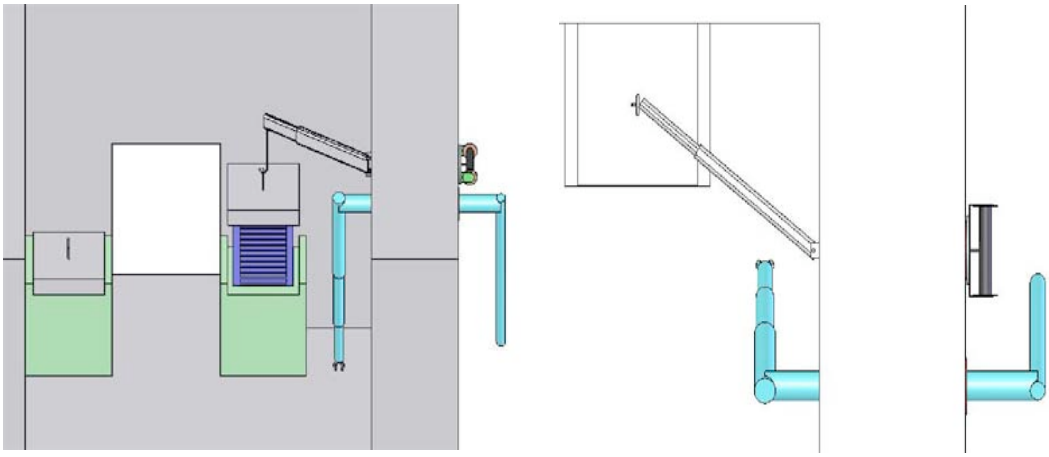

(side view) (top view)

Fig. 28. Drawings showing the orientation of rigging that would be inserted through the hotcell manipulator port to lift the specimen storage container.

Status of FFTF Component Retrieval

The FFTF ACO-3 duct, which is made from the F-M steel HT-9, is still safely in storage in the IEM hot cell on the FFTF site. A sketch of the duct is shown in Fig. 29. The plan was to retrieve the duct in early CY06 using one of the two T-3 shipping casks located on the FFTF site. The use of these casks was contingent upon the refurbishment of the casks that was to funded by DOE-EM who required the use of the casks. The refurbishment of the casks was delayed due to set backs in that DOE-EM program. However, thanks to the efforts of DOE-NE (F. Goldner), issues involved with refurbishment of the T-3 cask have been resolved, and the T-3 cask is currently being refurbished. Refurbishment should be complete in late May or early

June. Refurbishment costs are being paid by DOE-EM. It is expected that the duct will be loaded into the cask and shipped in late June. Prior to loading the duct into the cask, the duct will be swiped to measure smearable contamination levels.

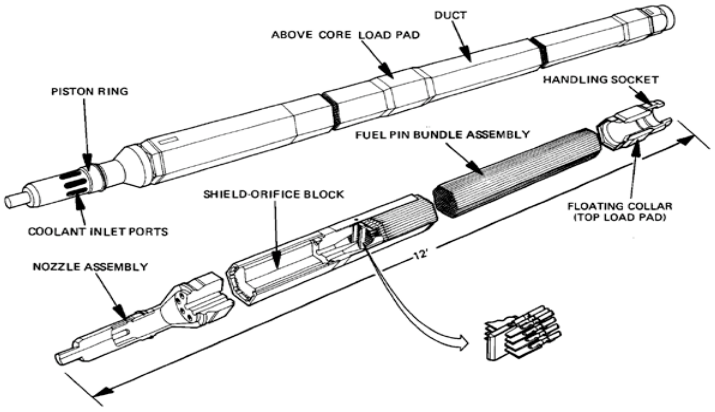

Fig. 29. Sketch of the ACO-3 duct.

AFCI-Gen IV Material Working Group Meeting

In early March, we participated in the 5th AFCI/Gen IV Working Group Meeting and presented the current status of the retrieval of FFTF specimens and the ACO-3 duct. The highlights of that presentation were: (1) DOE-EM and Washington Closure Group (WCH) have agreed to provide assistance with retrieving the specimens on the condition that the retrieval activities have minimal impact on the Building 324 D&D schedule. (2) efforts are underway to determine the most appropriate method to gain access to the specimens. Both the likelihood for success and cost are major considerations. (3) PNNL personnel are working with WCH personnel to gather the information needed for WCH to provide a cost estimate to retrieve the specimens. (4) The ACO-3 duct is safely in storage on the FFTF site and shipment of the duct will take place after the T-3 shipping cask is refurbished in late May. Refurbishment of the cask will be done as part of FFTF closure activities and paid for by DOE-EM.

Radiation Damage Modeling of Structural Materials

Simulation of Radiation Cascades in Fe-Cr System

Summary

We have implemented and debugged a new Fe-Cr EAM model into LAMMPS, a large-scale molecular dynamics simulation code developed by Sandia National Laboratory. This model was tested to ensure its accuracy, and some preliminary simulations of radiation cascades were performed. We now have a powerful capability to run cascade simulations in systems with hundreds of millions of atoms.

Here, we also report Temperature Accelerated Dynamics (TAD) simulations of vacancy clusters in Fe with up to 8 vacancies, using an embedded atom method (EAM) potential to validate the various metastable cluster configurations using first principles simulations.

We are currently conducting large-scale simulations of radiation cascades in Fe-Cr systems, and also incorporating the TAD results in the catalog used in our Kinetic Monte Carlo (KMC) model

Introduction

Radiation effects, both the defect generation and its impact on materials properties, in reactor materials have received much experimental and theoretical attention for a number of years. Ideally, one would like to combine the results of both to obtain a fundamental insight into radiation damage. However, this has proved to be difficult because experimental timescales are usually many orders of magnitude ($>10^{10}$) larger than modeling timescales.

To accurately predict radiation damage-response in a material, it is necessary to simulate longer time-scale processes such as defect mobility, annihilation, and aggregation. Recently, Arthur Voter's team at LANL has developed many novel algorithms to explore long-time dynamics in materials systems [1-3]. In this study, we apply Voter's TAD method to a many-body Fe potential with the goal of understanding vacancy cluster dynamics. To gauge the reliability of the model, we have also begun calculations of defect properties with density functional theory (DFT) [4] to validate the relative energetics of various cluster configurations obtained from TAD simulations using the EAM potential [5].

Temperature Accelerated Dynamics (TAD) Simulations of Vacancy Cluster Diffusion

We use an EAM potential for Fe developed recently by Mendelev *et al*. for our TAD simulations. This EAM model gives very good point defect formation and migration energies in comparison with DFT calculations.

TAD [1-3] is one of a number of accelerated molecular dynamics techniques that allow for the simulation of much longer time scales than conventional MD. The TAD algorithm involves running MD at a high temperature T_{high}, typically much higher than the temperature of interest T_{low}. The times of events seen at this high temperature are extrapolated to times at T_{low}. The extrapolation of event times from T_{high} to T_{low} is exact if harmonic transition state theory holds for the system being studied at both temperatures. It requires knowledge of the energy barrier for the event, which we find using the nudged elastic band method [6,7].

DFT calculations were performed using the VASP [4] code. This code uses pseudo-potentials and reduces the core electrons to an effective potential thereby only explicitly treating the valence electrons.

TAD Simulation Results

We explored long-time diffusion of vacancy clusters with 1, 2, 3, 4, 6, and 8 vacancies (see Fig. 30). In an earlier quarterly report, we summarized the results for the diffusion of a 4-vacancy cluster. Here we present the results for other cluster sizes. The salient result is that clusters with up to 8 vacancies are mobile. This is an important result and will be added to the defect migration process catalog for use in Kinetic Monte Carlo (KMC) simulations.

Fig. 30. Diffusion of vacancy clusters with 1, 2, 3, 4, 6, and 8 vacancies.

TAD simulations reveal many complex and non-intuitive mechanisms causing the translation of vacancy clusters. These mechanisms have different energy barriers to migration. What is the meaning of energy barrier? Imagine a mountain surrounded by valleys. Each vacancy cluster configuration can be imagined to lie in various valleys. To transform to another configuration, we have to climb up to the mountaintop and drop into a neighboring valley. The height of our climb is the energy barrier. The bar chart above plots the upper bounds of the energy barriers to cluster translation process. These barriers are critical input for our KMC simulations. Please note the remarkable agreement between EAM and DFT calculations.

Our calculations show the effectiveness of TAD simulations in probing diffusion processes that occur over a timescale much longer than that probed by conventional molecular dynamics (nanoseconds). This is shown in the table below – e.g., we could probe processes for up to 0.11 seconds of time for the 6-vacancy cluster.

#Vacancies	Boost	t_{max}
01	543	0.24 ms
02	507	0.15 ms
03	60	9.6 μs
04	268	68.7 μs
06	55,000	0.11 sec
08	36,000	66 ms

The energy barriers for long-term diffusion of vacancy clusters obtained from TAD simulations allow us to ask the critical question: At a given temperature and energy barrier, how long does it take for cluster diffusion to be activated? Assuming a reasonable value of 5e+12/second for the Arrhenius prefactor, we can evaluate the Boltzmann factor using $\tau = 1/[\nu_0 * \exp(-E_b/kT)]$, where k, E_b and T are respectively the Boltzmann constant, energy barrier, and temperature. From this we can plot the time to activate the motion of clusters as a function of temperature as shown in Fig. 31.

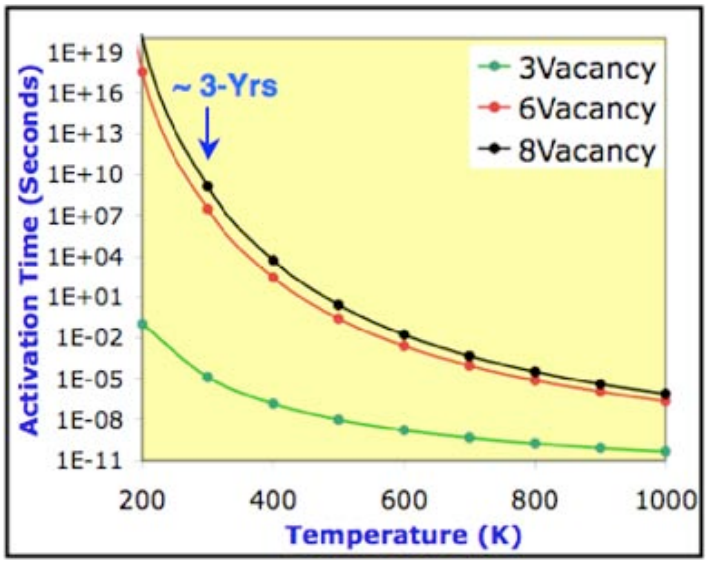

Fig. 31. This plot shows that at room temperature (300K), a 6-vacancy cluster will take ~3 years to diffuse.

KMC Simulations of Helium in Iron and Ferritic Steels

Introduction

The present work is aimed at quantifying the effects of irradiation damage accumulation in the presence of He in ways that were not possible in earlier studies. This is accomplished through systematic and coordinated computational modeling and experiments. The modeling approach employs both molecular dynamics (MD) and Kinetic Monte Carlo (KMC) simulations to study the dynamic evolution of He and defect clusters in BCC iron over relevant time scales. Figure 32 shows connections between various levels of modeling and simulation as applied to radiation damage in ferritic steels.

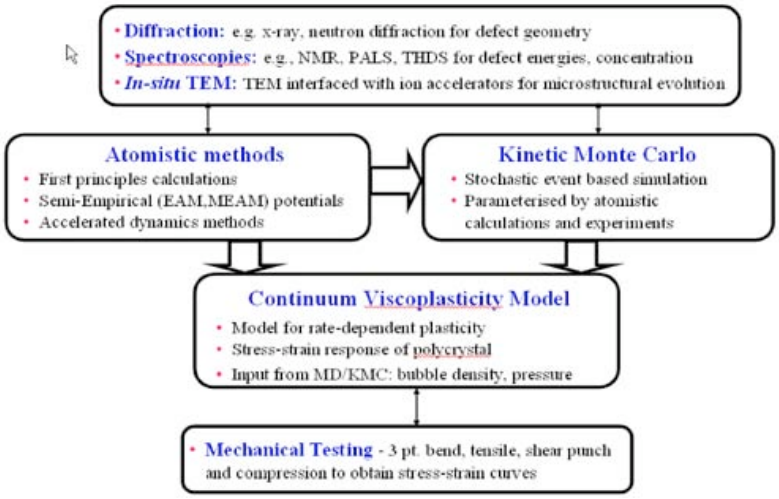

Fig. 32. A schematic of the relationship between various modeling and simulation techniques as relevant to predicting the effects of helium on irradiation damage in single-crystal iron.

The KMC model consists of helium interstitials on the octahedral sublattice and vacancies on the BCC iron lattice. Figure 33 shows the mechanisms by which the point defects migrate. The migration of the free (not clustered) helium and vacancies are illustrated in Figures 33(a) and 33(b) respectively. The rates of migration of the point defect entities are calculated as:

$$r^i_{migration} = \nu^i_{migration} \exp\left(-\frac{E^i_{migration}}{k_B T}\right), \quad (1)$$

where the superscript *i* refers to the helium and the vacancy point defect entities. The rate of migration of the point defect entity is $r^i_{migration}$, the attempt frequency is $\nu^i_{migration}$, the migration barrier is $E^i_{migration}$, while k_B and T are the Boltzmann constant and the temperature respectively. Two point-defect entities are considered to be in a cluster when the distance between them is less than a_0, which is the lattice constant of BCC iron. Dissociation of the helium and the vacancy from the cluster is described in Figs. 33(c) and 33(d) respectively. The rate of dissociation of a point defect entity (*i* = helium or vacancy) from a cluster into the bulk lattice is considered to be thermally activated and is calculated as:

$$r^i_{dissociation} = \nu^i_{dissociation} \exp\left(-\frac{E^i_{dissociation}}{k_B T}\right) \quad (2)$$

where $r^i_{dissociation}$ is the rate or dissociation, $\nu^i_{dissocation}$ is the attempt frequencies, $E^i_{dissociation}$ is the energy of dissociation. The dissociation energy $E^i_{dissociation}$ of a point defect from a cluster is taken to be the sum of the energy to bind a point defect entity to the cluster and $E^i_{migration}$. Morishita et al. [8] have calculated the migration energies of helium and vacancies as well as the binding energies of some helium-vacancy clusters. We employ these migration barriers to calculate the rate migration of the point defect entities. The attempt frequencies for the migration are taken to be of the order of the Debye frequency of iron (for vacancy migration) and that of helium (for helium migration). These parameters are used to calculate the rates of all the possible events [Eqns. (1) and (2)] in the system and build the event catalog for the KMC simulation.

The event catalog is generated by calculating the rates of migration or dissociation of the point defect entities using Eqns. (1) and (2). The KMC event catalog consists of the migration, clustering and dissociation of two point defect entities, helium and vacancies. The transition probability of each event is proportional to the rate of event occurrence, calculated by the Eqns. (1) and (2). We follow the well-established KMC simulation algorithm [9.10] which is a stochastic, atomic-scale method to simulate the time-evolution of defects and nano/microstructural evolution that focuses on individual defects and not on atomic vibrations.

At each KMC step, the system is monitored to identify a clustering event. When two point-defect entities (helium-helium, vacancy-vacancy, helium-vacancy) are in a cluster, the simulation creates a mapping between the entities and the cluster such that for each cluster there are at least two entities associated with the cluster. The event catalog is updated with the new rates of event occurrence and the transition

probabilities for the next KMC event are calculated. This quarter, we report on the time evolution of the concentration of free vacancies and helium, helium (He_n) clusters, helium-vacancy (He_nV_m) clusters, where n and m indicate the respective number of He or V in the cluster.

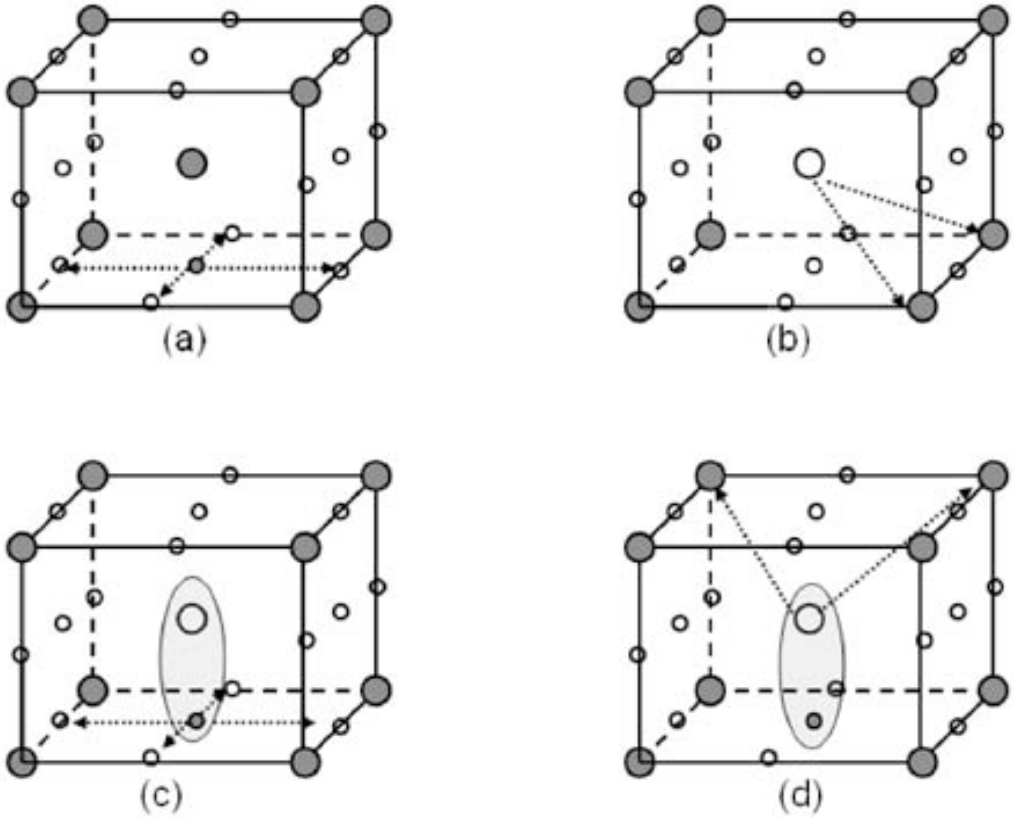

Fig. 33. Basic mechanisms of helium and vacancy activity in single-crystal BCC iron. Large filled circles represent iron, large open circles represent vacancies, small filled circles represent helium atoms and small open circles represent the octahedral BCC sites. (a) Helium migration on the octahedral sublattice; (b) Vacancy migration in BCC iron; (c) Dissociation of helium from an embryonic bubble; and (d) dissociation of vacancy from an embryonic bubble.

Defect Evolution (Q1-Report Summary)

We employ the above KMC model and algorithm to study helium and vacancy diffusion and clustering over small and large time scales. The interstitials diffuse by hopping to adjacent octahedral sites on the lattice while the vacancies diffuse by the vacancy mechanism on the substitutional BCC iron lattice. It is possible to introduce He atoms and vacancy populations throughout the KMC simulation at rates appropriate to the irradiation environment.

In the first quarter report, we investigated the defect evolution as a function of time. Free helium concentration, free vacancy concentration and cluster concentrations were plotted. Both free helium and free vacancy concentrations decrease with increasing time. The free helium concentration decreases far more rapidly than the free vacancy concentration. After the free helium concentration decreases to a negligible amount, the free vacancy concentration decreases rapidly. The

concentration of helium-helium clusters increases in the initial evolution phase, but decreases to a negligible amount at longer times. The concentration of helium-vacancy (He-V) clusters increased throughout the simulation and reached a constant value once all the free helium and the vacancies were incorporated in bubbles.

We also reported on the effect of temperature on vacancy evolution and on the evolution of clusters. Initially, the decrease in free vacancy concentration corresponds to the migration of the helium atoms and their clustering with vacancies. At longer times, all the helium is incorporated in embryonic clusters and the vacancies migrate leading to a decrease in their concentration. The He-He clusters increase in time at shorter times and decrease to a negligible value at longer times. The He-V clusters increase with increasing time until they reach a constant value for the given initial conditions. Thus helium-vacancy clusters persist over longer times while helium-helium clusters do not.

Helium Bubble Density

We now employ the KMC model to simulate the effect of damage and helium/dpa ratios on the formation of bubbles and bubble density. Simulations are performed for values of the He concentrations varying from 1–100 He/dpa. These correspond to proton energies on the order of hundreds of MeV, where high levels of gas atoms are generated in constituents of typical structural alloys, with helium typically 80–160 appm/dpa, and hydrogen (i.e., protium) at levels approximately an order of magnitude higher.

Figure 34 shows the concentration of bubbles as a function of He/dpa ratio after damage equal to 1 dpa is introduced. The bubble concentration is plotted as a fraction of the damage introduced in the system. The simulation temperature is $0.3T_m$. The bubble density increases linearly with increasing He/dpa ratio until it begins to saturate at high He/dpa rations. At higher He/dpa ratios, the bubble density can be described by a power law expression,

$$\rho_B = K\left(c_{He}\right)^m, \tag{3}$$

where ρ_B is the bubble density, c_{He} is the helium concentration in terms of the He/dpa ratio and K and m are constants determined by the kinetic Monte Carlo simulations. We find that the exponent m, at higher He/dpa ratios is ~0.5. Thus the bubble density increases as the square root of the He/dpa ratio at higher He/dpa ratios.

Figure 35 is a linear plot of the concentration of bubbles as a function of He/dpa ratio. Three different damage levels are considered 0.1, 1 and 10 dpa. The bubble concentration is plotted as a fraction of the damage introduced in the system. The simulation temperature is $0.3T_m$. We find that changing the damage level from 0.1 to 1 to 10 dpa has no effect on the fractional bubble density. Thus, the bubble density varies linearly with damage in this region. At higher dpa ratios, more damage is produced and more helium is produced for that amount of damage. Thus the bubble density scales linearly with increasing damage.

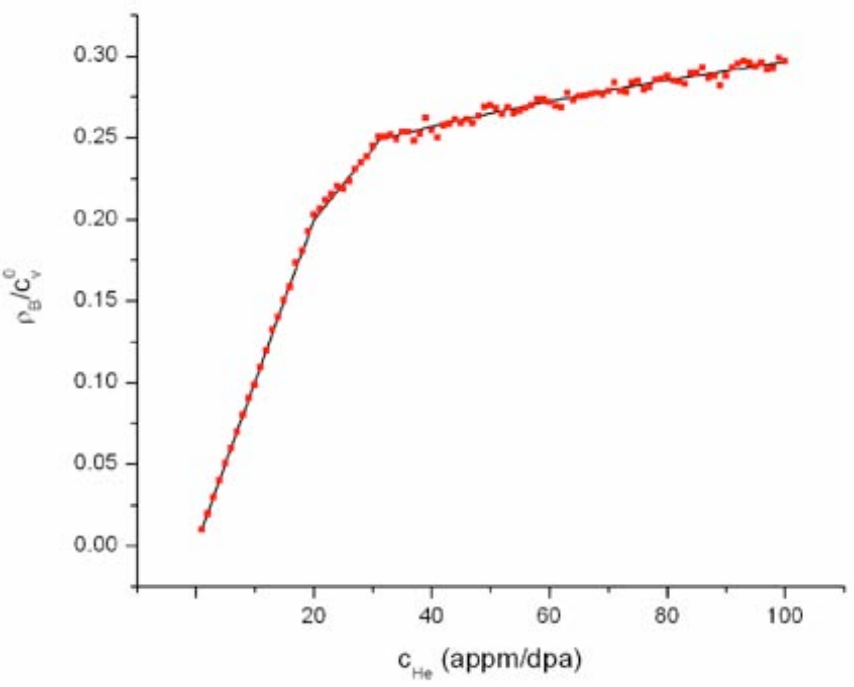

Fig. 34. A linear plot of the concentration of bubbles as a function of He/dpa ratio after damage equal to 1 dpa is introduced. The bubble concentration is plotted as a fraction of the damage introduced in the system. The simulation temperature is $0.3T_m$.

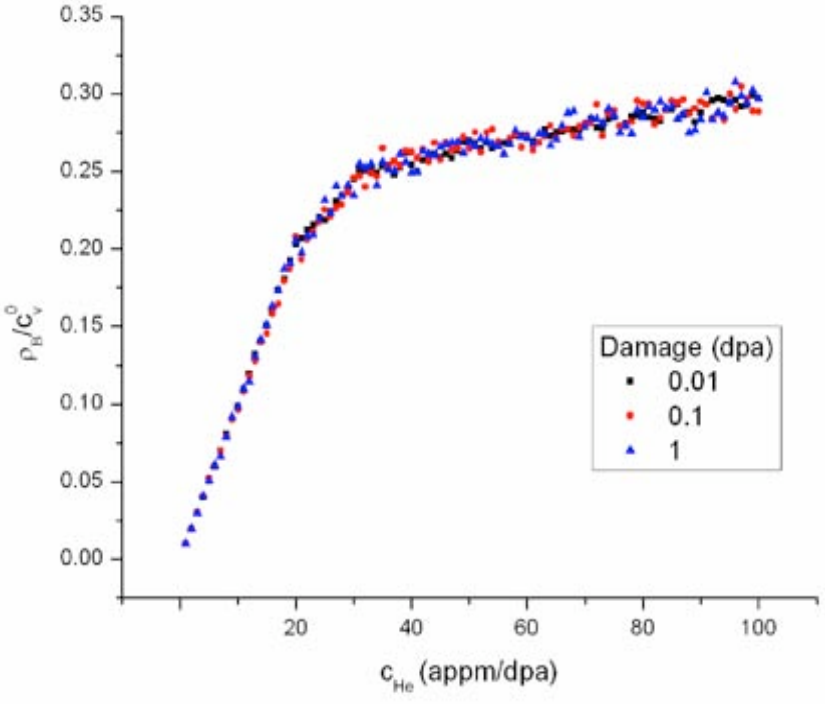

Fig. 35. A linear plot of the concentration of bubbles as a function of He/dpa ratio. Three different damage levels are considered 0.1, 1 and 10 dpa. The bubble concentration is plotted as a fraction of the damage introduced in the system. The simulation temperature is $0.3T_m$.

Simulations are on-going to study the effect of more damage conditions on the volution of bubbles using the KMC model. We are also conducting simulations that will clarify the effect of temperature on the evolution of bubble density and bubble size distribution.

KMC simulations of Ferritic Steels

We are also modifying the KMC simulations to study damage evolution in ferritic steels. The KMC model has been modified to include the presence of chromium atoms and migration mechanisms of the chromium atom. Chromium is assumed to migrate via substitutional mechanism. The model consists of the following entities in BCC steel: interstitial and substitutional helium and hydrogen atoms, interstitial iron atoms, substitutional chromium atoms, vacancies, vacancy-clusters, and sinks for the trapping of point defects (dislocations and grain boundaries). Input to the simulations includes the migration energies of the point defects (interstitial iron, vacancy, interstitial and substitutional helium and hydrogen), formation energies of the He_nV_m clusters, dissociation energies of the point defects from the He_nV_m clusters and initial concentrations and configurations of point defects and defect ratios. These quantities are obtained from the molecular dynamics (MD) simulations using MEAM potentials. The defect ratios and configurations are obtained from the post-cascade data of large MD runs.

At present, we have conducted some benchmark simulations of the iron-chromium system in equilibrium conditions allowing for the migration and clustering of chromium substitutional atoms via the vacancy mechanism. Two compositions 5% and 10% atomic fraction of chromium were considered in the simulations. The final simulations will be conducted over the range of 1-12% chromium in iron.

Summary

We have employed the KMC simulations to investigate the time evolution of the point defect configuration leading to defect clustering and bubble formation. The concentration and composition of embryonic defect clusters as a function of time and operating temperatures is determined. The low migration energy of the helium interstitials implies that the helium diffusion is faster than the vacancy diffusion. This leads to the initial formation of He_nV_m and He_n clusters. Helium-helium clusters dissolve while helium-vacancy clusters survive over longer times. These cluster concentrations evolve with time as the vacancy migration becomes more active at a longer time scale.

We have employed the KMC model to simulate the effect of damage and helium/dpa ratios on the formation of bubbles and bubble density. Simulations are performed for values of the He concentrations varying from 1–100 He/dpa. The bubble density scales linearly with increasing damage and increases as the square root of the He/dpa ratio at higher He/dpa ratios.

Coolant Technology

Scope

The major objective of lead-bismuth eutectic (LBE) research activities is to develop a fundamental understanding of LBE performance parameters and measurement techniques when used as a nuclear coolant, supporting the development of advanced reactors and transmuter concepts. Specific activities include analysis and modeling of oxide growth on specimens tested in the DELTA loop, system-corrosion modeling to include interface (oxides) dynamics, active corrosion-probe development based on commercial prototypes, and continued oxygen-sensor development and calibration.

Highlights

- We completed a significant reprogramming of the FY06 R&D tasks following the budget reduction due to GNEP realignment, revising all work packages.
- Welding of the Lead Correlation Stand (LCS) was completed, and the loop leak tested; installation of the main portions of the support structure, enclosure, and platform were also completed.
- We successfully conducted proton irradiations at the Ion Beam Materials Laboratory (IBML) that will be used to study irradiation effects on microstructure and corrosion; irradiation cells were assembled and tested.
- We prepared and submitted an LDRD proposal for establishing a materials-irradiation beamline at IBML to study radiation damages of new materials and processing.
- Preparation of software and programming was started for analyzing the available corrosion test data from around the world, using a model-based approach to extract corrosion rates that were not measured directly.
- We continued to perform lattice Boltzmann simulation of 2-D heat transfer in natural convection flow into the turbulence regime, preparing for heat and mass transfer studies of oxygen control in natural convection-driven LBE systems.
- A PbO canister was fabricated and the bypass welded in preparation for installing the mass exchanger into DELTA for oxygen-control testing.

Integration

We reprogrammed all AFCI Transmutation work packages in Coolant Technology and Materials Development to reflect DOE-HQ's reduced AFCI budget, proceeded to reassign personnel, and initiated planning for outyear R&D and funding for this area of work. We have begun supporting GNEP small reactor technology development planning.

We also coordinated materials delivery and characterization with Penn State University NERI collaborator for detailed study of oxide microstructure in LBE-tested steels.

DELTA Loop Operations

We fabricated the PbO canister and welded a bypass in preparation for installing the mass exchanger into DELTA for oxygen-control testing. We repaired and cleaned the gas injection venturi, the level sensors and the gas supply line that lost the LBE freeze plug due to high temperature during the last DELTA test campaign, and started to enhance the cooling by replacing cooling water lines with larger ones.

We began preparing the materials (shown in Table 5) for the upcoming DELTA test. The specimens will be partially coated with alumina (Al_2O_3) so we can make direct measurement of corrosion rather than only measuring oxide thickness.

As before, we continued to characterize DELTA-tested specimens.

Table 5. Partial List of Materials and Conditions to be Included in the next DELTA Test.

Material	Condition	Material	Condition
HT-9	As received (Timken)	SMAT 316L	Surface deformed 316L
HT-9	HTP nano crystal	SMAT 420SS	Surface manipulated 420SS
HT-9	New heat	420 SS	As received
T91	As received (Timken)	MA956	As received
T91	New heat	Ma956 Welding	Welding
T91	HTP nano crystal	PM2000	As received
14Cr SC*	Spherical shaped SC*	Aluchrome Y Wire	Welding rod
		Crofer 22 APU	As received

*SC = single crystal

Oxide Layer Analysis

Oxide Dispersion Strengthened (ODS) Steels

X-ray Photo Spectroscopy (XPS) analysis was completed of the Al-alloyed ODS steels PM2000 and MA956 after a 600-hr exposure to the 535ºC hot LBE. Figure 36 shows the sputter depth profile of PM2000, for which a clear picture can be drawn. PM2000 shows a Y enrichment in the first 500Å and an Al enrichment in the first 1000Å. The O content has a similar trend to that of the Al content. The Cr content in the near surface area is lower than in the bulk. The thickness of this layer is about 2000Å. The measurements for the Al are more difficult to perform and less accurate because of peak interference in the spectrum. However, it can be seen that the Al and Y have a strong effect on the materials and its oxidation behavior. The data for MA956 are subject to further investigation.

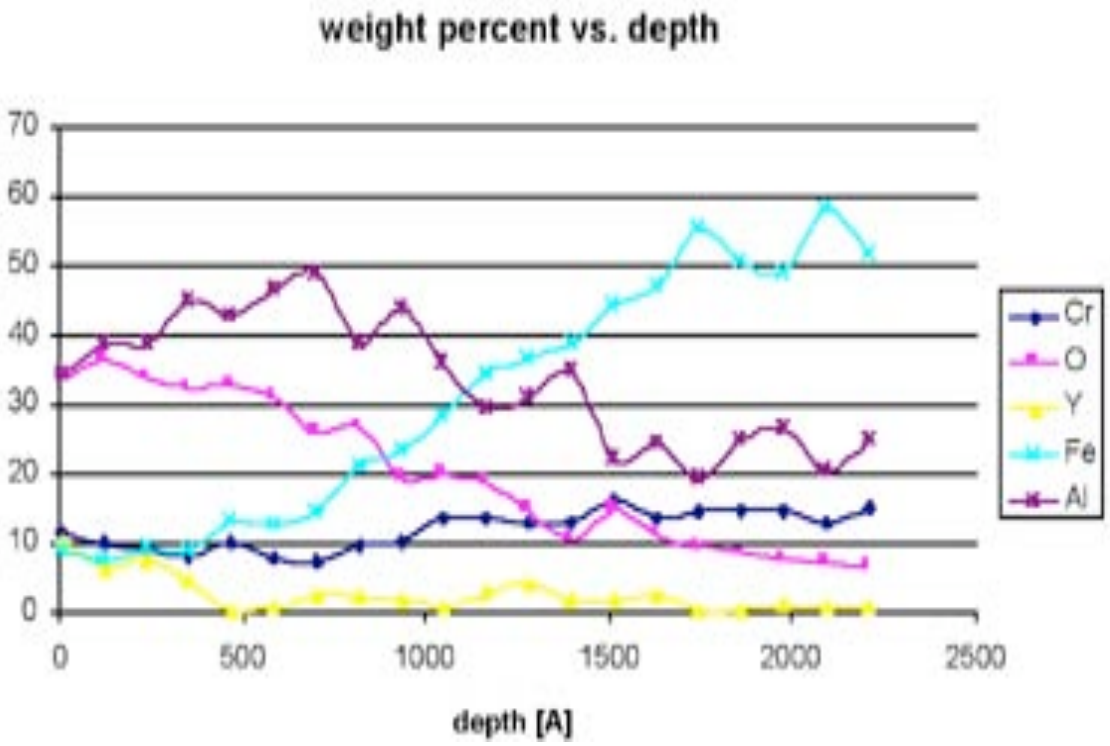

Fig. 36. Presents the XPS sputter depth profile from the materials PM2000. The data are shown here in weight percent vs. depth in the material.

Laser Peening

The SEM/EDX/WDX nano indentation measurements were finished on the surface-treated specimens tested in DELTA at 535ºC for 600 hrs, including the laser-peened, shot-peened and un-peened HT-9, 316L, T91, and EP823. Figure 37 shows the results for the peened and un-peened HT-9. The results of HT-9 are representative of the behaviors of the tested ferritic/martensitic materials. There are no significant differences between laser-peened and un-peened. This seems to result from the fact that laser peening induces only a stress state and no real structural change. The nano indentation and the micro-hardness measurements show that after exposing the samples in LBE, the initial (before exposing to LBE) hardness difference between peened and un-peened disappeared. Therefore, it seems that exposure at 535ºC for 600 hrs anneals the samples enough to eliminate the influence of laser peening on the samples. The nano indentation results show that the oxide layer itself is “weaker” (lower E-modulus and hardness than the pure FeCr oxide). This may be caused by the high porosity in the layer itself. The results agree with the literature where it is reported that a thicker oxide layer causes “weaker” mechanical properties due to higher porosity.

Stainless Steel 316L on the other hand seems to show a slight improvement due to laser peening. Micro-hardness measurements show that the compression stress is still in the materials after the experiment. On the laser peening side, less grain boundary oxidation was found. Therefore, it can be said that the compression stress stays in 316L at these test conditions and improves the oxidation behavior.

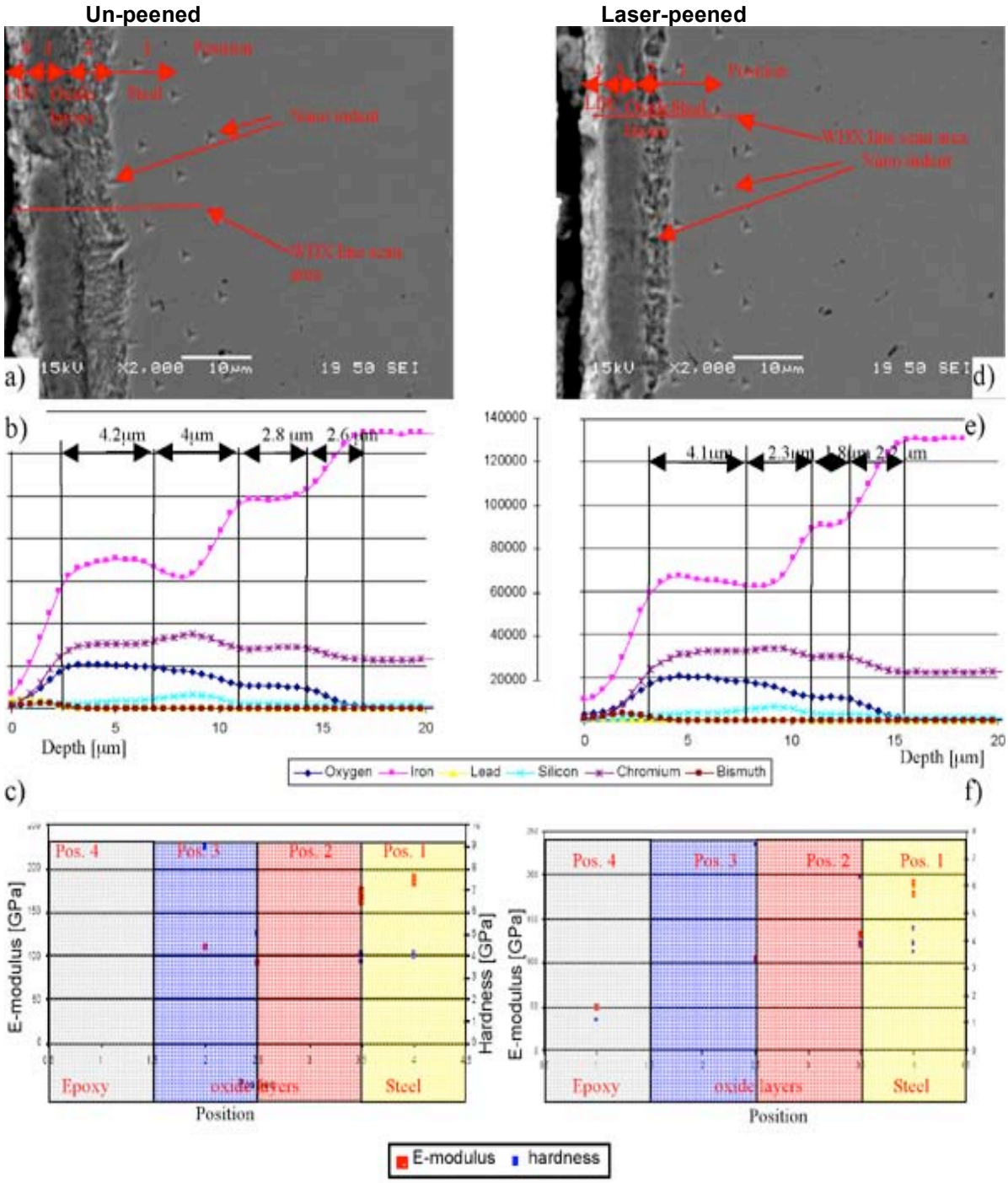

Fig. 37. Shown in (a) and (b) are the SEM image and the corresponding WDX line-scan of the as received (un-peened) HT-9 material after 600-hr exposure to LBE. Shown in (d) and (e) are the SEM image and the corresponding WDX line-scan of the laser-peened HT-9 material after 600-hr exposure to LBE. At both SEM images, the nano indents are visible. The areas where the nano indents were made [results shown in (c) and (f)] are marked in the SEM images as well as the area where the line scans were made. No significant difference between the laser peened and the un-peened material can be observed.

Lead Correlation Stand (LCS)

Welding of the Lead Correlation Stand (LCS) was completed, and the loop leak was tested to 10^{-4} Torr vacuum pressure.

We modified the design and selection of materials of the expansion tank, re-fabricated the top plates, and welded the ports without the cracks found from the previous attempt.

The main portions of the support structure, enclosure, and working platform were installed.

The new welding technique developed for ODS steels was evaluated by the Technology Transfer Office to have research and industrial needs. It will be submitted for patent protection.

Corrosion Control

We have compiled the results of heavy liquid-metal coolant technology and materials development that has been conducted through numerous corrosion tests on a wide variety of steels and reported in the literature as of Fall, 2005. The results may be summarized as follows:

- There are over 22 ferritic/martensitic steels (including a number of ODS steels), and 6 austenitic steels tested in stagnant and/or flowing LBE and/or Pb. The test duration ranges from a few hundred hours to up to 7200 hrs (the longer durations are mostly for stagnant testing).
- In stagnant LBE (in crucibles, with or without oxygen control), more than 165 results for F/M steels and over 102 for austenitic steels are available.
- In flowing LBE (in loops, usually with oxygen control), more than 70 results for F/M steels and over 42 for austenitic steels are reported.
- In Pb, 12 results are reported for stagnant testing, while 20 are reported for dynamic (flowing) testing.
- Most groups only analyzed oxide growth based on simple oxidation power laws, and were not able to extract liquid-metal corrosion rates. This is complicated by the difficulty in measuring weight changes due to residual LBE/Pb on specimens.
- Our modeling and testing show the mechanisms and kinetics of oxidation and corrosion in liquid metals, and will be applied to the reported test results from other groups.

We devised strategies to use our models to analyze the reported test results and extract long-term corrosion rates, and started to select software and programming. Early analysis showed that our approach yielded much improved interpretation of the results, including the often neglected and usually not-measured corrosion rates.

We studied the comparisons between asymptotic thickness of the oxide layer in liquid lead and LBE. One example is shown in Fig. 38. It appears that for the same oxygen concentration (but slightly different activities), oxide layers are thicker in LBE.

We continued to model heat transfer in natural convection-driven flow in cavities, and dependence on aspect ratio in an effort to understand oxygen distribution in stagnant tests. The simulations produce some qualitative and quantitative understanding of transition to fully turbulence flow.

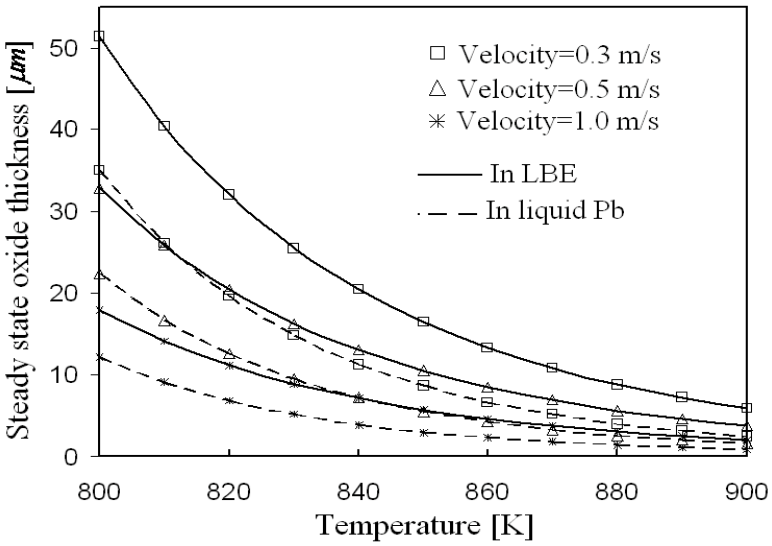

Fig. 38. Comparison of asymptotic oxide layer thickness as a function of temperature for different flow velocities in LBE and Pb. The oxygen concentration is 0.05ppm.

Below are velocity fields and temperature contours in aspect ratio 1 box (from top left to bottom right, Ra=1e1, 1e2, 1e3 (laminar), 1e4, 1e5, 1e6, 1e7, 1e8 (highly turbulent):

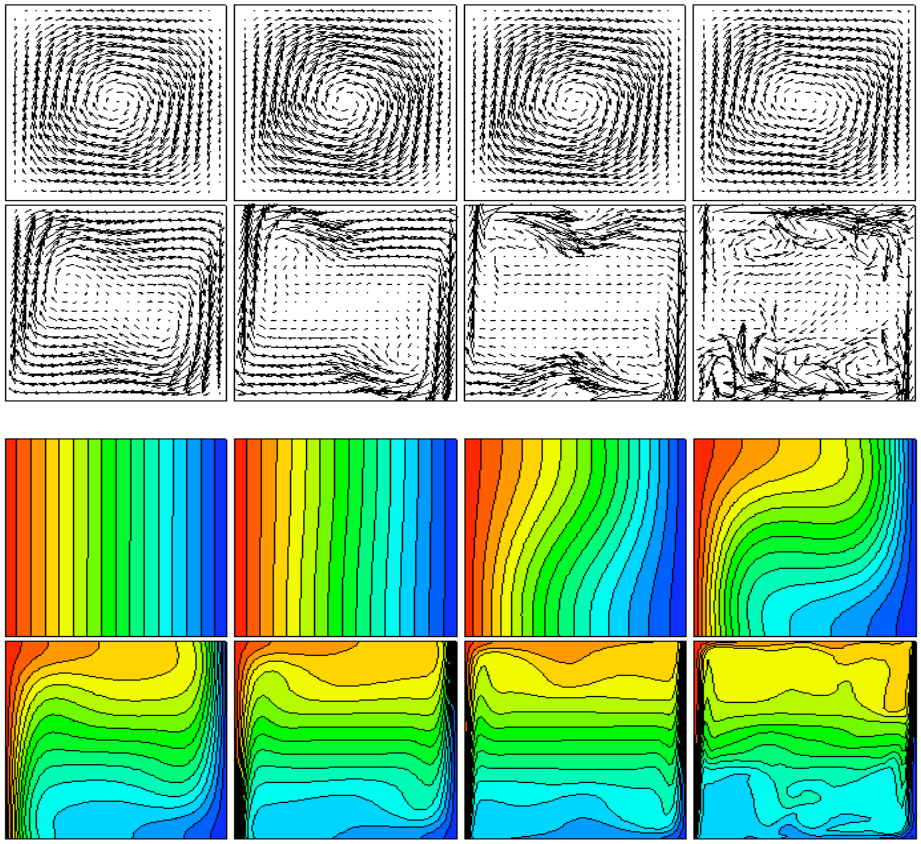

Irradiation Effects on Corrosion

The pure Ta Ta+O_2, Ta+W, Ta+W+O_2 samples were prepared and irradiated in the IBML for 10 hrs. The experimental setup in the beamline can be seen in Fig. 39(a). The cooling sample holder could hold the temperature constant at 29ºC during the entire experiment. The dose-depth profile can be seen in Fig. 39(d). This is a successful test of materials irradiation using IBML accelerator.

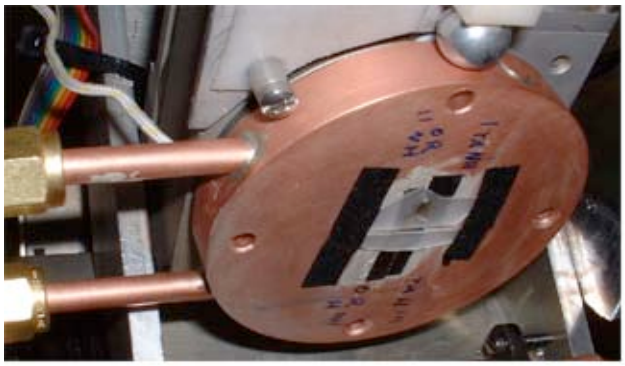

(a)

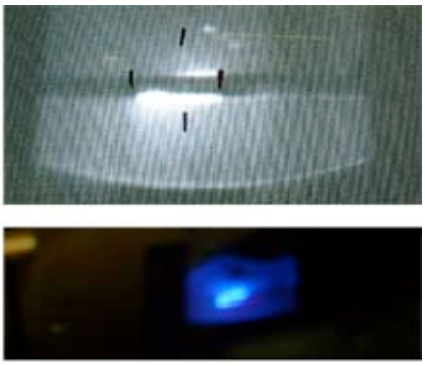

(b) top, (c) bottom

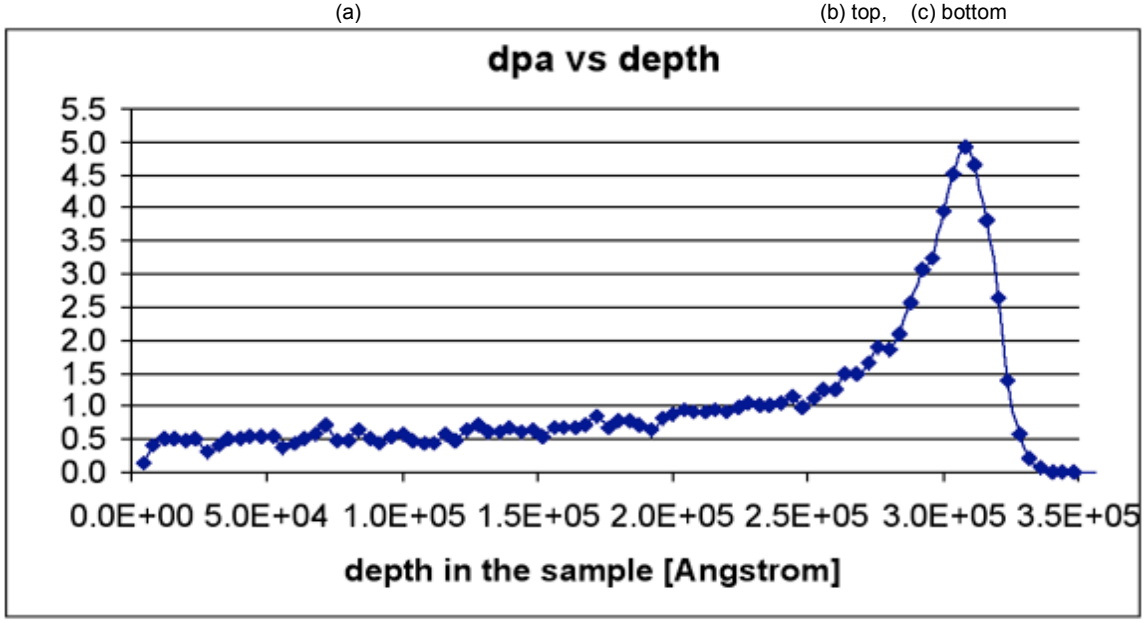

(d)

Fig. 39. (a) Digital image of the sample holder with the Ta samples glued on together with the scintillators; (b) The 3-MeV proton beam is the bright spot in the scintillator gap. The gap is 2mm wide. Therefore, the irradiation area is 8mm^2; (c) Live image of the glowing scintillator; (d) The dose vs. depth profile is given.

We procured and/or fabricated all main components of the irradiation test cells. A dummy sample with a ceramic gasket was assembled and vacuum tested successfully. This electrically insulates the specimen and allows the use of electric impedance measurement of corrosion.

According to our study, using the γ-ray to measure the oxides based on proton activation may provide another *in-situ* measurement of oxidation and corrosion. This will be tested as well.

Corrosion Resistant Alloys

To investigate the structure and porosity of the oxide layer, a fracture device was built. This device will allow breaking samples in liquid nitrogen so that the F/M specimens will break in a brittle fashion, preserving the inter-granular structural details. We will be able to visualize the fracture surface of the oxide layer and therefore the structure of the oxide as well. Currently HT-9, 316L, T91 and EP823 are oxidized in an air furnace at 535ºC for 200 hrs to grow a thick oxide layer. These samples will be tested in the breaking device so the oxide layer structure can be analyzed. We began to prepare DELTA-tested Mo- and W-coated specimens for analysis.

Transmuter Design Activities

Transmuter Design

Scope

The effectiveness of fast spectrum systems for actinide transmutation has been well documented. On the other hand, fast reactor systems are expected to be more costly than conventional LWRs; thus, multi-tier fuel-cycle strategies strive to limit the number of fast systems by maximizing the destruction rate. In FY02-03, low conversion-ratio designs were developed for the SFR concept using metal fuel. Results indicate that the favorable passive safety behavior can be retained, even to the limit of nonuranium fuel forms. In this work, a similar approach will be employed to develop SFR-system point designs employing oxide and nitride fuel. The reactor performance will be compared to the metal-fueled SFR, and any changes in transmutation performance and/or system design will be explored in detail. The eventual goal is to perform a consistent safety comparison of low-conversion SFR burners with the three fuel types (metal, oxide and nitride); however, only the designs and cursory evaluation of reactivity coefficients will be completed in FY06 at the specified funding level.

Highlights

- A document entitled "Low Conversion Ratio Fuel Studies", (ANL-AFCI-163) was submitted to DOE, fulfilling an AFCI milestone for the Transmutation Design Work Package.

Technical Summary

A neutronics study was completed for a nitride-based fuel form employed in a compact fast-burner reactor that achieves a low conversion ratio. In this work, a previous low conversion ratio design developed in 2003 was used as the starting point for the nitride-fueled reactor. The major design option used in the earlier work to achieve a low conversion ratio was the reduction of fissile breeding by the removal of fertile material from the fast reactor system. To reduce the fertile content, the fuel-pin diameter is decreased while the number of driver assemblies, the assembly size, and assembly pitch are held constant. This causes a reduction in the fuel volume fraction. To maintain criticality, the fissile loading must be conserved and thus reductions in the fertile content must be made. For the nitride fuel studied in this

work, the differences in the density and assumed irradiation swelling behavior lead to changes in the conversion ratio. The same modifications of the pin geometry are again utilized to target a 0.25 conversion ratio for a system fueled with nitride fuel.

Three different nitride fuel forms were considered. The first used natural nitrogen while the second used enriched nitrogen. The final nitride fuel form introduces 1 wt% of hydrogen contaminant into the natural nitrogen-fueled core. This rather large amount of contaminant is posed as a bounding limit rather than a real amount. Table 6 gives a breakdown of the important changes seen between the three reactor models. All of the results presented in Table 6 are based upon the same configuration of a recycle model with the same assembly geometry. The only difference in geometrical configuration is the pin diameter given in Table 6, which was altered such that the nitride-fueled core utilizing natural nitrogen would yield a conversion ratio identical to the metal-fueled core. These changes in pin size are needed due to the change in the fuel density and the assumed change in fuel swelling when switching from metal fuel to nitride fuel.

As can be seen in Table 6, the change in fuel pin size affects the fuel-volume fraction, which leads to a change in the total fuel loading. For the hydrogen-contaminated fuel, the nitride fuel-volume fraction was artificially decreased to allow for the 1 wt% of hydrogen, thus the fuel loading changes when compared with the other nitride-fueled cores. Excluding the hydrogen-contaminated core, the basic performance data only indicate a minor change in the TRU destruction rate and fuel loading when switching from metal to a nitride fuel form. The reactivity coefficients also undergo some changes but generally are very similar. The void worth is clearly better for the natural nitride-based fuel, but the higher production of ^{14}C is not justifiable from the changes in core performance or reactivity coefficients.

Table 6. Compact Core Reactor Performance Data and BOC Reactivity Coefficients

	Metal	Natural Nitrogen Nitride	Enriched Nitrogen Nitride	H Cont. Nitrogen
Fuel Pin Diameter (cm)	0.631	0.5354	0.5354	0.5354
Calculated TRU Conversion Ratio	0.23	0.23	0.25	0.18
Beginning of Cycle				
U Loading (kg)	2133	2108	2178	1501
TRU Loading (kg)	2689	2818	2730	3382
Heavy Metal Loading (kg)	4822	4926	4908	4883
Total HM Feed (kg/yr)	1500	1530	1525	1516
Net TRU consumption rate (kg/yr)	200	201	196	217
Peak Fast Fluence (10^{23} n/cm^2)	4.3	3.5	3.6	1.1
Burnup Reactivity Loss (%Δk)	3.5	3.2	3.3	2.8
Beta	2.62E-03	2.63E-03	2.62E-03	2.75E-03
Prompt Neutron Lifetime	4.11E-07	4.15E-07	4.24E-07	7.69E-07
Sodium Density Worth (cents/K)	0.16	0.14	0.15	0.037
Sodium Void Worth ($)	6.73	5.43	6.02	2.19
Radial Expansion Worth (cents/K)	-0.37	-0.34	-0.36	-0.13
Axial Expansion Coefficient				
Fuel & Clad (cents/K)	-0.23	-0.20	-0.21	-0.09
Fuel (cents/K)	-0.33	-0.13	-0.14	-0.06
Control Rod Driveline Expansion ($/cm)	-0.65	-0.570	-0.595	-0.261
Doppler (cents/K)	-0.041	-0.014	-0.058	-0.350
Burnup Reactivity Loss ($)	13.58	12.30	12.58	10.11

The introduction of the large hydrogen contaminant appears to generally be beneficial. However, this is a little deceiving since this reactor discharges more higher actinides, such as Cm, compared to the other three. Similar to the production of ^{14}C, an increased production of higher actinides is also undesirable. Given the radical changes in the reactivity coefficients for this core, clearly a safety analysis would have to be performed to assess the impact.

Overall, the metal-fueled core and the core loaded with enriched nitride-based fuel have very similar core performance. The reactivity coefficients are also very similar and it is not unreasonable to assume that the safety performance will be similar. The added cost of fuel fabrication due to the use of enriched nitrogen does have to be considered as does any problems with recycling the fuel.

Experimental Physics [ANL]

Scope

The scope of this activity consists in providing high quality experimental data. In order to simulate the physics and dynamic behavior of transmuter systems and to support their design, several experiments are performed or proposed. After the cancellation of the TRADE program, focus now for the experimental simulation of ADS dynamic behavior is on the RACE program being performed in USA, and the SAD program being performed in Russia. Evaluation of these two programs as well experimental support and leadership will be provided. Another experimental program, performed at the CEA (France) MASURCA facility, focuses on simulation of gas-cooled fast-spectrum systems that can be eventually used as transmuters. ANL personnel will collaborate with CEA and ISU in the experimental planning and conduct of critical and subcritical experiments of the ENIGMA and RACE programs. Experimental techniques will be developed, and measurements for the physics characterization of the different systems will be performed.

Highlights

TRADE

- Two additional papers were accepted for Physor 2006
  - G. Imel, et al., “ADS Reactivity Measurements from MUSE to TRADE (and Where Do We Go from Here?)”
  - M. Carta, et al., “RACE Project: Expectations in Comparison with TRADE”
- A final report on the low power TRADE experiments has been completed and submitted as the last deliverable of Coupling Experiments.

ECATS/RACE

- The ECATS target design group from FZK, CEA, and ENEA have evaluated options for a high power (~30 kW) target for RACE. A preliminary report has been issued.
- During the TRADE experiments, an anomaly was discovered for transients initiated from around 350 kW in TRIGA reactors, and attempts are underway to understand this behavior.

- A proposed experimental plan for RACE-LP (low power) to be presented to the U.S. RACE group in April was prepared.
- A document detailing the beam power and target material for RACE-HP (high power) was prepared and distributed for review. It seems necessary to have a U target in the center of the core to achieve 50 kW for k_{eff} even as high as 0.98.

ENIGMA

- The ENIGMA core loading is progressing. The four control rods and pilot rod were installed. The first criticality is planned for the end of June.

Technical Summary

RACE Target Development

It was decided in agreement with U.S. collaborators to (1) study a U-based "simple" target, defined as simple in geometry and easy to fabricate; and (2) study an "optimized target" (in any material).

A comparison of neutron production resulting from different target shapes related with the former studies is shown as follows:

Target / Target Shapes	Neutrons/sec
Infinite uranium	9.8E13
UNLV target (5mm of Tungsten+Uranium)	~ 6.3E13
TRADE solution 13c200 with Tantalum	~ 3E13
TRADE solution 13c200 with Uranium	~ 7.4E13
Preliminary design of the multi-disk target	~ 6.3E13

As can be seen, the U-based solutions have the highest gain compared to the Ta-based solution. It appears that the multi-disk concept is the most promising because of simplicity. It is based on a stack of clad U plates disposed in horizontal position with a slight inclination and cooled by water flowing in the horizontal channels, which lay between the plates. Calculations by CEA have shown that the cooling is sufficient in case of five plates having 6kW power each with a water flow of 3 m/s. The main question is in regards to the fabrication of the plates.

The first and second U plates must be about 1.5-mm thick and 65 mm in diameter. All plates must be clad. The cladding must be Al or Zr (or other low absorption materials). Assuming the cladding external temperature must be limited to 100ºC, the maximum temperature of U is 240ºC if the thermal contact between U and Al is tight. In case of poor contact and a helium gap, the maximum U temperature is 260ºC. These values are both within the acceptable criterion of maximum U temperature. The thickness of the U plates could be increased, which would ease the problems of

manufacturing the disks but would increase the coolant flow rate. Doubling the flow rate and doubling the U thickness (to ~3 mm) would lead to a well-proven manufacturing technology.

The U shape in thin plates with Al cladding was envisaged as a “simple shape” and therefore feasible. In case that the fabricability is not confirmed, the upper U plates will be replaced by Pb or Ta or W plates, paying a penalty in terms of neutron production, and the lower plates will coalesce to a single cylinder.

RACE LP (Low Power) Experimental Plan

Table 7 was developed following the March 8-9, 2006 meeting held at Cadarache, France. This represents the needs of the ECATS/Eurotrans partners from the US RACE project. The interest in even the low-power phase of RACE is increasing, as evidenced by the contributions of KTH (Sweden) and CIEMAT (Spain). These organizations originally had not planned to participate.

The RACE-LP phase is oriented towards confirmation of the techniques studied in MUSE and TRADE and studying current/reactivity/power relations for on-line monitoring.

RACE HP (High Power) Beam Power, Target, and Reactor Power

In order to study the relative merits of different beam powers, energies, and target materials, we define the energetic gain, G, as the ratio between core and beam powers. The gain is proportional to the source importance and target yields, and inversely proportional to the beam energy and reactivity.

The complete system (target plus TRIGA subcritical core) was simulated taking into account the electron, photon and neutron transport using the MCNPX code. In this model, source electrons, Bremsstrahlung photons, photo-neutrons and induced fission neutrons were transported for each history, allowing the estimation of several physical quantities relevant to analysis of the subcritical core and target coupling; viz., net multiplication factor, core fission power, etc. Two core configurations, representative of SC0 (-500 pcm) and SC2 (-3000 pcm) configurations of the TRADE experiment were considered coupled with four target types. The results are summarized in Table 8

We note that our desired objective is to obtain 50 kW of reactor power to ensure that there will be adequate reactivity feedback effects. Thus, for a 25 kW beam, we would need a gain of at least 2.0 to obtain 50 kW reactor power. As shown in Table 8 above, this is not achievable in the SC2 configuration, for any type of target. Based on this, we will likely not be able to run at subcritical levels as low as 0.97 and still have feedback effects. However, the above Table 8 does show the clear advantage of a uranium multi-plate target, yielding a gain of almost 5 in the SC0 configuration.

We then looked at four configurations to see the effect of using the Texas A & M core as opposed to the Casaccia core. These results are shown in Table 9, where beam energy of 25 eV and beam power of 25 kW was assumed, coupled to the uranium multi-plate target.

Table 7. Needs of ECATS/Eurotrans Partners from US RACE Project

	Items of experiments	Technical objective(s)	Location	Core configuration				Contributors
				Critical	SC0 *	SC2 †	SC3 §	
1	Study of gamma flash effect	Assess time detectors are blinded by gamma ray and how it affects msmt performed using PNS based technique	IAC					CEA
2	Source characterization	Production rate and energy spectrum and spatial distribution with tungsten/copper alloy, uranium; diagnostic techniques	IAC					CEA
3	Source monitoring	On line monitoring of neutron production rates	TAMU and/or UT					CEA
4	Characterization of the beam line	Assessing geometric stability and diagnostic consistency	TAMU					US
5	Source importance with Linac	Effectiveness of source due to location	TAMU					CEA
6	Kinetics parameter measurement (beff, L)	Assessment of absolute reactivities from a or r$ experimental values	Same core					US
7	Rod drop experiment	Reference reactivity level for ASM/MSM methods		X				CEA
8	ASM msmt	Ref. method for reactivity msmt			X	X	X	CEA, FZK
9	Rod worth	Determination of rod reactivity worth at various axial positions		X	X	X	X	CEA
10	PNS experiments with IAC accelerator	Reactivity calibration			X	X	X	CEA, CIEMAT, KTH, ENEA
10	PNS experiments with a DT source	Reactivity calibration			X	X	X	CEA, CIEMAT, KTH, ENEA
11	Cf Source jerk	Reactivity calibration			X	X	X	CEA, ENEA, KTH
12	Current to power relation	Online monitoring of reactivity			X	X	X	CEA, CIEMAT, KTH, ENEA
13	Reactivity msmt using beam trips	Interim cross check			X	X	X	CEA, CIEMAT, KTH
14	Γ-H characterization of critical core in power range 0-100 kW	Reference measurements in view of HP phase	TAMU and/or UT	X				FZK
15	Determination of reactivity coefficients in critical reactor in power range 0-100 KW			X				FZK
16	Reactivity insertion transients in 20 kW steps in power range 0-100 kW in critical reactor			X				FZK
17	Calibration of control rods in critical reactor			X				US
18	Power shape (axial & adial fission rate msmt)	Core characterization	TAMU and/or UT	X	X	X		CEA
19	Start-up and loading procedure	Overall methodology for reactivity monitoring (task 2.1.4)	TAMU and/or UT					All

*(keff ~0,995); †(keff ~0,97); §(keff ~0,95)

Table 8. Two TRADE Experiment Core Configurations (SC0 & SC2) Coupled with Four Target Types

	W-Cu Cylinder		W-Cu Conical		U Multi-plate Central		U Multi-plate Tangential	
	SC0	**SC2**	**SC0**	**SC2**	**SC0**	**SC2**	**SC0**	**SC2**
Electron energy E_e (MeV)	25	25	25	25	25	25	25	25
Accelerator current (mA)	1.00	1.00	1.00	1.00	1.00	1.00	1.00	1.00
P_{beam} (kW)	25	25	25	25	25	25	25	25
Target neutron yield γ_t (n/e)	4.12E-03	4.12E-03	3.86E-03	3.86E-03	7.99E-03	7.99E-03	7.99E-03	7.99E-03
Core (γ,n) contribution ε_c	0.11	0.11	0.16	0.16	0.09	0.07	0.01	0.004
Total neutron yield (n/e)[(a)]	4.57E-03	4.57E-03	4.48E-03	4.46E-03	8.74E-03	8.55E-03	8.04E-03	8.02E-03
K_{eff}	0.99323	0.97748	0.99041	0.97157	0.99450	0.97875	0.99346	0.97334
ρ_{eff} (pcm)	-682	-2304	-968	-2926	-553	-2171	-658	-2739
φ*	1.17	1.03	0.97	0.91	0.97	1.12	0.25	0.23
ρ_s (pcm)	-583	-2246	-997	-3225	-569	-1943	-2664	-12149
<S> (n/s)	2.86E+13	2.86E+13	2.80E+13	2.79E+13	5.46E+13	5.34E+13	5.03E+13	5.01E+13
$g=\gamma_t\cdot(1+\varepsilon_c)\cdot\varphi^*$	5.35E-03	4.69E-03	4.35E-03	4.05E-03	8.48E-03	9.55E-03	1.99E-03	1.81E-03
$<\nu\Sigma_f\varphi>$ core (n/s)	4.90E+15	1.27E+15	2.81E+15	8.65E+14	9.59E+15	2.75E+15	1.89E+15	4.13E+14
P reactor power (kW)	62.70	16.25	35.92	11.05	122.59	35.14	24.12	5.28
G	2.51	0.65	1.44	0.44	4.90	1.41	0.96	0.21

[(a)] $\gamma_t\cdot(1+\varepsilon_c)$.

Table 9. Texas A&M Core vs. Casaccia TRIGA Core

	SC2 Central TRIGA RC-1	SC2 Central Texas A&M	SC3 Central Texas A&M	SC2 Tang Texas A&M
Electron energy E_e (MeV)	25	25	25	25
Accelerator current (mA)	1.00	1.00	1.00	1.00
P_{beam} (kW)	25	25	25	25
Target neutron yield γ_t (n/e)	7.99E-03	7.99E-03	7.99E-03	7.99E-03
Core (γ,n) contribution ε_c	0.07[(a)]	0.07[(a)]	0.07[(a)]	0.07[(a)]
Total neutron yield $\gamma_t\cdot(1+\varepsilon_c)$ (n/e)	8.55E-03	8.55E-03	8.55E-03	8.55E-03
K_{eff}	0.98000	0.96816	0.95037	0.97639
ρ_{eff} (pcm)	-2041	-3289	-5222	-2418
φ*	1.01	1.27	1.16	0.26
ρ_s (pcm)	-2029	-2590	-4486	-9265
<S> (n/s)	5.34E+13	5.34E+13	5.34E+13	5.34E+13
$g=\gamma_t\cdot(1+\varepsilon_c)\cdot\varphi^*$	8.59E-03	1.09E-02	9.95E-03	2.23E-03
$<\nu\Sigma_f\varphi>$ core (n/s)	2.63E+15	2.06E+15	1.19E+15	5.77E+14
P reactor power (kW)	33.65	26.36	15.22	7.37
G	1.35	1.05	0.61	0.29

We note that a peripheral source position leads to very small gains, making even 25-kW reactor power unlikely. Running with a central target at k=0.97 does appear to yield 25-kW reactor power however, which might be enough to see feedback effects (even if below the desired level of 50 kW).

In Figs. 40 and 41, we show the core power vs. the subcritical level for the different targets, uranium and non-uranium. The results are normalized to 25 kW beam power.

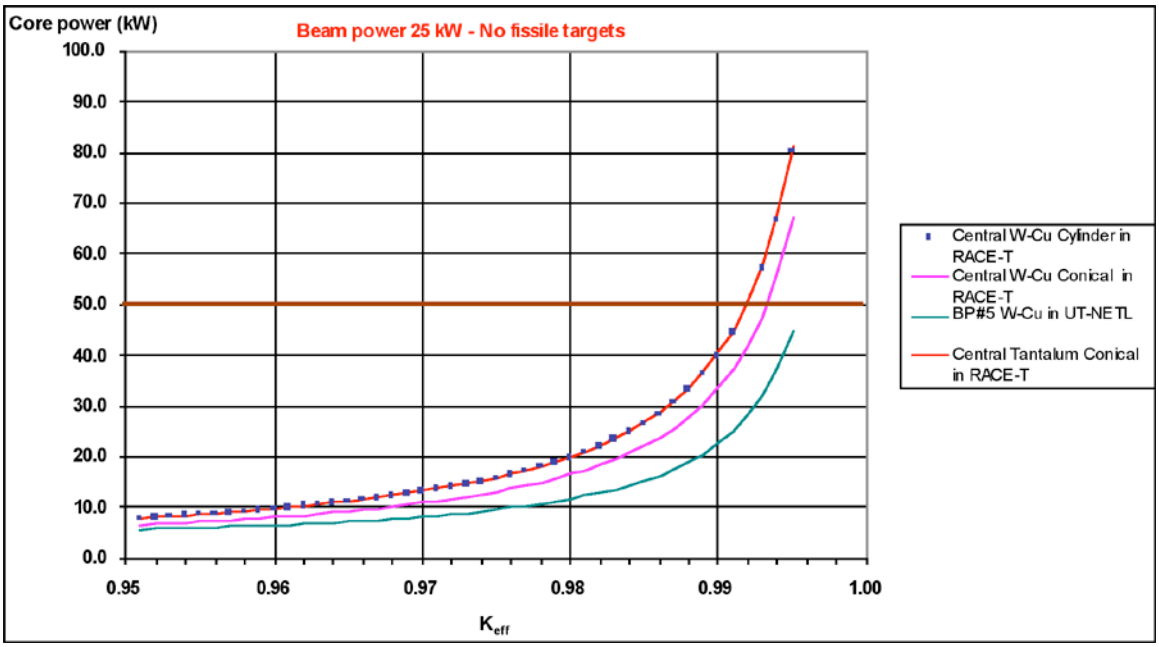

Fig. 40. Core power vs. the subcritical level for non-uranium targets

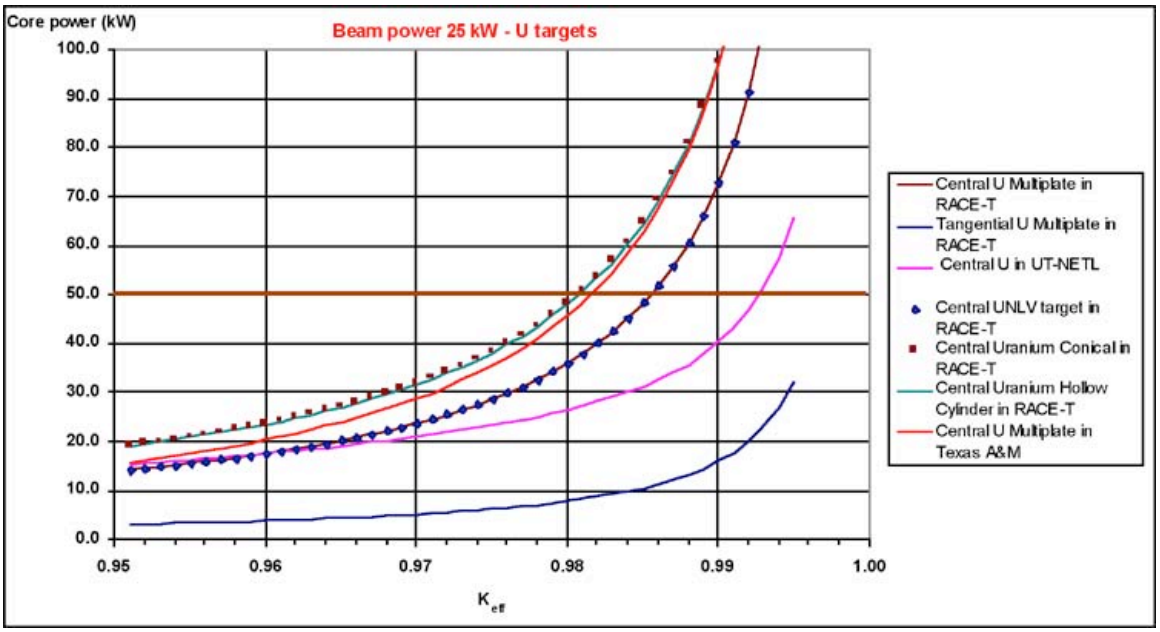

Fig. 41. Core power vs. the subcritical level for uranium targets

We can note a couple of points based on the preceding data:

- It seems necessary to have a uranium target in the central position to obtain a core power larger then 50 kW for K_{eff}>0.98.
- The results show that the tangential channel solution implies a penalization factor around 4 for the core power for the same beam power.

Transient Behavior of a TRIGA

An anomaly in the transient behavior of a TRIGA was uncovered during the TRADE experiments. There has been considerable effort made to understand this anomaly, because potentially it can affect the RACE high-power experimental phase. In short, for a transient initiated at around 370 kW, the measured fuel temperature spikes and then decays to a level very close to the original temperature (note: The RACE high-power experiments will not achieve this power level, but until the phenomenon is understood we don't know that this won't occur at much lower powers in another TRIGA with different fuel and geometry). This behavior is shown in Fig. 42 with the fuel temperature being the red trace and the power is the blue trace. The anomaly is that while the fuel temperature does not change before and after, the power level definitely increases in a consistent manner, which implies a vastly higher temperature coefficient in this regime.

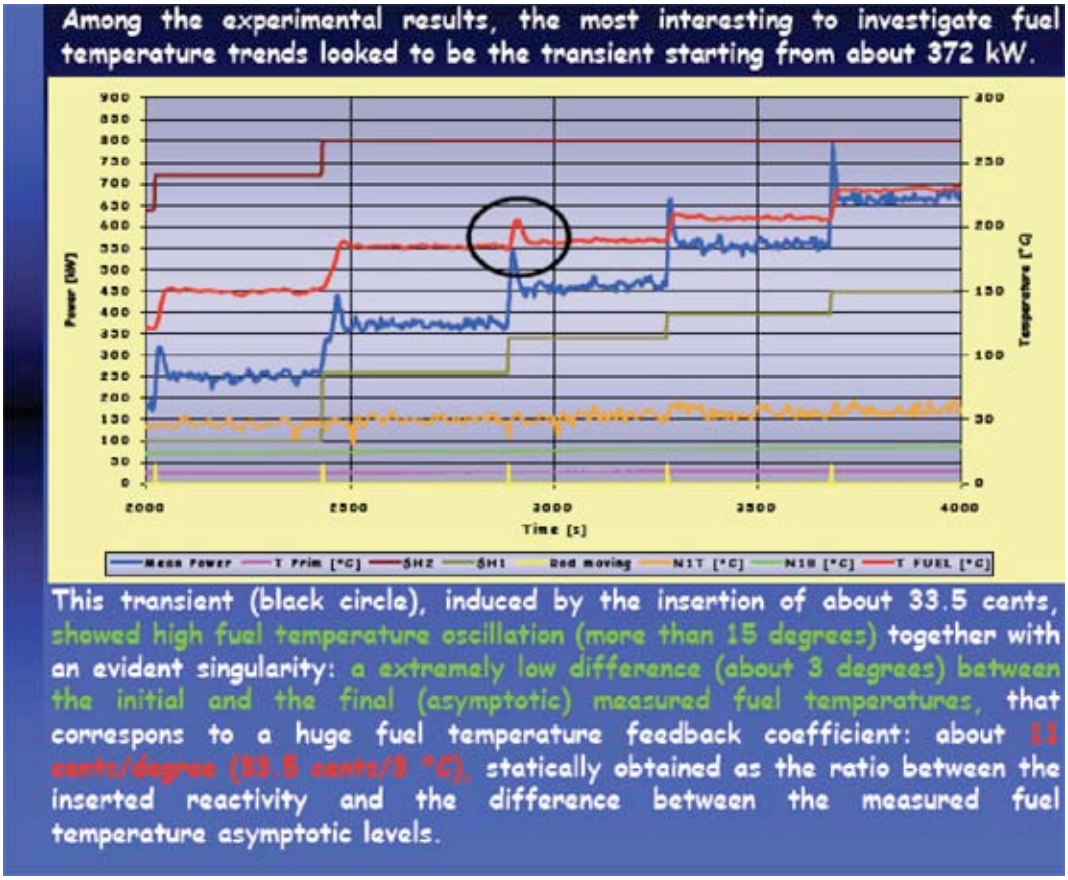

Fig. 42. Transient behavior of a TRIGA. The fuel temperature is in red and the power is in blue.

One hypothesis is that that the clad was overheated which would then be followed by the onset of nucleate boiling, explaining why the final temperature increase was so little. Calculations by ENEA have shown that nucleate boiling will begin at a flux of 6 W/cm². But, we don't know if this is true at different conditions (e.g., inlet temperatures).

RELAP5 calculations were performed for a hot channel and an average channel, showing some overheating of the fuel which occurs between 300 kW and 450 kW.

One problem with these measures is that the fuel temperature was only measured in one spot, which might not be representative of the rest of the core. It is hoped to redo some of these transients in the Texas TRIGA, where multiple instrumented fuel elements are available.

Another angle of investigation has to do with the feedback mechanism itself. Apparently it has been shown in the TRIGA in Slovenia that there is a peak to the feedback coefficient that occurs for a fuel temperature of around 130°C.

All of these studies have greatly contributed to the understanding of the TRIGA reactor behavior, but there is still work to be done.

Materials Test Station (MTS)

Research and development of advanced nuclear fuels and materials for the AFCI and Gen-IV programs requires an adequate fast-neutron irradiation capability to test candidate samples in a prototypic environment. Testing is necessary to prove the adequate performance of the fuels and materials prior to implementation of a demonstration reactor. The system must meet certain requirements for test volume, instrumentation, neutron spectrum, and physical conditions characteristic of the anticipated operating environment. For the fuels and materials being explored as part of the AFCI and Gen-IV initiatives, specific requirements include the ability to achieve a wide range of temperatures under tightly controlled conditions. It is recognized that a user facility of this type will also benefit other DOE programs and collaborations. Therefore, to address the performance and capability gap, the Materials Test Station will meet the following mission needs:

- Provide the capability to safely irradiate materials and fuels in a fast-neutron spectrum and in a prototypic temperature and coolant environment to meet the technology and proof-of-performance experimental needs of the AFCI and Gen-IV programs.
- Provide a user facility for the DOE to perform fast-neutron-spectrum irradiations for university and international collaborators, and other DOE programs.

Integration

A cost estimate and project schedule for the MTS was completed in January, fulfilling an AFCI level-2 milestone. The estimate shows a project cost range of $58M–$73M, with a scheduled completion date of September 2010. The cost estimate is documented in a LANL report (LA-UR-06-0197).

External Review Committee Report

The MTS External Review Committee issued in report of the Review held in December 2005. Regarding the irradiation capability, the Committee made the following observations and recommendations:

Observations

- Performance parameters for flux and burn-up have been met.
- Designers should be congratulated for completing first order trade-offs.
- Even at 10^{15} n/cm2/s, the fast flux is still only half that typical of a fast reactor.
- The neutronic models used are necessarily idealized at present. The effect of adding engineering detail will likely be to reduce the flux available.
- A Ta-W target with HIP bonding has been used successfully at ISIS with low power density. It is unclear if the bond at high power density will retain its capability to diffuse transmutation gases.
- Requirements for material-irradiation studies introduce a large number of vacuum penetrations and complexity to the target design.
- There are significant benefits to the MTS relative to other facilities, particularly in terms of higher flux capabilities.

Recommendations

- Further analysis should be conducted to evaluate peak flux with realistic sample loading.
- Calculate realistic ranges for power density and He/dpa ratios.
- In collaboration with ISIS, utilize a high dose sample from STIP-2 to analyze the HIP bond integrity.
- Minimize the number of He circuits for temperature control of material irradiation canisters.
- Material samples for cladding should be irradiated after prototypic processing and in prototypic configuration, i.e., in a cylindrical configuration.
- It is important not to preclude improving performance parameters, at least through conceptual design. During conceptual design, means for improving performance parameters should be identified. Perform trade studies. For example, sacrificing irradiation volume for even higher flux may be a reasonable decision during conceptual design. There appears to be good margin on the volume. Perhaps a 50% reduction in volume would be reasonable.
- Don’t limit potential fuel pin power. Current power estimates appear to be in the normal regime. 500 W/cm (assuming 0.25 cm radius) would be a good target.

- There is a direct interaction between the calculated neutronic performance parameters of the MTS on one hand and the mechanical, thermal, and hydraulic design of the target assembly on the other. Therefore it is important to be aware of the interfaces between the two so that the optimization of one does not result in the degradation of the performance of the other. Ensure that operational transients experienced by the fuel (and other components) are analyzed during conceptual design, e.g., instantaneous power on, pulsed beam structure, etc.
- Assess what features can be incorporated in the MTS design now to make the addition of alternative missions easier in the future, e.g., LPSS demonstration, isotope production, high energy neutron beam line, etc. Evaluate the potential impacts of such features on the primary irradiation mission.

In the Summary Section of the report, the Committee stated the following: "The committee believes that the MTS design team has a good understanding of its design framework and has a well-developed concept. The committee also believes that the design team is ready to begin a formal conceptual design, and that open questions developed during this review can be resolved during conceptual design.

Major effort on the design side was concentrated on evaluating passively safe proton beam shutdown and passively safe decay heat removal under plausible accident scenarios. Initial indications are that both of these features will be difficult to accomplish. Without these passive safety features, unmitigated accidents may well lead to significant off-site doses, leading to a requirement for the equivalent of safety-class active safety systems.

J. Eddleman of LANSCE-MDE was selected to lead the Hot Cells and Remote Handling activities within the project. John already has responsibility for Area A preparation work, an activity is currently suspended due to lack of funds.

A Baseline Change Proposal was submitted to and approved by DOE-NE for spending $800K of the $3.465M FY06 MTS allocation. Four additional AFCI level-3 milestones were added to existing work packages as part of the BCP. Also submitted to NE was a work plan associated with the remainder of the FY06 allocation. The $800K allocation will allow the project to proceed with design activities through May 2006.

An overview of the MTS project was presented to LANL's Nuclear Technology Assessment Advisory Group on March 2. The project was well received. The draft meeting minutes state "NTAAG recommends that a knowledgeable Review Board be convened to review LANSCE operations/programs, and make recommendations for the continued operation of this important facility to support NNSA, OSc and, in particular, NE programs. The Review Board should provide a critical review of the MTS flux vs. other possible fast neutron sources for fuel irradiations."

Neutronics Design

Several physics and neutronics issues of the MTS target design were explored during this quarter.

Target Calculations

Three different front face designs for the target modules were used for calculations (see Fig. 43). The neutron yield for each was assessed. Only minor differences were noted between the three designs although, in general, having the least material in the front face is most desirable.

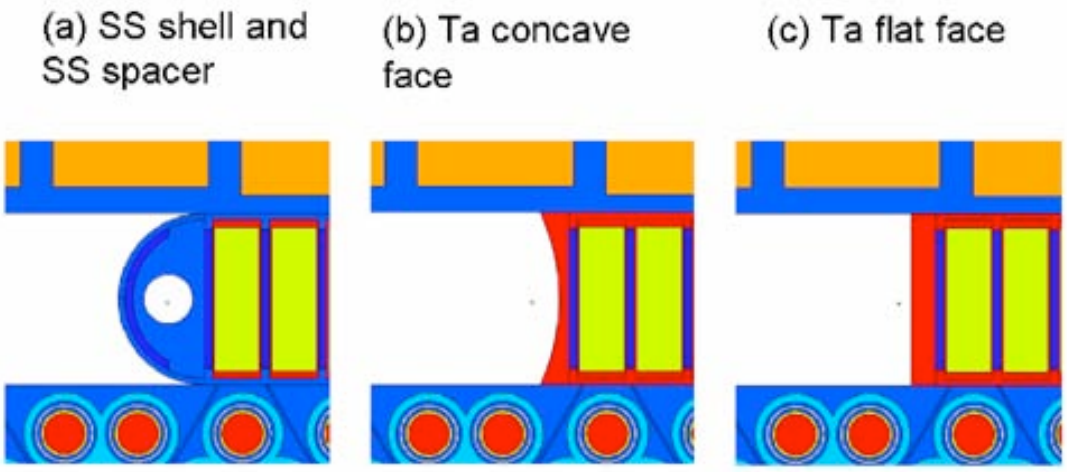

Fig. 43. Target Front Face options.

Further calculations were performed to judge the effectiveness of reflector material as a function of distance from the target. Previous designs had assumed a cylindrical tungsten reflector surrounding the target out to 43 cm. It was found that this could be reduced without impacting irradiation performance. The present design uses a smaller reflector which reduces the cost and weight of the target.

A study was made assessing the effect of changing the clad materials to stainless steel and reduced thickness from 0.250 mm to 0.127 mm. The effect on overall neutron yield was noticeable, the effect being about a 1.6% drop. This study was done because some target design options may need to consider using stainless steel as a clad material.

Other calculations that were performed involved an energy breakdown by module and detailed breakdowns in target and backstop plates. In order to size the cooling requirements, the major target pieces needed to have their heat loads defined. MCNPX calculations were run to gather the heat loadings required by the designers. Table 10 gives the approximate heating levels for the major components at 1 mA of beam operation.

Table 10. Heat Loads for Major Target Components

Module	Heat Loading at 1 mA (kW)
Fuel	121
Target (2)	189 ea.
Materials (2)	51.7 ea.
Backstop	121.4
Reflector and Shielding	~115 kW

The option of altering the fuel module to accommodate a single row of fuel elements would reduce the size of the interior flux trap and increase the flux within the trap. However, this comes at a cost of reducing the number of fuel elements and increasing the He/dpa ratio, especially at the rear of the irradiation volume. This tradeoff was assessed by calculating the change in flux and other irradiation parameters for the single-row design. The number of fuel pins that could be accommodated was reduced from 36 to 20. The overall flux increase was around 10% in the peak flux region. The He/dpa ratio change varied by position. In the front of the flux trap, it remained constant. In the peak flux region, it increased by ~15%. Towards the rear of the flux trap, the increase was greater than 25%. Figure 44 shows the neutron flux map and irradiation conditions at 3 locations.

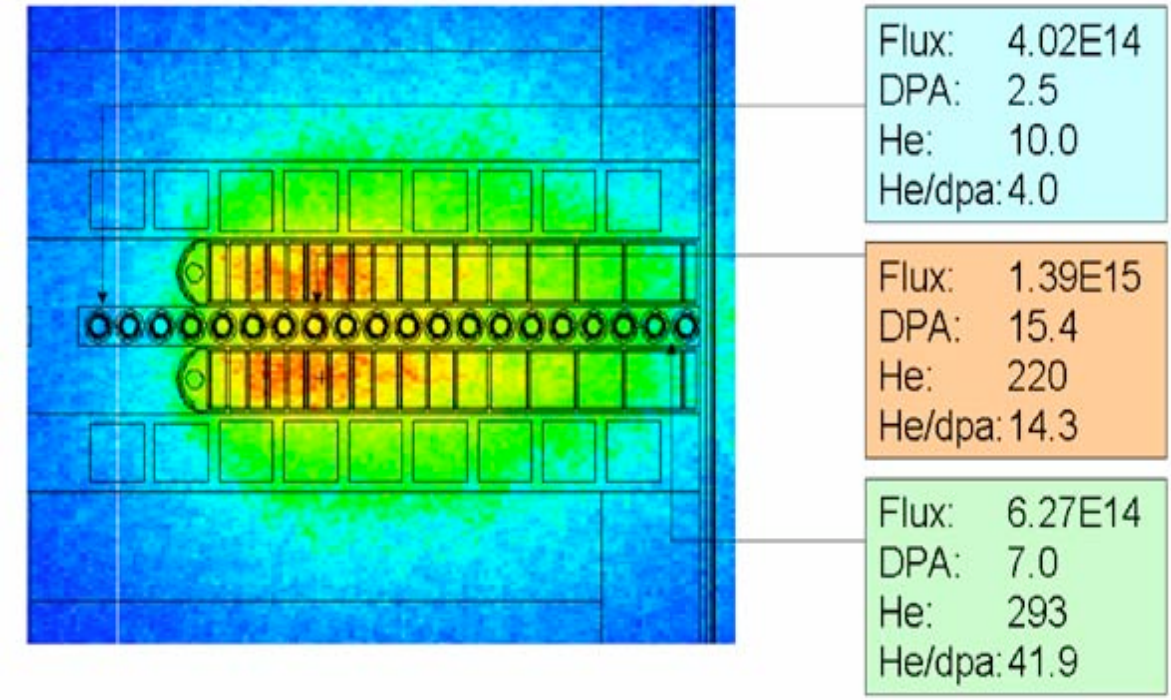

Fig. 44. Neutron flux conditions for single row design. Flux numbers are total flux in n/cm^2/s at 1mA of proton current. Protons enter from the left.

Shielding and Activation

Estimates of N-16 production were made using the MCNPX model of the target and this production was used as a source term to determine the dose in various parts of the facility due to the N-16 circulating in the coolant. Initial shielding estimates were performed from this estimated source to determine the efficacy of shielding radiation-sensitive components from the activated cooling water. More detailed shielding calculations will be done when design of the TRAM and service cell are more advanced.

Finally, shielding calculations were performed to estimate the dose in the service cell during operation from prompt neutrons penetrating the bulk shield material. For these

scoping calculations, contributions from radiation streaming through gaps in the shielding were ignored. As shown in Fig. 45, several material combinations were calculated; the most promising in terms of cost, ease of construction, and shielding performance is a mix of magnetite ore and concrete.

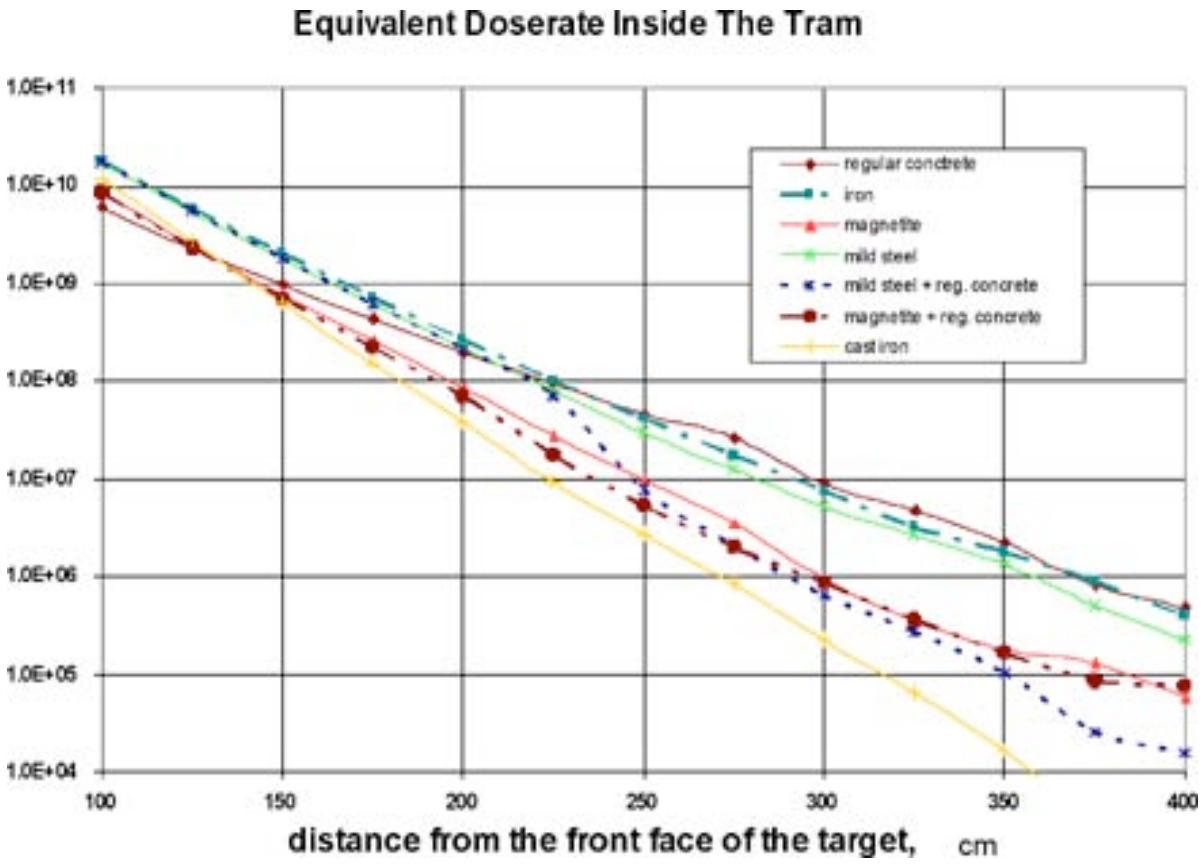

Fig. 45. Shielding calculations along the length of the TRAM

Target Assembly

Overview

Last quarter, the target assembly design details were advanced to the point of a viable pre-conceptual design. During this quarter, we continued to add depth to the design and evaluate potential changes to the design with the goals of improved performance, reliability, safety, and simplicity.

The current baseline design of the target assembly consists of a fuel sample module sandwiched between two target modules, which are in turn sandwiched between two material sample modules. These modules are bolted into an assembly, together with a backstop of stacked tantalum plates. The assembly is illustrated in Fig. 46.

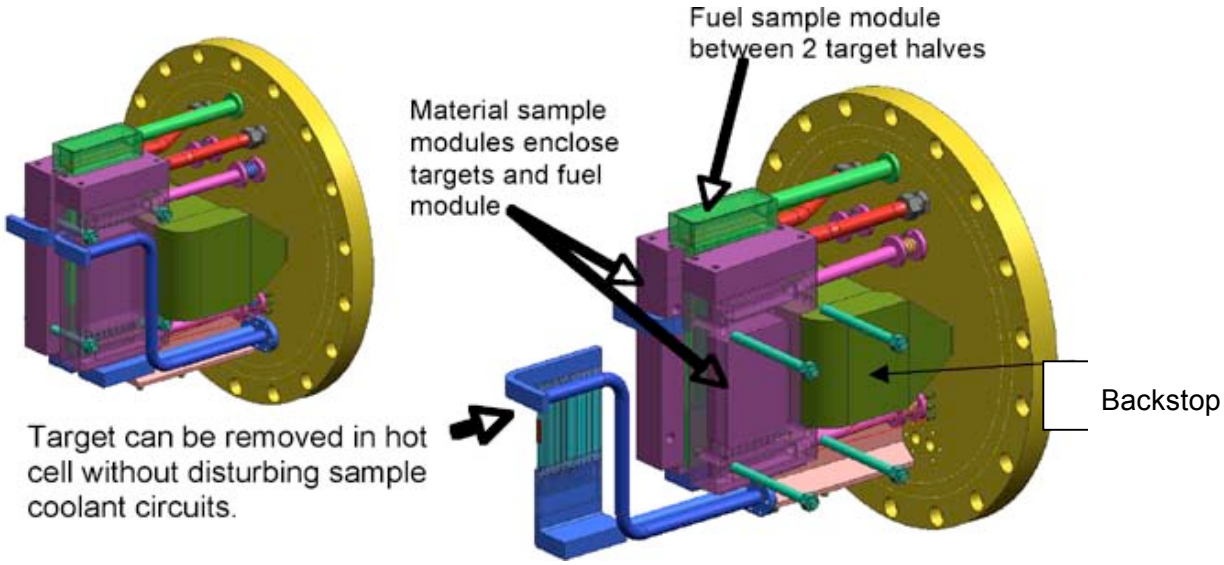

Fig. 46. Target assembly mounted to flange; exploded view shows one target module removed.

Design Trade Studies

The current baseline cooling design is parallel flow through each of the fuel, target, and material sample modules. Investigations were initiated to evaluate the feasibility of changing the cooling flow through these modules to series flow. The primary driver for this change is that series flow enables the detection of blocked cooling channels. In addition, series flow is beneficial because total coolant flow through each module would be reduced and coolant temperature rise would increase. These effects would serve to reduce heat exchanger and pump sizes. Initial calculations indicate series flow is feasible in both the fuel and material sample modules. For series flow through the target modules, however, pressure drop is excessive. Therefore, alternative designs are being investigated that divide the target module coolant into two or more separate series flow lines.

Figure 47 shows a segment of the water volume within a series-flow, fuel sample module. The water volume in Fig. 47 is a solid created of the void space inside the fuel sample module. In this figure, the water inlet is in the upper right. Cooling passages are shown for four complete cloverleaves (out of 12) and the beginning of the fifth cloverleaf. Series flow in the fuel sample module reduces the volume flow rate from 286 to 24 lpm (75.6 to 6.3 gpm). The coolant temperature rise and approximate pressure drop for series flow are 60ºC and 1.45 MPa (210 psi), respectively.

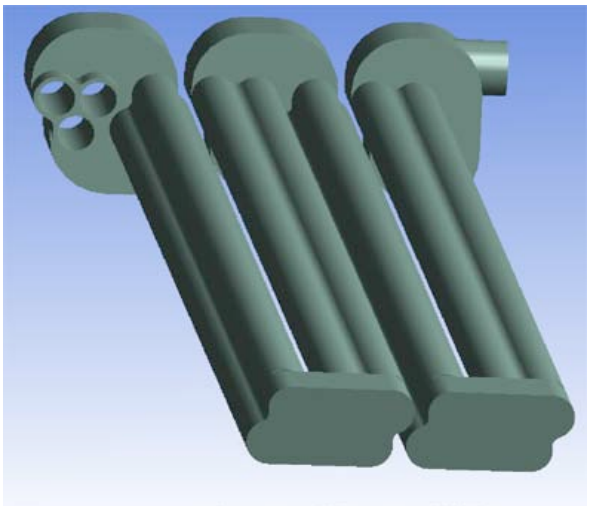

Fig. 47. Series flow water volume in partial fuel sample module.

Figure 48 shows a series-flow material-sample module design. On the left is a view of the external structure. On the right are solids representing the water- and gas-cooling flow passages. Series flow in the material sample module reduces the water volume flow rate from 78.4 to 8.7 lpm (20.7 to 2.3 gpm). The water temperature rise and approximate pressure drop for series flow are 60ºC and 240 kPa (35 psi), respectively.

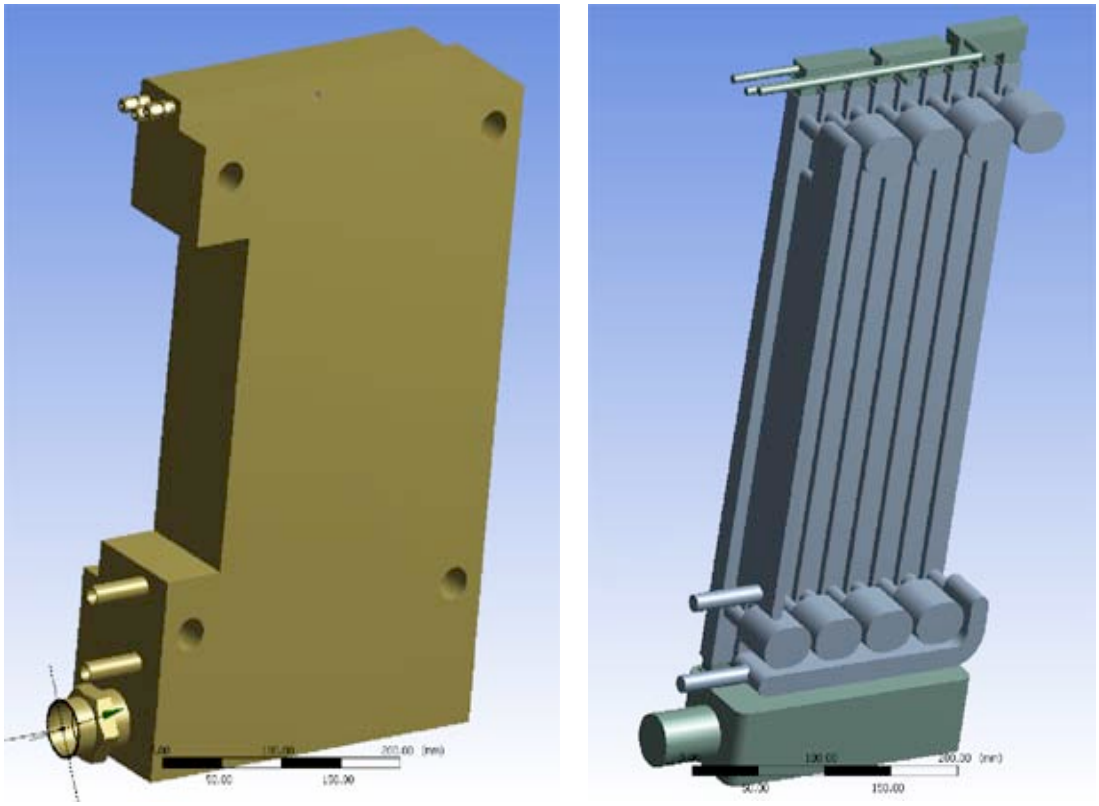

Fig. 48. Series-flow material-sample module; exterior structure on left, internal volume of water space (grey) and gas space (green) on right.

The stainless steel target housing design, as was presented at the Conceptual Design Review, was chosen to remain as the baseline design. A detailed evaluation has been performed for several all-tantalum designs, including structural and thermal analyses. The results of these analyses indicate that the tantalum designs provide marginally adequate performance based on ASME Pressure Vessel Code. Also, current knowledge of the behavior of tantalum under MTS target-irradiation conditions is insufficient.

Evaluation of the advantages and disadvantages of adding a window has concluded. The MTS safety-by-design strategy is to rely as much as possible on passive beam shutdown and decay-heat removal in the events of a loss of coolant accident (LOCA) or loss of flow accident (LOFA). Passive beam shutdown will be by way of gas or water vapor expanding down the beampipe, thus not requiring a window.

Decay Heat Removal

Decay heat removal investigations are being performed on the target and fuel modules. In one such analysis, a LOCA was assumed for the fuel module only. The decay heat from the fuel was assumed to conduct to the adjacent target modules (Fig. 49). The current project assumption is that a LOCA will occur for only one of these three modules (either the fuel module, or one of the target modules) in a single event. Since the target and fuel module structures are separate, an additional conduction resistance is encountered for the heat flowing across module boundaries.

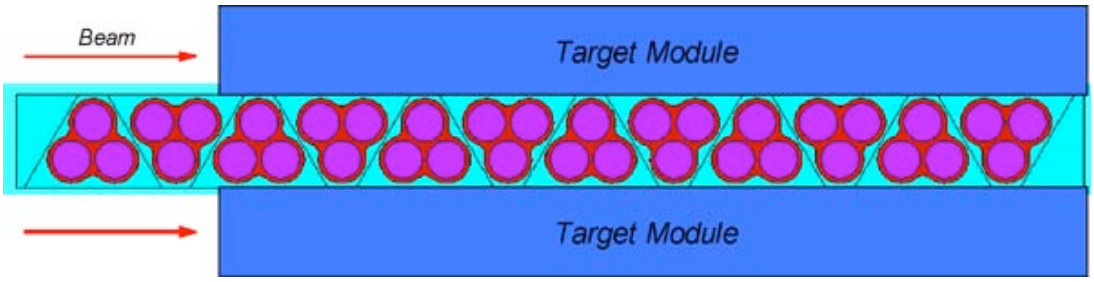

Fig. 49. Decay heat from fuel module removed by adjacent target modules.

A steady-state analysis was performed for the decay heat rate at one minute after beam shutdown. The resulting temperatures in the baseline fuel module are shown in Fig. 50. The peak temperature in the module was 1470ºC and occurred in the forward-most cloverleaf. One option for reducing the peak temperature is to remove the forward-most cloverleaf. For this reduced-volume configuration (also shown in Fig. 50), the resulting peak temperature was 820ºC near the center of the fuel module.

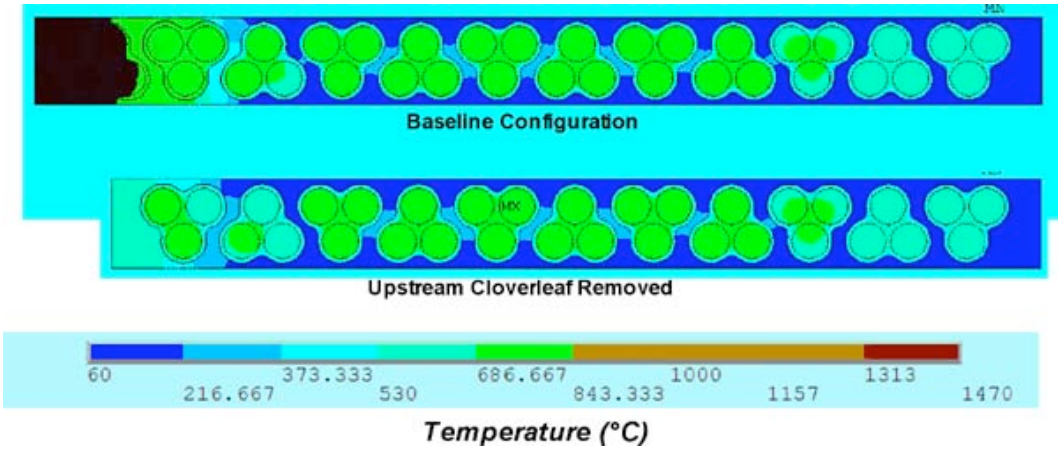

Fig. 50. Resulting decay heat temperatures (°C) for baseline configuration (upper) and upstream cloverleaf removed (lower).

Another approach being investigated for facilitating decay heat removal is to integrate the fuel and target module structures into a single, stainless steel body. The primary driver for this investigation is to remove the module-to-module conduction resistance. In the event of a LOCA, decay heat removal to the neighboring modules will be facilitated via conduction through the integrated structure, without module-to-module contact resistance.

Prototype Target Plate Cladding

Two successful HIP (hot isostatic press) cycles for target plate cladding have been completed, one with 0.38 mm (15 mil) tantalum clad and the second with the desired 0.25 mm (10 mil) clad. The tantalum cladding was bonded to 6-mm-thick tungsten target plates inserted into 6-mm-thick tantalum frames (see Fig. 51).

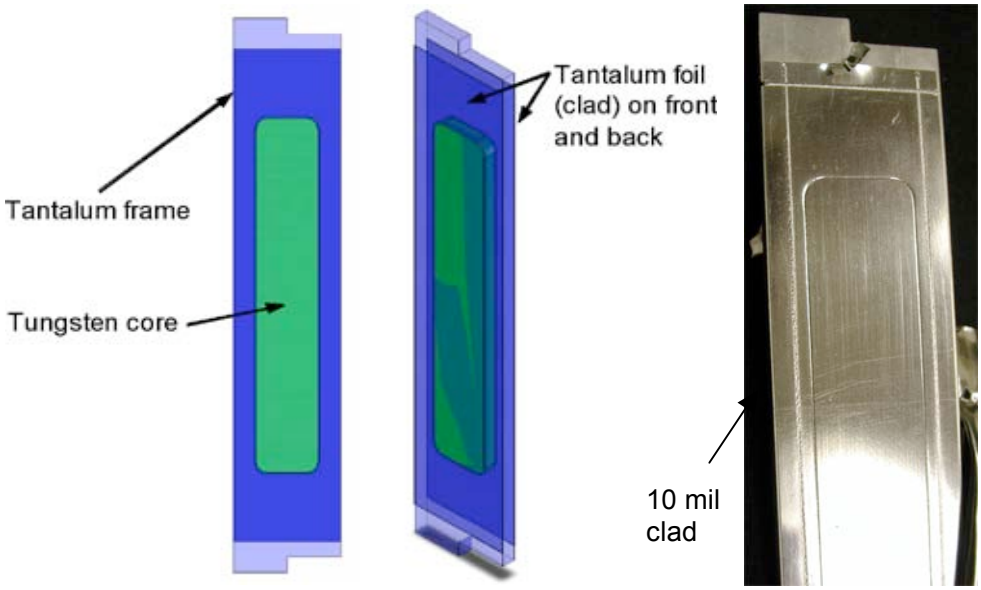

Fig. 51. Target plate configuration shown with 10-mil clad prototype (right).

Straightness measurements on the prototype plates indicate no significant warping occurred during the HIP process. Micrographs of the tantalum-foil-to-tantalum-frame e-beam welds show good bonds with grain growth across the boundary (Fig. 52). Optical and SEM evaluations performed on micrographs of the three-way interface between the tungsten plate, tantalum frame, and tantalum clad, also indicate good bonding. Currently, this effort has been postponed due to lack of funding.

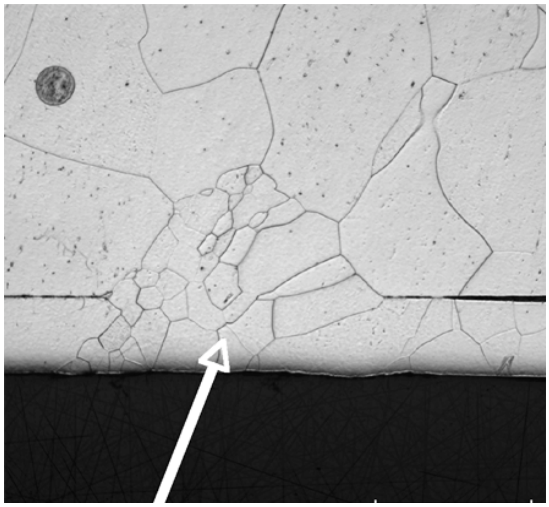

Fig. 52. Section of tantalum-foil-to-tantalum-frame e-beam weld showing grain growth across boundary.

Target Plate Cooling Experiments

Significant progress has been made toward the initiation of target thermal-hydraulic testing. A test heater was designed to simulate the high heat flux environment (600 W/cm^2) that the target plates will encounter in-beam (Fig. 53). The test heater is being constructed out of copper in two halves. Each heater half will focus the power of 12,500-Watt cartridge heaters to a 1.5-cm x 6-cm simulated beam spot inside the cooling channel (Fig. 54). The two halves will be brazed together to form the 1-mm x 18-mm cross-section water-cooling channel. The initial machining of the heater halves was completed (see Fig. 55); these parts have been successfully brazed and the test heaters are currently undergoing final machining.

An existing water flow test loop is being upgraded to accommodate the target thermal-hydraulic testing. A schematic of the modified flow loop is shown in Fig. 56. Modifications include the addition of a high-pressure booster pump capable of generating 500-psi water flow. Modifications will be completed soon and testing of these heaters will take place during the third quarter of this year.

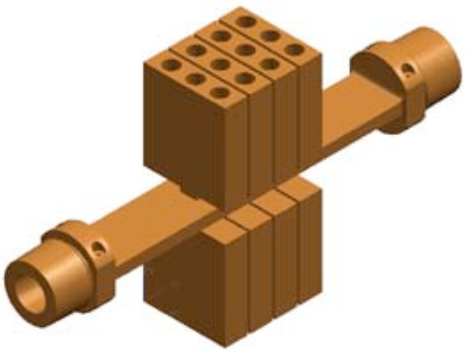

Fig. 53. Isometric of planned target test heater.

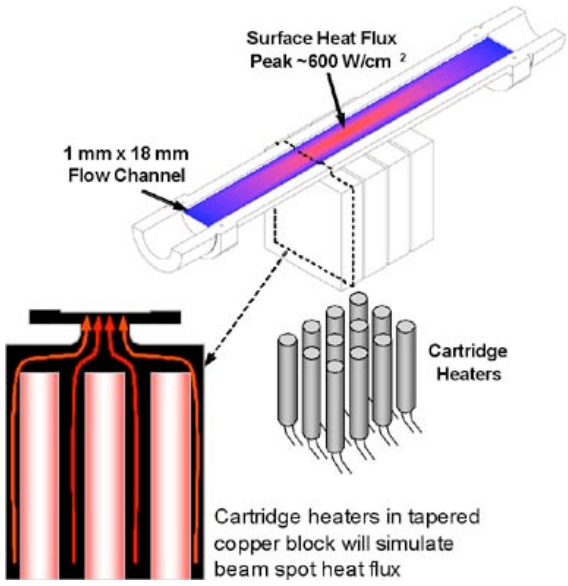

Fig. 54. Test heater half showing heat flow path.

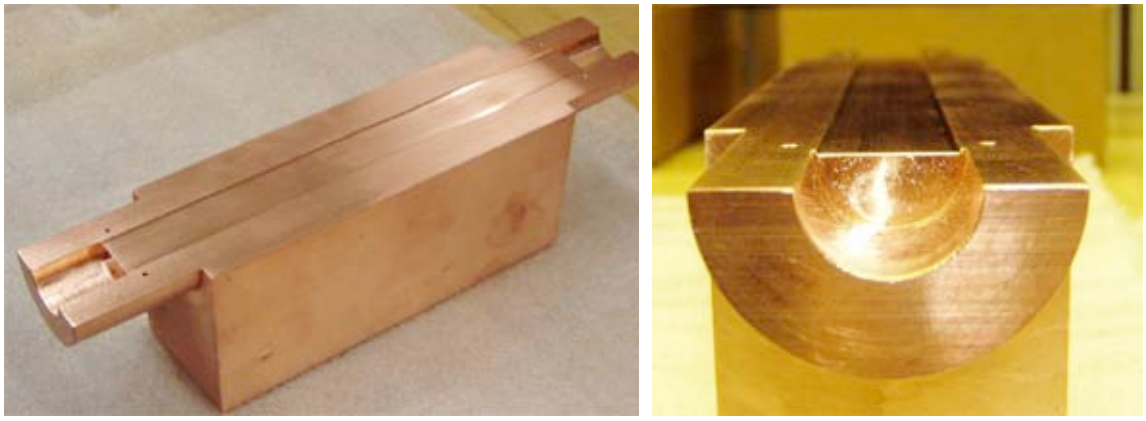

Fig. 55. Initial-machined heater half prior to brazing.

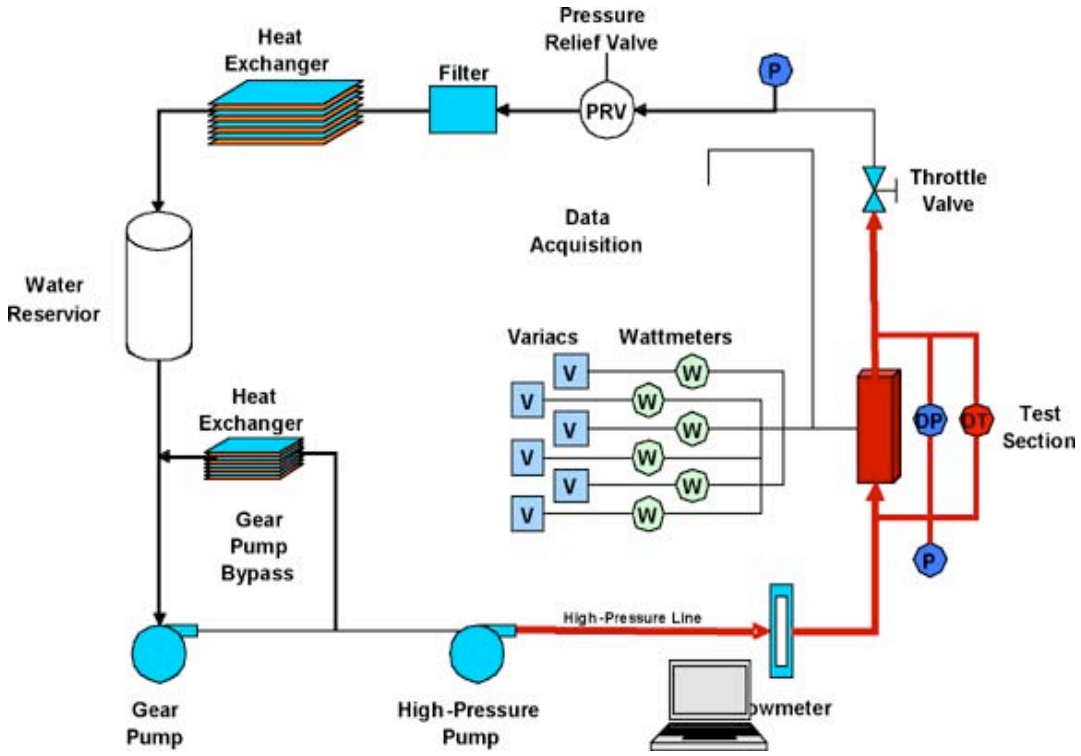

Fig. 56. Flow loop schematic.

Auxiliary Systems

Target Resource Auxiliary Module (TRAM)

A decision-matrix spreadsheet was developed to assess the configuration of the MTS service cell and its placement relative to the inner shielding and helium tank. Two alternative arrangements are compared and contrasted, identifying performance of each alternative against an array of functional requirements.

A target cooling system schematic was created that represents a system with separate fluids for target and sample modules and separate pumps for each module, but common coolant conditioning components. This system offers control of cooling flow through individual modules and LOFA redundancy, while minimizing system complexity. A portion of this schematic diagram is shown in Fig. 57.

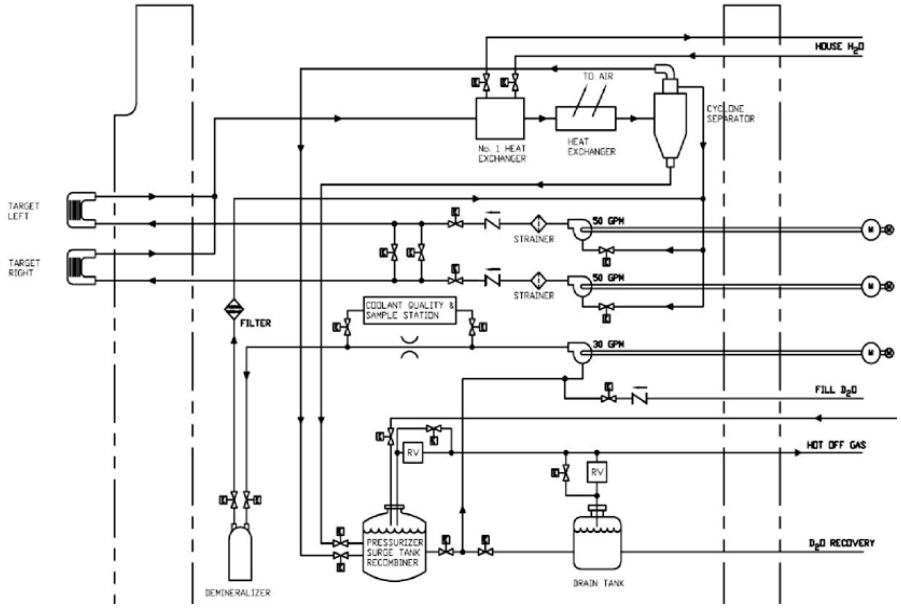

Fig. 57. A portion of the target cooling system schematic. During a LOCA, flow from an adjacent pump can be directed to the module served by the failed pump, providing adequate flow to carry away decay heat.

A schematic was also developed for a cooling system that has six separate isolated subsystems. This system may reduce the susceptibility to a LOCA situation, as the other five subsystems would still function and may carry away heat by conduction to adjacent modules. Work continues on configuring a failure tolerant design that maximizes reliability.

A portable service-shield model was created which allows direct servicing of the static seals between the TRAM and the helium vessel. This method provides a simple, effective procedure for exchanging the static air-to-helium and helium-to-vacuum seals, without compromising the operational effectiveness of the MTS facility. The seal service shield is illustrated in Fig. 58.

A method for sealing the helium, vacuum, and air atmospheres at the helium chamber TRAM port was revised. This revision configures the helium-to-vacuum seal pair as a face seal, rather than as a radial seal. This change improves the serviceability of the seal assembly, at the cost of a small amount of additional radial space required to mount the seal assembly. This seal configuration retains all the operational advantages of a no-tools TRAM cycle, *in situ* seal performance monitoring, and robustness against settling or drift over the operational life of the facility. A metal bellows allows relative motion between the vacuum chamber and the wall of the helium tank, maintaining the precision placement of the target relative to the proton beam. The revised seal configuration is shown in Fig. 59.

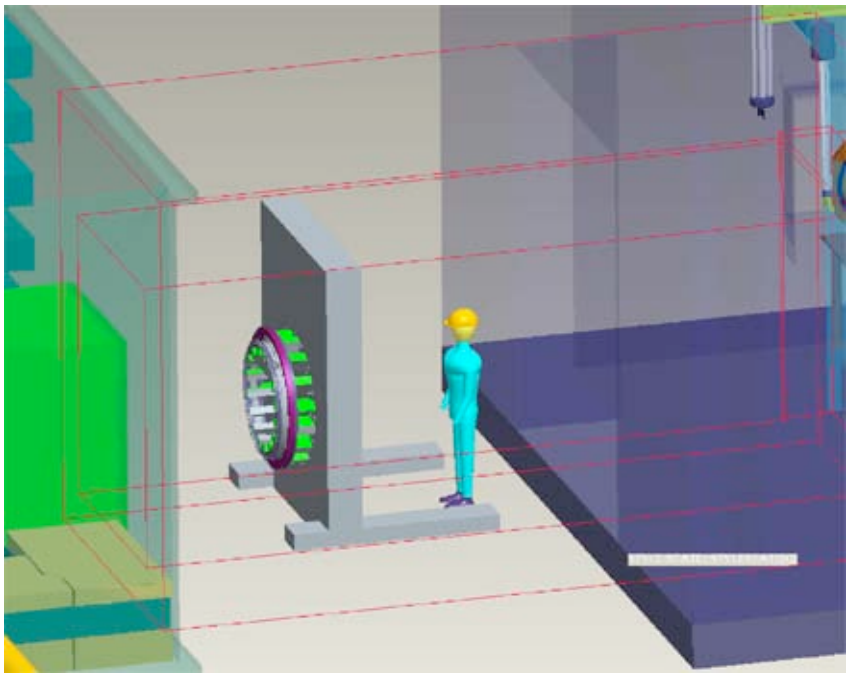

Fig. 58. Image of a service shield that allows direct servicing of the static seals between the TRAM and the helium vessel. The active seals, which are opened each time the TRAM is cycled, ride on the TRAM and require no manipulation to cycle the TRAM.

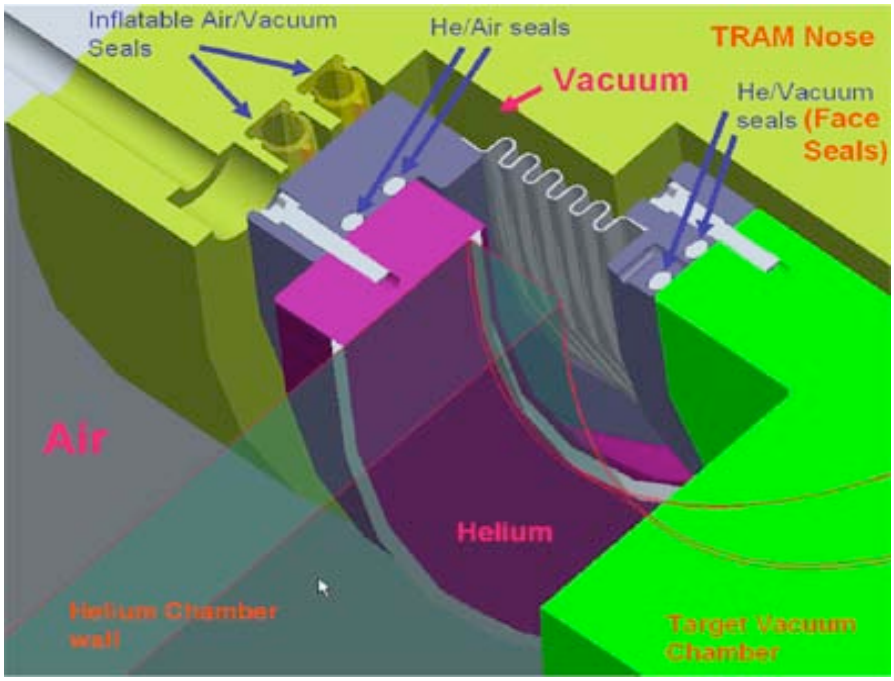

Fig. 59. A revised seal configuration, placing all seals in a face loaded condition. Three pairs of seals separate the three atmospheres. A metal bellows provides Target Chamber isolation. One seal integrity check port is visible in this section view; the other two are in other sections.

The design of the TRAM drive system was refined. The drive system uses two independent drive motors in parallel. Either system is capable of moving the TRAM. Commercially available components that meet requirements were selected. Figure 60 shows the arrangement of the components of one side of the drive system. The ends of the TRAM drive chains are anchored to the steel substructure of the equipment room floor, as illustrated in Fig. 61.

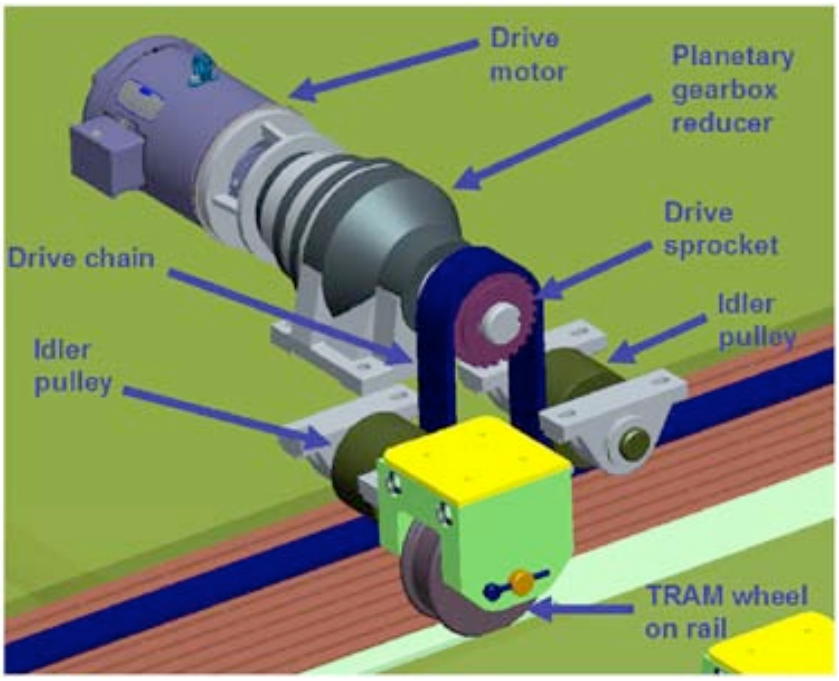

Fig. 60. Components of one half of TRAM drive system, showing motor, planetary gearbox, drive sprocket, and idler pulleys.

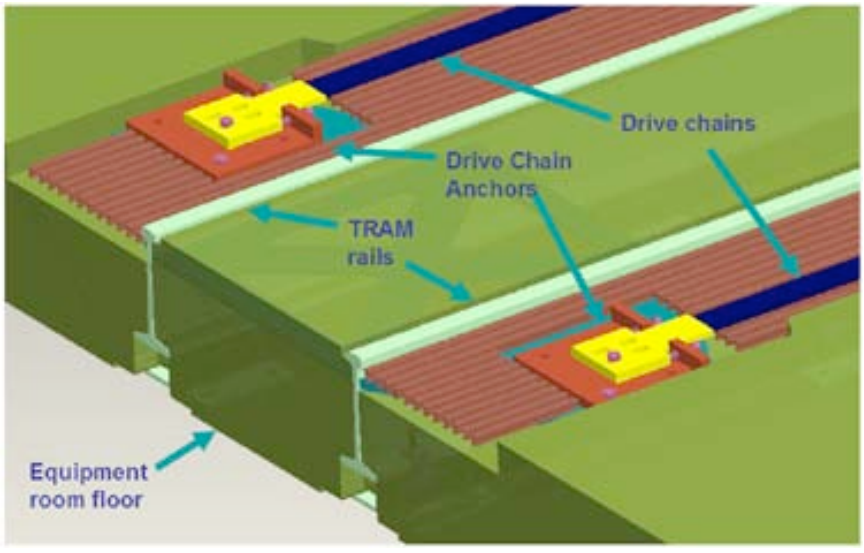

Fig. 61. TRAM drive chains are anchored to steel substructure in the equipment room floor. The chain anchors provide means for adjusting the tension in the drive chains.

A variation of the TRAM was modeled as part of a cost-performance study, and is illustrated in Fig. 62. This variation appears to offer simpler construction at the cost of some functional performance. This concept incorporates a movable saddle shield that covers the components on the TRAM during operation, reducing radiation damage to hot-cell windows. Figure 63 shows the saddle shield retracted to allow service of TRAM components in the hot cell.

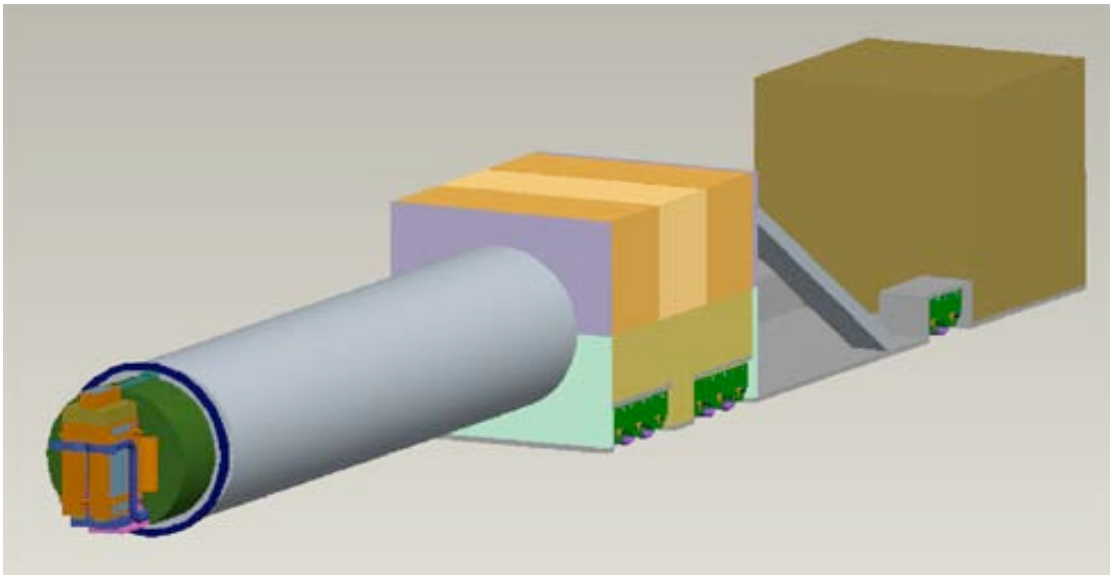

Fig. 62. A TRAM variation modeled as part of a cost/performance study.

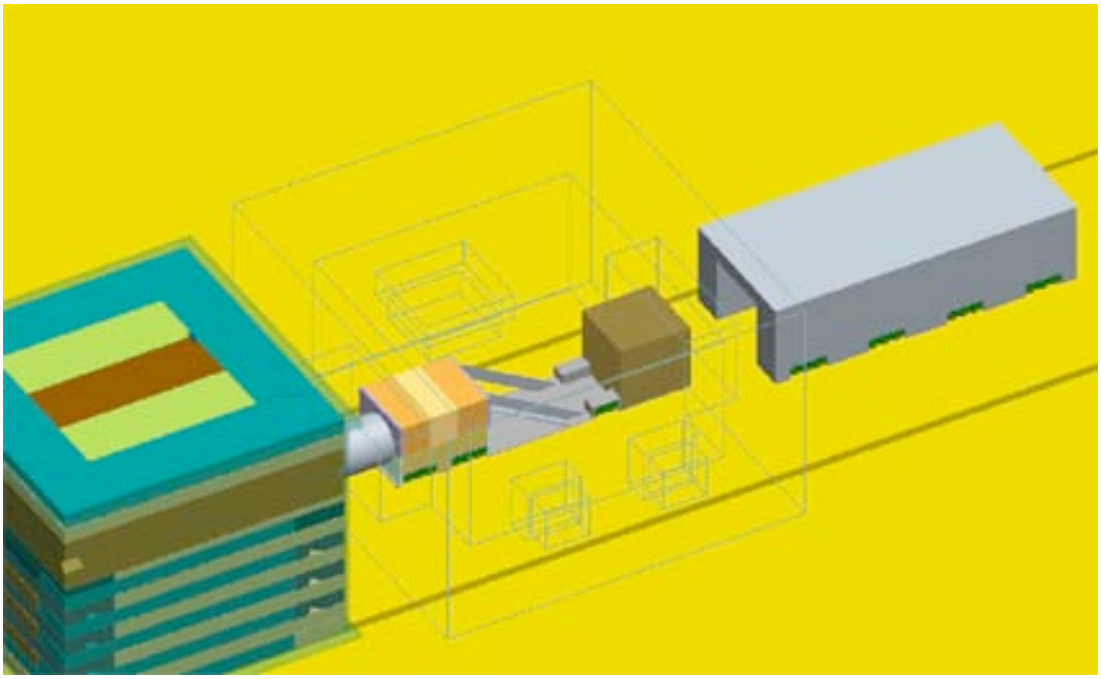

Fig. 63. TRAM and movable saddle shield. Hot cell is shown in wire frame. The airlock building to the right of the hot cell is not shown.

During this report period, Argonne Engineers created a conceptual arrangement, code named “Winchester”, which places the TRAM perpendicular to the proton beam, efficiently meeting operational requirements. This configuration places the critical mechanical components and seals in a region where radiation levels are lower, allowing improved component life and simpler shielding. All radioactive TRAM components are within the shielded tunnel during operation, so that the hot cell is not subjected to radiation. Grade-level ingress and egress are provided with the TRAM extended or retracted, providing a simple, safe method to move materials into and out of the cell in a production environment. Seismic safety is easier to achieve by maintaining operations on a single level. An isolated sample preparation cell is provided within the hot cell for specialized operations that may be required for pre- and post-processing of samples. There is no need for a pump house/air-lock building or a saddle shield vehicle in this configuration, conserving floor space, simplifying operation, and saving cost. Key features of the Winchester configuration are illustrated in Fig. 64.

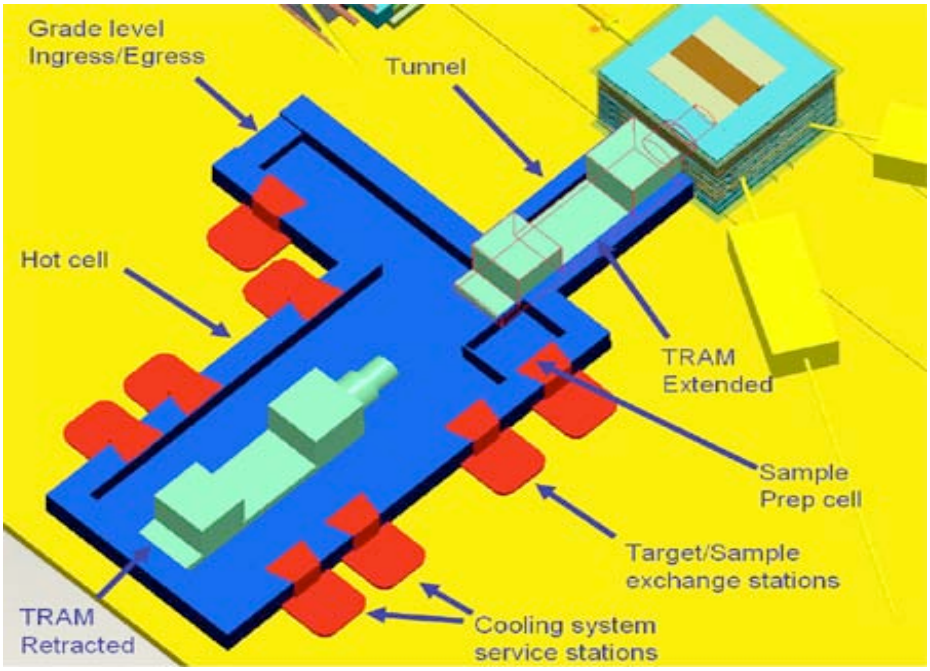

Fig. 64. The “Winchester” configuration provides simple TRAM motion, grade level ingress/egress, a sample prep cell, and a hot cell that is empty during beam operation. The TRAM is shown in both operational positions.

This configuration would likely accommodate the installation of up to two single event upset beamlines at 30º to the axis of the proton beam. Details of the hot cell bridge crane and the transfer cart system are illustrated in Fig. 65.

Finally, a concept for a configuration that employs a two story hot-cell and an air-lock building to support a Pipe TRAM concept was modeled. A saddle shield vehicle is required to cover the active components on the pipe TRAM during operation, to minimize radiation damage to components in the hot cell. This pipe TRAM configuration is illustrated in Fig. 66. The walls of the air-lock building may not need to provide radiation shielding.

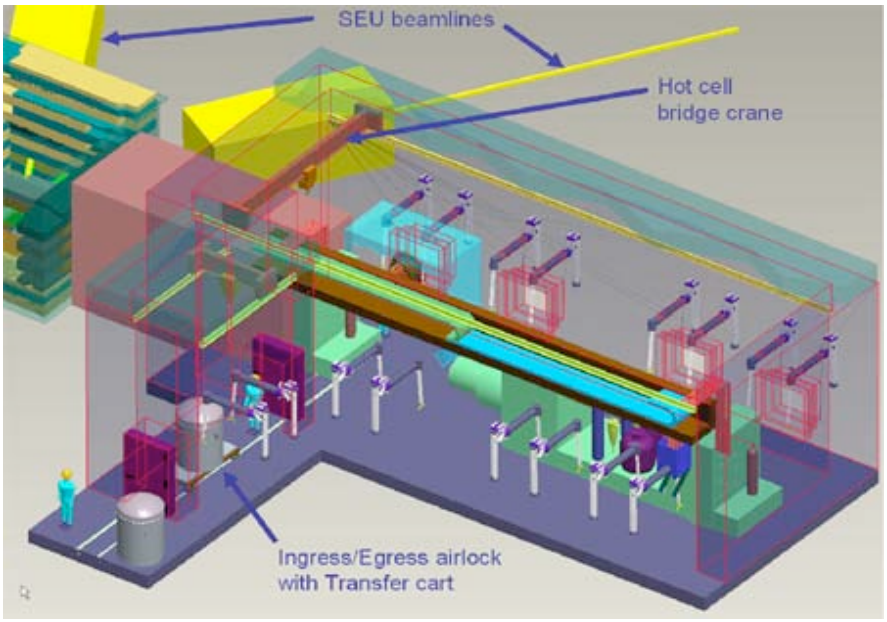

Fig. 65. Detailed view of the Winchester concept, illustrating the hot cell bridge crane and the ingress/egress transfer cart system. Two SEU beamlines are visible at the top of the picture. The near wall of the hot cell is removed in this view to add clarity. The TRAM is shown in both operational positions.

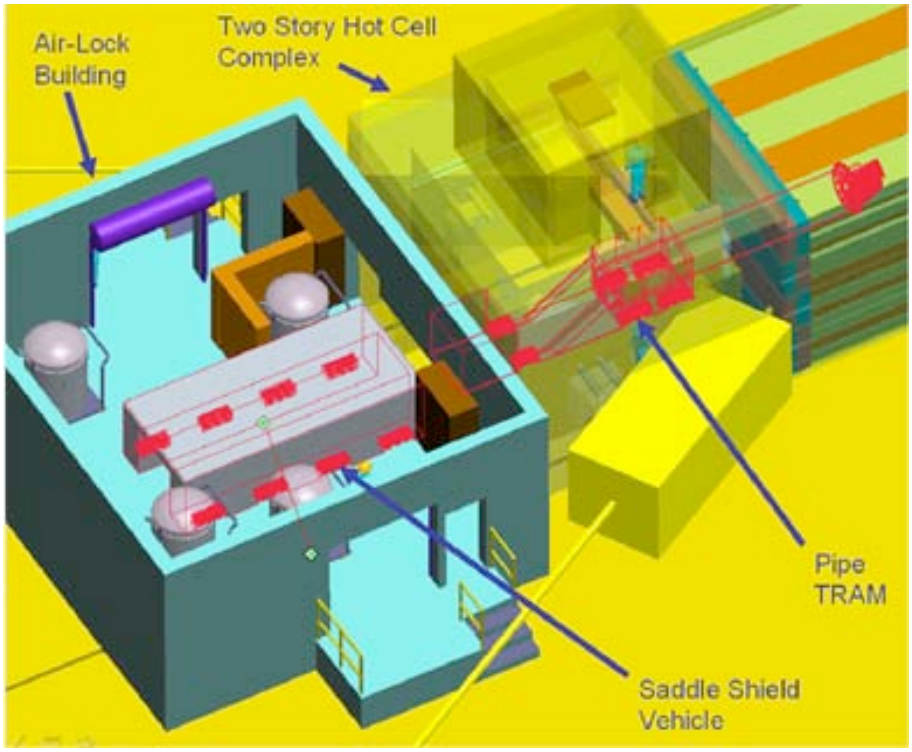

Fig. 66. The pipe TRAM configuration showing the two story hot cell complex and the air-lock building. A saddle shield vehicle is required to cover the active components on the pipe TRAM during operation, to minimize radiation damage to components in the hot cell.

Helium Chamber and Internals

Inner Shielding and Helium Tank

Argonne Engineers developed two alternative inner shielding constructions that re-use a high percentage of existing shielding materials, saving significantly on construction costs. Configuration A, shown in Fig. 67, requires significant cutting of existing Atlas counterweights to achieve a high level of shielding efficiency. Configuration B, shown in Fig. 68, requires less cutting of Atlas counterweights, with the attendant risk of increased radiation streaming paths. Neutronics analyses will be performed to assess the streaming question, which will allow a selection between the two options.

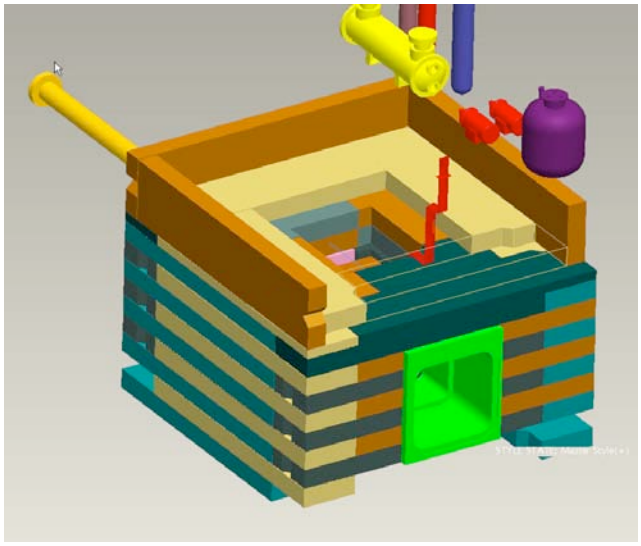

Fig. 67. Re-used shielding blocks fill most of the volume in the helium tank. Staggering of joints provides an efficient shielding package.

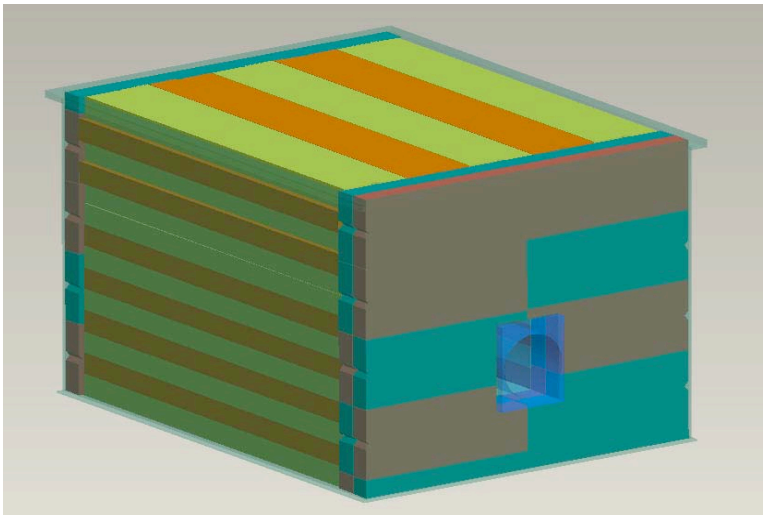

Fig. 68. This configuration of re-used shielding blocks requires fewer block cuts, but provides less effective shielding.

We developed a concept of a target vacuum chamber with all seals in areas that are easier to access, enhancing serviceability. The vacuum chamber is a weldment with four ports, one for the proton beam, one for the TRAM, and two for possible SEU beamlines. The target vacuum chamber is shown in Fig. 69 for an alternate configuration from the baseline design. Seals and/or windows can be replaced from the exterior of the helium tank without the need to disassemble the inner shielding. This has the potential to be a significant operational cost savings. The target vacuum chamber is isolated from external forces during operation, maintaining the precision alignment of the target assembly to the proton beam. The target vacuum chamber can be replaced with a reconfigured target chamber by opening the helium chamber and un-stacking the inner shielding.

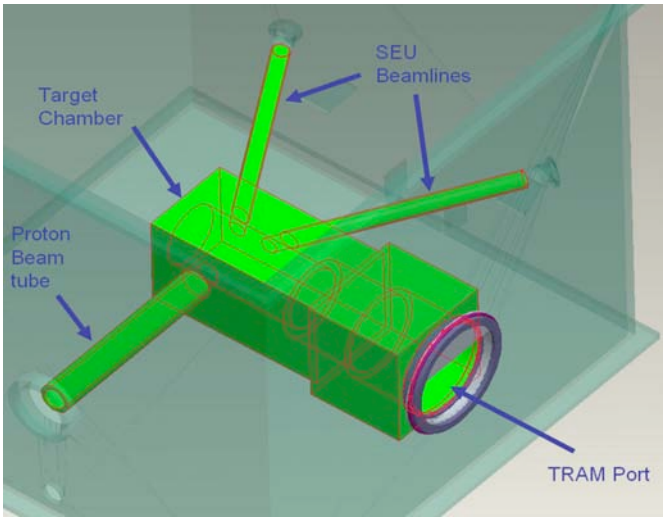

Fig. 69. Replaceable target vacuum chamber with four ports. Each port is sealed at the helium vessel wall to separate helium, vacuum, and air atmospheres.

A method was modeled for creating external shielding around the proton beam by reusing existing concrete and steel shielding blocks. Figure 70 illustrates the external shielding created this way. Details of seismic restraint remain to be addressed.

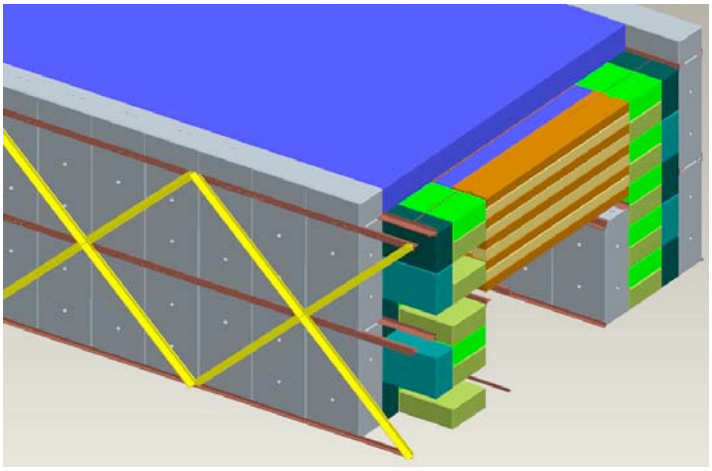

Fig. 70. External shielding around the proton beam line, created by stacking and securing existing concrete and steel shielding blocks. Steel structural members provide seismic restraint.

Accelerator Systems

Accelerator Team members finished defining the functions and requirements for their respective systems. This activity was in response to the request by the chairman of the MTS External Review Committee to generate functions and requirements for all systems.

Three technical notes were written that describe different aspects of the MTS beam line. The first technical note describes the beam optics, the second describes the raster-magnet section, and the third discusses beam steering and characterization. All three documents have been sent to the MTS Project Office.

We have been analyzing data from the beam jitter experiences performed during the last LANSCE Run Cycle, and have written a technical note that describes their results to date. The analysis of the jitter data tentatively indicates that beam jitter is greater than previously thought. However, there are still unresolved inconsistencies with the data that need to be settled before drawing definitive conclusions.

Safety and Permitting

A draft of the MTS Preliminary Hazard Analysis (PHA) was submitted to DOE-HQ on January 13, 2006, fulfilling an AFCI level-2 milestone. The principal PHA results, as reported in the first AFCI Quarterly Report for 2006, have not changed. A draft document entitled, *Safety Approach for Developing a Preliminary Safety Assessment Document (PSAD) for MTS* was prepared for review by MTS project participants. It is intended that this be a standalone "safety approach" document for MTS. Besides describing the overall MTS safety approach, this document includes summary descriptions of the MTS PHA results, a "Safety-by-Design" philosophy, the processes for determining credited controls to prevent or mitigate unwanted hazardous material releases, and the relationship between Important to Safety (ITS) levels and Management Levels (MLs) for systems, structures and components. Additionally, the document delineates top level functional and operational requirements (F&ORs) that will be used by the MTS design team to establish a highly reliable and robust safety design that will minimize the risk and provide adequate protection of the onsite workers, offsite public, and the environment. Work was initiated during this quarter on developing a Preliminary Safety Assessment Document (PSAD) and a supplemental Fire Hazards Analysis (FHA) for MTS.

LANL-Sponsored University Programs

University support has been an important part of the AFCI Program. In addition to the general university programs run by DOE-HQ, a number of universities have been supported directly by LANL programmatic funds to provide technical assistance to the AFCI Program. However, direct laboratory support is being discontinued, and the only remaining LANL support is to the University of Illinois.

University of Illinois

Scope

UIUC will investigate impedance spectroscopy as a feasible method of measuring the effects and rates of LBE corrosion on structural materials. This impedance spectroscopy technique employs alternating electric currents of various frequencies to measure the electrical impedance through a corrosion probe of a surface corroded by lead-bismuth. UIUC researchers will collaborate with DELTA Loop research members at LANL and construct a container/piping system to investigate those issues related to corrosion in high-temperature LBE. UIUC will construct an LBE loop (piping, pumps, thermocouples, heating elements, etc) at the Nuclear Engineering Laboratory (NEL), and will conduct controlled experiments to take impedance spectroscopy measurements on corroding steel samples. Post-exposure sample analysis will be conducted at the DOE-sponsored UIUC Materials Research Laboratory.

For effects of helium on irradiation damage in BCC iron, the university will investigate irradiation damage and He effects in ferritic materials (single-crystal iron) through experimental irradiation exposures and computer simulations of radiation damage. The objective of this project is to examine the dependence of damage cascades in iron samples on the dimensions of He bubbles and how this alters material properties. In the experimental program, ion irradiations with H and He ions will be used to develop various levels of displacement damage in Fe single crystals. Some of the parameter space that will be investigated experimentally includes varying PKA (Primary Knock-on Atom) energies, system sizes, He bubble size, pressures and concentrations and varying doses. Molecular dynamics approaches will be used to model this system. In the computational modeling work, varying PKA energies, system sizes, He bubble sizes, pressures and concentrations, and varying radiation doses will be investigated. These results will be critical in assessing the effects of radiation on ferritic alloys for use in AFCI and Gen IV systems.

Impedance Spectroscopy for Monitoring Corrosion in LBE Systems

The objective of this research program is to investigate and develop impedance spectroscopy (IS) as a feasible method of measuring the effects and rates of Lead-Bismuth Eutectic (LBE) corrosion on structural materials. The impedance spectroscopy technique employs alternating electric currents of various frequencies through a corrosion probe to measure the electrical impedance of a surface undergoing corrosion by lead-bismuth. The frequency response is analyzed to

provide information about the type, thickness and growth rate of the corrosion layer that develops during exposure to lead-bismuth.

Oxide Scale Characterization

To learn the structure and composition of the oxide scale formed on condition of immersion in the lead-bismuth eutectic (LBE), scanning electron microscopy (SEM) coupled with energy dispersive x-ray spectroscopy (EDS) tests were carried out this quarter on a sample created during last quarter's open-air tests. The result (see Fig.71) showed that there was a 2.77-μ-thick oxide layer formed on the surface of the underlying metal, SS316. This sample had been oxidized in an open-air furnace for 60 hours under 800ºC and was immersed in the LBE afterwards for over a week.

The composition of the oxide layer and its surrounding material was investigated and is shown in Figs. 72–74. A compositional change of the component iron and chromium along the depth of the oxide layer was observed. The result showed that the percentage of iron in the sample decreased along the direction from the underlying metal to the oxide layer, while the percentage of chromium increased. This may be caused by a diffusion process in which the iron diffuses inward and the chromium diffuses outward in the oxide layer. Further investigation and theoretical mode will be employed to study this process. In addition, the technique of Auger Electron Spectroscopy (AES) may be used in the future to get a better in-depth profile of the elements in the oxide layer and metal.

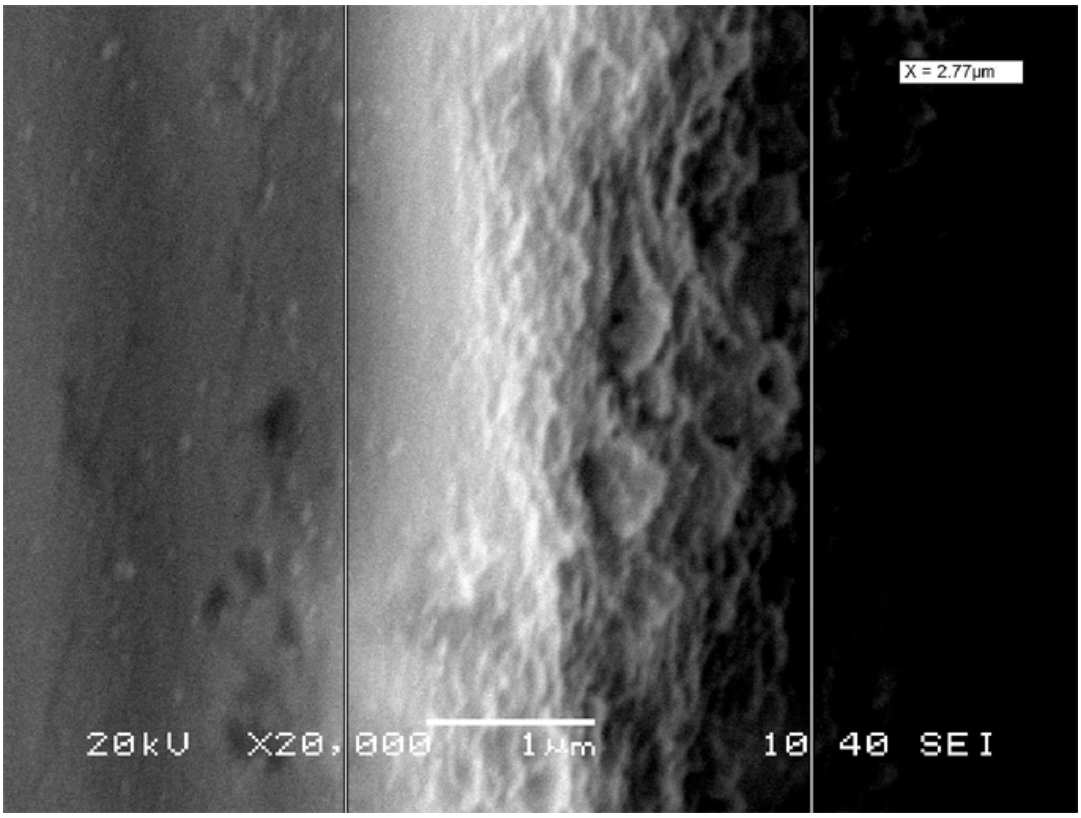

Fig. 71. SEM micrograph of the oxide layer

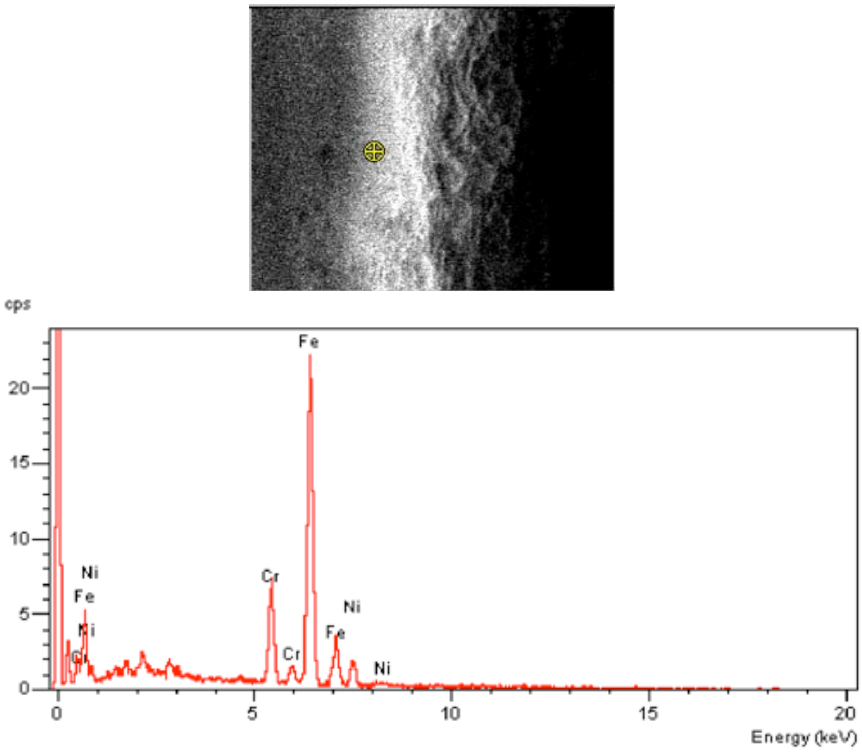

Fig. 72. Leftmost point on the oxide layer and its EDS spectrum, indicating its elemental composition

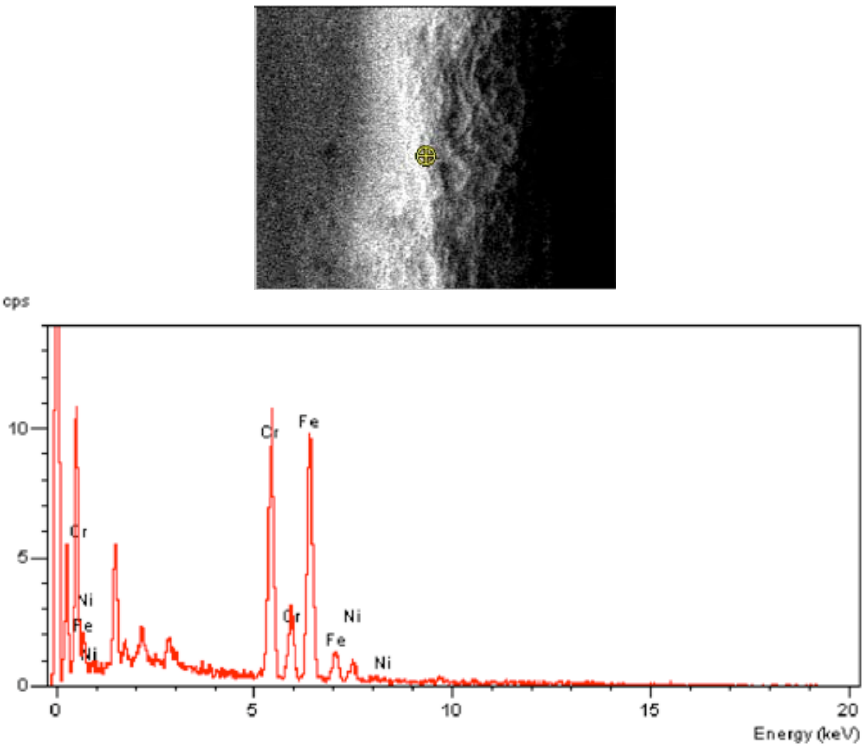

Fig. 73. Center point on the oxide layer and its EDS spectrum, indicating its elemental composition

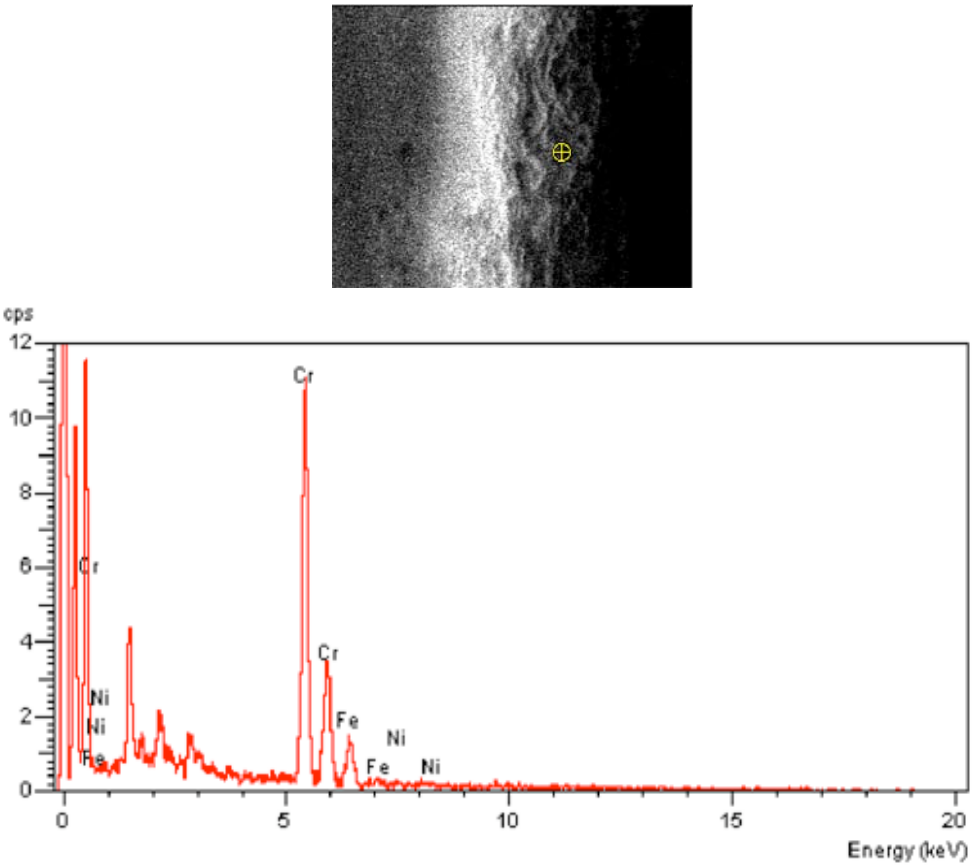

Fig. 74. Rightmost point on the oxide layer and its EDS spectrum, indicating its elemental composition

Although the SEM micrograph showed the existence of the oxide layer, it did not contain too much information about the structure of the layer. The edge of the oxide layer was damaged (see Fig. 75). The reason for this is that the poor edge retention (see Fig. 76) of the mounting material (in this case, epoxy resin) cannot protect the oxide layer during the polishing process. In polishing, the polishing rate of the mounting material is faster than the metal sample. After polishing for a while, the metal sample protruded from the mount surface and its edge was rounded and damaged (see Fig. 80). To avoid this and achieve a better result, several efforts were made:

- A chemical nickel plating on the surface of the sample was employed before the polishing process. The nickel layer can provide sufficient protection to the oxide layer.
- A diamond-polishing compound was used in the polishing process instead of using common silicon-carbonate polishing paper. This could improve the edge retention further.
- Semiautomatic polishing machine was used to get a better surface flatness instead of manual polishing.

SEM & EDS will be used in the near future to evaluate the effect of these efforts.

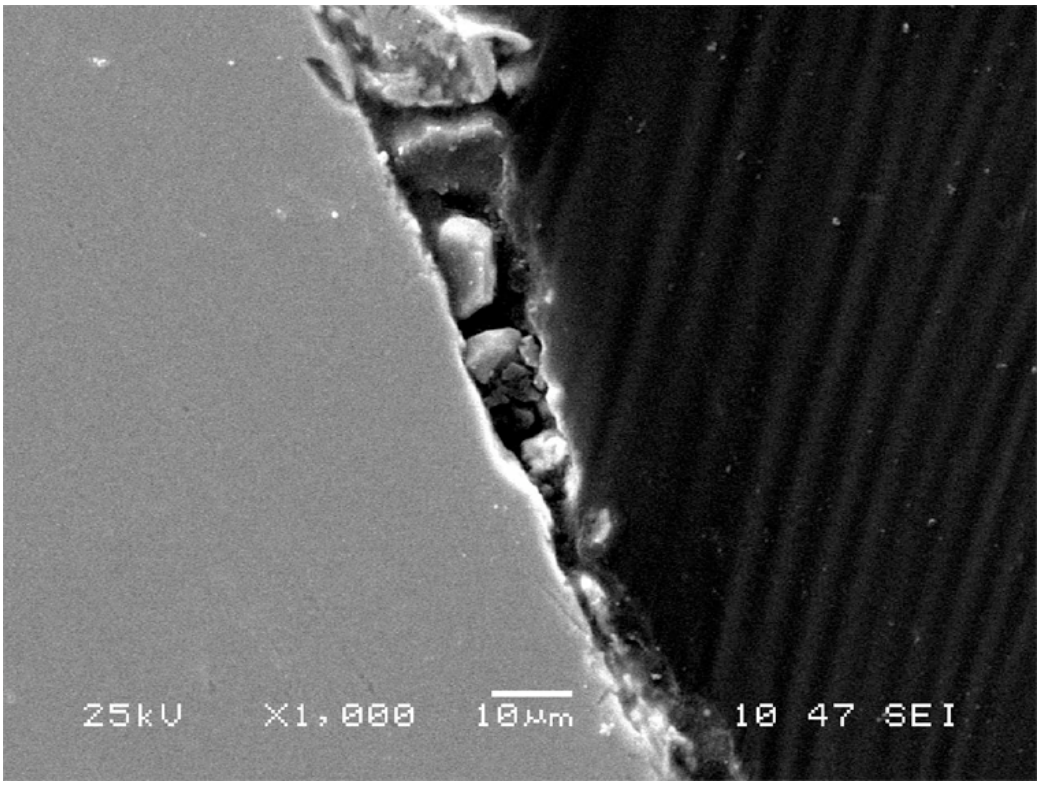

Fig. 75. SEM micrograph showing the poor edge retention when the sample is prepared without nickel plating and by polishing with silicon carbide paper instead of diamond polishing compound

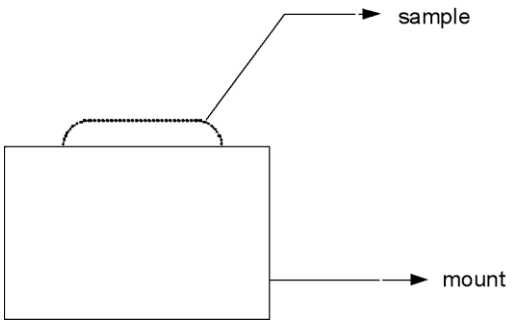

Fig. 76. Schematic drawing of how the edges of the sample are rounded when measures are not taken to retain the edges.

Miscellaneous Accomplishments

This quarter, a MS thesis was written on the oxygen control technique used in LBE experiments. The results and discussion of the topics covered in the thesis will be reported in the next quarterly report.

We continued to work with Dr. Scott Lillard at LANL. Plans were made for work to be performed at Los Alamos this summer with Dr. Lillard in support of this program.

Effects of Helium on Irradiation Damage in BCC Iron

The goal of this project is to utilize both computer simulations and experiments to understand the effects that helium and hydrogen have on irradiation damage occurring in single-crystal BCC (body centered cubic) iron and in more complex Fe-base alloys as the program progresses..

Simulation Program

Previously, molecular dynamics (MD) test simulations were conducted with WARP (a parallel MD code). These tests consisted of low-energy (2–10 keV) irradiations of the pure BCC iron and iron-helium systems at 573 K and 723 K with He bubbles or He interstitials of varying concentrations. The results obtained for the Fe-He irradiations indicated that additional testing of the Fe-He system was necessary. This was evidenced by the immediate amorphization of the lattice following the introduction of an energetic atom. Additional calculations for the screening potential are being conducted to more accurately fit the modified embedded atom method (MEAM) potential for Fe-He. This will provide a more reliable potential. Once the potential is modified, additional simulated irradiations will be conducted in the future with varying temperature, He concentration, and bubble size and concentration. The effects of incident-ion direction and energy (up to 100 keV) will also be investigated. Particular attention will be focused on the evolution of defects, including He interstitials, clusters, and bubbles. In the future, the effects of H in iron (Fe-H), as well as He and H in iron (Fe-H-He) subjected to irradiation will be considered.

Experimental Program

The experimental program is designed to provide a range of irradiation conditions that will produce various levels of atomic displacement damage (displacements per atom, dpa) and He levels. The following protocol is followed for the irradiation of the single-crystal BCC iron: The iron is first implanted with He at ambient temperature followed by proton implantation at either 573 K or 723 K (300ºC or 450ºC). Helium will be implanted at concentrations of 0, 0.3, 3, 4.5, 30, 45, or 450 appm. A dose from the irradiation with 1 MeV H^+ of 0, 0.03, 0.3, or 3 dpa will be subsequently implanted in the specimens. The combination of both irradiations using He and protons will lead to four values of He -to-damage ratios: 0, 10, 150, and ∞ (appm/dpa). The 0 and ∞ are control values for no He and no proton dose, respectively. The values of 10 and 150 appm/dpa were chosen since these values are consistent with what is observed in fusion and spallation systems, respectively. All irradiations will be carried out at two different temperatures: 573 K and 723 K with the exception of the ∞ appm/dpa value, which will only be performed at 723 K since the higher temperature will result in the greatest bubble formation. Once these samples are irradiated as described, they will undergo positron annihilation spectroscopy (PAS) measurements. Depending on the initial results from PAS, it may be necessary to revise the irradiation matrix described above. Following PAS, the specimens will be analyzed via transmission electron microscopy (TEM).

Positron annihilation spectroscopy (Doppler broadening) was previously conducted at Washington State University with all 25 single-crystal BCC specimens that were irradiated with varying proton doses and He concentrations (as described above). One additional specimen was not annealed, nor irradiated, but utilized for comparison purposes. The PAS technique with a beam ranging up to 70 keV allowed for depth profiling of the damage region (particularly in the 1–4 micron range) of the specimens.

The PAS Doppler broadening results demonstrated that the S parameter increased with He concentration, as shown in Fig. 77. The S parameter is an indication of the amount of open-volume defects present. As the S parameter increases, the amount of open-volume defects also increases. Figure 78 demonstrates that the S parameter also increased as the proton damage increased, as expected. The S parameter demonstrated that there were fewer open volume defects present in the 450ºC irradiated specimens when compared to the 300ºC irradiated specimens. Figure 79 shows five specimens that were irradiated to 3 dpa with protons at both 300ºC and 450ºC and with varying concentrations of He and one specimen that was subjected to the largest He concentration at 450ºC.

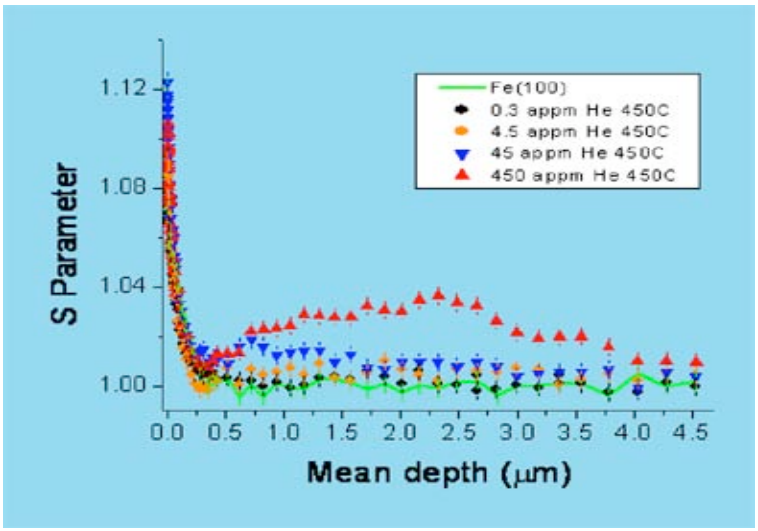

Fig. 77. S parameter vs. mean positron depth in BCC single-crystal Fe specimens implanted with various concentrations of He at 450ºC. The Fe(100) is a reference specimen that was not implanted with He.

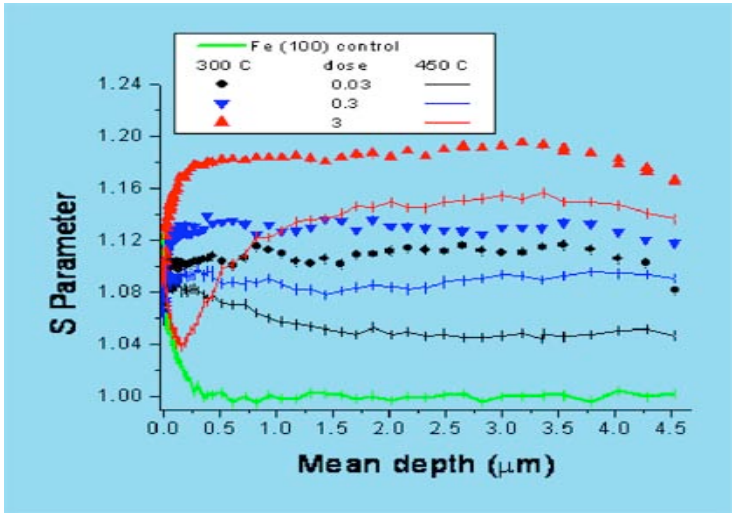

Fig. 78. S parameter vs. mean positron depth in BCC single-crystal Fe specimens irradiated with various proton doses at 300ºC and 450ºC. The Fe(100) is a reference specimen that was not implanted with He.

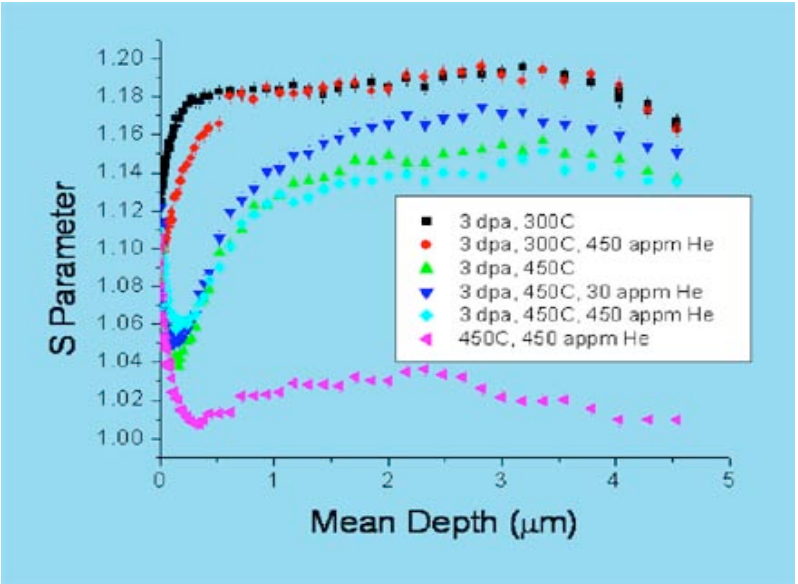

Fig. 79. S parameter vs. mean positron depth in BCC single-crystal Fe specimens irradiated with various proton doses and He concentrations at 300ºC and 450ºC.

This graph (Fig. 79) illustrates that the greatest effect on the S parameter is a result of the proton irradiation. The effects of the He implantation are not very clear with respect to the S parameter. These effects will need to be resolved by additional techniques. Also, note that all of the 450ºC irradiations demonstrated a decrease in the S parameter in the first micron of the sample, indicating that the surface is acting as a sink for defects.

Polycrystalline and single-crystal BCC Fe TEM specimens were pre-implanted with 3 and 30 appm of He (2.3 MeV) at the University of Michigan. These specimens were then thinned to expose the He-implanted region and then subjected to *in-situ* TEM at Argonne National Laboratory. The *in-situ* TEM utilized 250-keV protons to conduct uniform radiation damage throughout the specimens. Micrographs of the *in-situ* TEM results of polycrystalline Fe without He are shown in Fig. 80. The temperatures of 300ºC and 450ºC were studied at doses ranging from 0.03 dpa to 0.6 dpa. The 300ºC sample demonstrated visible black spots at 0.3 dpa and 0.6 dpa, while no black spots were observed in the 450ºC specimen. The results of the 450ºC specimen indicated movement and perhaps annealing of the dislocation loops. These results can be compared to that of the PAS results, which showed more damage in the 300ºC specimens and a release of defects at the surface of the 450ºC specimens.

Training was completed on the Focused Ion Beam (FIB) device for preparation of TEM specimens. This technique is being evaluated for TEM specimen preparation of the single-crystal specimens that have been previously irradiated. This technique will be carefully compared to the traditional mechanical polishing and chemical electropolishing techniques. TEM test specimens of polycrystalline (irradiated and non-irradiated) were prepared. One of the major advantages of the FIB technique is that a precise region can be elected for analysis and little specimen is consumed or wasted.

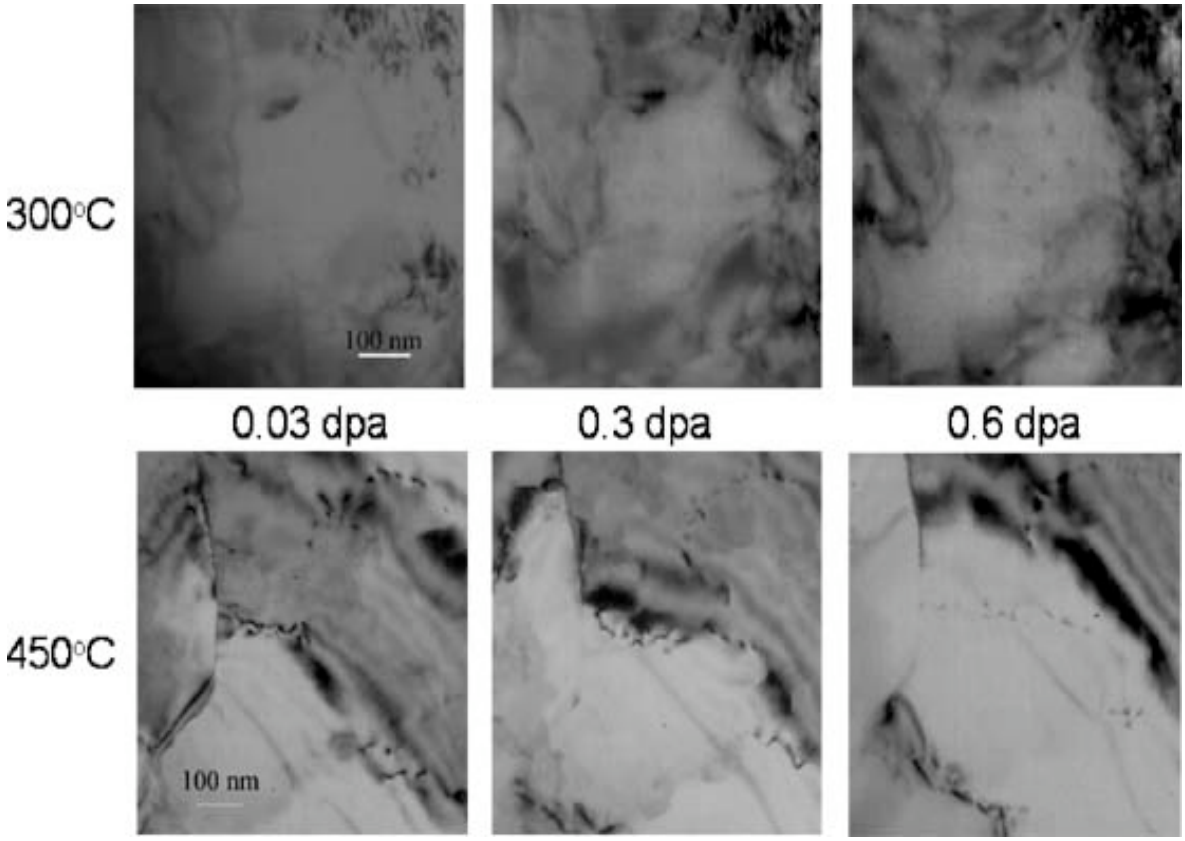

Fig. 80. *In-situ* TEM results of polycrystalline Fe (no He) subjected to 250 keV proton damage at various temperatures.

Miscellaneous Accomplishments

Final manuscript (proof corrections) from the TMS conference (Feb 2005) was submitted for publication to the *Journal of Nuclear Materials* entitled "Positron Annihilation Spectroscopy of Proton Irradiated Single Crystal BCC Iron" with multiple authors from UIUC, LANL, and Idaho State University.

A talk was presented at the TMS conference in March 2006 entitled "The Effects of Helium and Hydrogen in Irradiated Single Crystal Body-Centered Cubic Iron" with multiple authors from UIUC, LANL, and Idaho State University.

References

[1] M. R. Sørensen and A. F. Voter, J. Chem. Phys. 112, 9599 (2000).
[2] F. Montalenti, M. R. Sørensen and A. F. Voter, Phys. Rev. Lett. 87, 126101 (2001).
[3] A. F. Voter, F. Montalenti and T. C. Germann, Ann. Rev. Mater. Res. 32, 321 (2002).
[4] G. Kresse and J. Hafner, Phys. Rev. B 47, 558 (1993); 49, 14251 (1994); 55, 11169 (1996).
[5] M.I. Mendelev et al., Philos. Mag. 83, 3977 (2003).

[6] G. Henkelman, B. P. Uberuaga and H. Jónsson, J.Chem. Phys. 113, 9901 (2000).
[7] G. Henkelman and H. Jónsson, J.Chem. Phys. 113, 9978 (2000).
[8] K. Morishita, R. Sugano, et al., Nuclear Instruments & Methods in Physics Research Section B-Beam Interactions With Materials and Atoms, 6th International Conference on Computer Simulation of Radiation Effects in Solids 202, 76-81 (2003).
[9] D. T. Gillespie, Journal of Physical Chemistry, Symposium on Reaction Mechanisms, Models and Computers 81, 2340-61 (1977).
[10] A. B. Bortz, M. H. Kalos, et al., Journal of Computational Physics 17, 10-18 (1975).